Characterization of tissue properties on the sub-micron scale in human bone by means of Synchrotron Radiation CT

Dissertation

zur Erlangung des akademischen Grades

doctor rerum naturalium

(Dr. rer. nat.)

im Fach Biophysik

eingereicht an der

Mathematisch-Naturwissenschaftlichen Fakultät I

der Humboldt-Universität zu Berlin

von

Diplom-Physiker Bernhard Hesse

Präsident der Humboldt-Universität zu Berlin:

Prof. Dr. Jan Hendrik Olbertz

Dekan der Mathematisch-Naturwissenschaftlichen Fakultät I:

Prof. Stefan Hecht, Ph.D.

Gutachter/in: 1. Kay Raum

2. Pascal Laugier

3. Klaus Rademann

4. Birgit Kanngießer

Datum der mündlichen Prüfung: 24.03.2014

The present thesis was carried out within a bi-national program (Co-tutelle de thèse) between L'Institut National des Sciences Appliquée de Lyon and the Humboldt-Universität zu Berlin.

The present manuscript is submitted to INSA de Lyon and to the Fakultät 1 of the Humboldt-Universität zu Berlin at the same time. The cover page is adjusted to the institute where this manuscript is submitted to. The cover page of the respective other institute can be found in the appendix.

Abstract

Under healthy conditions, human bone undergoes permanent remodeling in order to adjust to mechanical demands, to repair microcracks and to maintain mineral homeostasis. This process of remodeling is performed by osteoblasts and osteoclasts, the bone-forming and bone-resorbing cells, respectively. The activity of osteoclasts and osteoblasts is triggered by the osteocytes, the most frequently occurring type of bone cell, via mechanosensation processes. Mineralization of the newly formed bone tissue has an initial rapid phase, within which up to 90% of the final mineralization level is reached. This is followed by a secondary mineralization process, which continues for several years until full mineralization is achieved. It is known that the mineral available from nutrition and from the remodeling process is insufficient to cover the daily mineral fluctuation in the blood. It has been proposed that the mineral in the bone matrix adjacent to the extracellular fluid in the pore network serves as rapid exchangeable calcium pool used to maintain mineral homeostasis. In this context, enlarged osteocyte-lacunae volumes have been reported in a lactating mice model.

In the present work, the volume distribution of osteocyte lacunae of human cortical jaw bone has been investigated, and a comparison between healthy subjects and patients treated with bisphosphonates was carried out by means of synchrotron radiation μCT. Bisphosphonates prescribed during treatment for osteoporosis or bone metastasis inhibit osteoclast activity and thus decrease the bone turnover. We hypothesized that patients treated with bisphosphonates would exhibit larger volumes of osteocyte lacunae, since tissue at the surface of the peri-lacunar region has been resolved in a process called osteocyte osteolysis in order to maintain mineral homeostasis, because the mineral available via the remodeling process has decreased. Interestingly, we could not confirm this hypothesis. It remains unclear if the potential process of osteocytic osteolysis results in decreased peri-lacunar mineralization instead of enlarged osteocyte lacunae. We found that the apparent mass density of jaw bone was significantly smaller compared to that of tibia, consistent with a higher bone turnover in the jaw bone. In a comparison of the volume distribution between the jaw and the tibial/femoral sites, we observed a higher value of large osteocyte lacunae volumes in the jaw. We concluded that bisphosphonates are deposited into jaw bone at a higher rate, due to its higher bone remodeling rate. Moreover, if deposited into osteocyte lacunae during the mineralization of

osteocyte lacunae (micropetrosis), a toxic concentration of bisphosphonates may be reached following the de-solution of minerals, caused by a decreased pH level in the course of infections, for example. This process potentially explains one of the serious side effects of bisphosphonate treatment: osteonecrosis of the jaw. However, more in-depth studies are necessary to support this hypothesis, in particular with samples originating from more homogeneous groups than those being used in the present thesis.

In a second approach, we used synchrotron radiation nano-CT in combination with phase retrieval to investigate the morphology of the canalicular network and the bone tissue properties in the vicinity of the lacuna-canalicular network of human jaw bone, originating from both healthy subjects and patients treated with bisphosphonates. We hypothesized that the secondary mineralization process takes place via a diffusion process through the fluid-matrix interface at both the lacunar and the canalicular surfaces. The proposed diffusion process should result in mass density gradients with respect to the distance to the pore boundary.

We observed that the hypothesized mass density gradients indeed exist at both the lacunar and canalicular interfaces. However, based on our finding that these gradients exist at the lacunar as well as at the canalicular surface, we further hypothesized that the process of mineral exchange between the extracellular fluid and the mineralized matrix occurs at all bone surfaces, including the canalicular network. Our data suggested that the capacity of the pore network to exchange minerals with the extracellular mineralized bone matrix would increase by one order of magnitude if the canalicular surface is taken into account. Based on the morphology of the lacuna-canalicular network, we could then show that the mass density gradients are most likely unaffected by short-term fluctuations of mineral in the fluid, and are instead affected solely by secondary mineralization processes.

To conclude, the findings concerning the effective diffusion processes during secondary mineralization and also that the canalicular surfaces are likely to be involved in this process, provide an important contribution in terms of understanding and optimizing drug delivery. However, more sophisticated studies should be performed, targeting not only the changes of tissue properties during secondary mineralization, but also during fluctuations of mineral concentration in periods of high mineral demand.

Kurzfassung

Gesunder humaner Knochen unterliegt einem permanenten Umbau, um sich den mechanischen Anforderungen anzupassen, Mikrofrakturen zu reparieren und das Minerliengleichgewicht zu erhalten. Dieser Umbauprozess wird durch Osteoblasten- und Osteoklastenaktivität realisiert, den knochenbildenden bzw. knochenresorbierenden Zellen. Es wird angenommen, dass die Aktivität der Osteoklasten und Osteoblasten durch Osteozyten reguliert wird, wobei dem Oteozyten-Netwerk mechanosensorische Fähigkeiten zugesprochen werden. Osteozyten befinden sich in Lakunen die über Kanäle verbunden sind, sie bilden das lakuno-kanalikuläre Netzwerk (LKN). Neu gebildeter Knochen erreicht innerhalb weniger Tage bis zu 90% seiner Mineralisierung. Dieser primären Mineralisierung folgt ein sekundärer, mehrjähriger, zur endgültigen Mineralisierung führender Prozess. Mineralien, verfügbar aus den ständigen Umbauprozessen des Knochens, sind nicht ausreichend und die zugehörigen Prozesse zu langsam, um Schwankungen der Kalziumkonzentration im Blut zu erklären. Eine Hypothese zum Kalziumgleichgewicht schlägt vor, dass Mineralien in unmittelbarer Nähe der extrazellulären Flüssigkeit des LKN entfernt bzw. abgelagert werden. In diesem Zusammenhang wurde bereits über vergrößerte Osteozyten-Lakunen (OL) in einem stillendem Mausmodell berichtet.

Im ersten Teil dieser Arbeit wurden morphologische Eigenschaften der OL in humanem Knochen mittels Synchrotron-µCT untersucht. Dabei wurden einerseits gesunde Probanden und andererseits mit Bisphosphonaten (BP) behandelte Patienten verglichen. BP, Medikamente die bei der Behandlung von Osteoporose oder Knochenmetastasen eingesetzt werden, hemmen die Aktivität der Osteoklasten und erhöhen somit die Knochenumsatzzeit. Wir haben vermutet, dass die mit BP behandelten Patienten vergrößerte OL aufweisen, da ein Teil des peri-lakunaren Knochengewebes für das durch die gehemmten Osteoklasten veränderte Mineralgleichgewicht im Körper verwendet werden könnte. Interessanterweise konnten wir diese Hypothese nicht bestätigen. Es blieb unklar, ob der potentielle Prozess des Abbauens des peri-lakunaren Gewebes zu einer verminderten peri-lakunaren Mineralisierung führt, statt zu vergrößerten OL. Unsere Untersuchungen haben gezeigt, dass humaner Kieferknochen im Vergleich zu Tibia einen geringeren Mineralisierungsgrad aufweist, was auf einen höheren Knochenumsatz des Kiefers hinweist. Wir schlussfolgerten daraus, dass BP aufgrund des höheren Knochenumsatzes in größerem Umfang im Kieferknochen abgelagert werden können. Beim Vergleich der Volumenverteilung der OL des Kieferknochens mit der

von Tibia und Femur fanden wir größere OL im Kiefer. OL können, nach dem Tod der Osteozyten, mit Mineral gefüllt werden. Wir folgerten, dass BP während dieses Prozesses zu hohen Konzentrationen in den OL abgelagert werden könnten, und es schließlich zu einer toxischen Konzentration von BP kommen kann, wenn die BP-belasteten Mineralien wieder herausgelöst werden (z.B. durch einen verringerten pH Wert während einer Infektion). Diese Hypothese könnte ein wichtiger Schlüssel im Verlauf einer Nebenwirkung der Behandlung mit BP sein: der Osteonekrose des Kiefers (BRONJ). Allerdings muss diese Hypothese in einer weiterführenden Studie genauer untersucht werden.

Im zweiten Teil dieser Arbeit haben wir Synchrotron-Nano-CT in Kombination mit Phasen-Kontrast angewandt, um die Morphologie des LKN und die Gewebeeigenschaften humanen Kieferknochens in der Umgebung des LKN von gesunden Probanden und mit BP behandelten Patienten zu untersuchen. Wir nahmen an, dass der sekundäre Mineralisierungsprozess mittels eines Diffusionsprozesses durch die Grenzfläche der extrazellulären Flüssigkeit im LKN stattfindet. Ein solcher Diffusionsprozess, der von der Diffusionskonstante und der Morphologie des LKN abhängig wäre, sollte in Gradienten der Massendichte in der Umgebung des LKN resultieren. Unsere Untersuchungen haben gezeigt, dass sowohl an den lakunären als auch an den kanalikulären Oberflächen Massendichte-Gradienten existieren. Daraus schließen wir, dass der Mineralienaustauschprozess zwischen der extrazellulären Flüssigkeit und der mineralisierten Matrix an der gesamten Oberfläche des LKN stattfindet. Wir schätzten, dass die Kapazität der Knochenmatrix Mineralien aufzunehmen oder bereitzustellen etwa eine Größenordnung höher ist, wenn die kanalikulären Grenzflächen einbezogen werden, gegenüber der Annahme, dass der Austausch lediglich an den Grenzflächen der OL stattfindet. Basierend auf der Morphologie des LKN konnten wir zeigen, dass die Massendichtegradienten wahrscheinlich nicht auf kurzfristige Schwankungen der Kalziumkonzentration im Blut oder den extrazellularen Flüssigkeiten zurückzuführen sind, sondern nur durch sekundäre Mineralisierungsprozesse verursacht werden. Unsere Erkenntnisse zu den Diffusionsprozessen während der sekundären Mineralisierung sind für das Verständnis und die Optimierung von neuen Medikamenten von großer Bedeutung. Weiterführende Studien sollten nun durchgeführt werden, um nicht nur die Veränderungen der Gewebeeigenschaften während der sekundären Mineralisierung zu untersuchen, sondern auch Schwankungen der Mineralienkonzentration bei hohen Kalziumanforderungen des Körpers zu analysieren.

Résumé Français étendu

En fonctionnement normal, les os subissent des remodelages permanents afin de s'adapter aux différentes contraintes mécaniques, de réparer leurs micro-fractures potentielles et de maintenir l'homéostasie des minéraux. Ces transformations s'opèrent grâce aux ostéoblastes et aux ostéoclastes qui sont des cellules respectivement responsables de la synthèse et de la résorption du tissu osseux. Les activités ostéoclastiques et ostéoblastiques sont orchestrées par les ostéocytes, qui sont les cellules osseuses les plus abondantes, logées dans des cavités appelées "lacunes" ostéocytaires. Les ostéocytes sont connectés entre eux via des dentrites se situant à l'intérieur de petits canaux de quelques centaines de nanomètres de diamètre, appelées canalicules. Ce réseau d'ostéocytes joue un rôle primordial dans le processus de mécano-sensation et de mécano-transmission. La morphologie du réseau lacuno-canaliculaire (RLC) est supposée être liée aux processus de mécano-sensation et mécano-transduction (Schneider *et al.*, 2010, Lanyon, 1993, Burger & Klein-Nulend, 1999, Zhou *et al.*, 2009, Wang *et al.*, 1993b, Weinbaum *et al.*, 1994, McCreadie *et al.*, 2004, Vatsa *et al.*, 2008, van Hove *et al.*, 2009, Currey, 2003, Mullins *et al.*, 2007). Ce réseau RLC assure aussi le transport des déchets et des substances nutritives au sein des cellules osseuses (Burger & Klein-Nulend, 1999). Il joue, de plus, un rôle essentiel dans la résorption de micro-fissures en stimulant le remodelage osseux (Currey, 1984b). En plus de leurs fonctions mécaniques, les ostéocytes sont supposées participer à la régulation du métabolisme minéral osseux tel que le métabolisme du phosphore (Westbroek *et al.*, 2002, Nakashima *et al.*, 2011).

Les études sur le réseau lacuno-canaliculaire ont surtout été réalisées à partir de coupes 2D imagées par microscopie optique ou électronique. La microscopie électronique à balayage (SEM, cf. (Reznikov *et al.*, 2013) permet aussi d'atteindre des résolutions inférieures au micron mais a pour l'instant été implémentée pour la représentation de tissus déminéralisés. Récemment, des études sur des tissus osseux de souris ont montré que la microscopie par rayons X permettait d'avoir accès au degré de minéralisation au voisinage du RLC avec une taille de pixel de 208 nm (Nango *et al.*, 2013). Les quelques représentations 3D ont jusqu'alors essentiellement été obtenues par microscopie confocale (Kerschnitzki *et al.*, 2011, Verbruggen *et al.*, 2012) avec cependant des images de très faible profondeur de champ. La faisabilité de la ptychographie par rayons X a été démontrée pour la représentation 3D du RLC avec des résolutions en dessous du micron (Dierolf *et al.*, 2010), toutefois les temps

d'acquisition restent trop long pour envisager une application à des séries d'échantillons. Une étude récente a montré que la nano-tomographie par rayonnement synchrotron en contraste de phase (SR-PNT) permettait de réaliser des reconstructions 3D de la densité volumique de l'échantillon avec une taille de voxel d'environ 60 nm de côté pour des champs de vue supérieurs à 100x100x100 μm^3 (Langer *et al.*, 2012b). Comparée aux méthodes conventionnelles de tomographie par atténuation, l'imagerie par contraste de phase est beaucoup plus sensible aux changements de masse. Cette technique a permis d'observer des détails sur le RCL et de quantifier pour la première fois en 3D les orientations des fibres de collagène dans les lamelles du tissu osseux (Varga *et al.*, 2013).

Une bonne régulation des niveaux de minéralisation de l'os est cruciale dans les tissus sains mais peut se trouver altérée dans le cadre de maladies osseuses telle l'ostéoporose. Une solution courante pour lutter contre l'ostéoporose ou le développement de métastase osseuse est de recourir à un traitement par bisphosphonates (BP) qui va permettre de freiner voire d'annihiler la résorption osseuse par inhibition de l'activité ostéoclastique (Dhillon & Lyseng-Williamson, 2008, Liberman *et al.*, 1995). Un surdosage de BP peut avoir un effet inverse et irréversible, entrainant une ostéonécrose de la mâchoire. Même si plusieurs hypothèses ont été récemment avancées, les mécanismes physiopathologiques des bisphosphonates responsables de l'ostéonécrose de la mâchoire sont encore mal compris (Otto *et al.*, 2010, Bertoldo *et al.*, 2007).

Dans le cadre de mes travaux de thèse, j'ai utilisé la tomographie par rayonnement synchrotron afin d'analyser et d'étudier la morphologie du RLC ainsi que la distribution de masse densité des tissus osseux minéralisés provenant de sujets contrôle ou atteints d'ostéonécrose de la mâchoire.

L'ostéonécrose ne survient qu'au sein des os de la mâchoire. Chez les animaux, le taux de renouvellement des os de la mâchoire est plus élevé que dans les autres parties du corps, à cause des différentes contraintes physiques exercées sur celle-ci et notamment par les dents. Nous pensons que l'absorption de BP par les cellules osseuses est étroitement liée à ce taux de renouvellement osseux. Dans un premier temps (i), nous étudierons si la densité moyenne des os de la mâchoire humaine est inférieure aux autres régions anatomiques, ce qui confirmerait l'hypothèse d'un taux de renouvellement plus important des os de la mâchoire. Les BPs réduisent l'activité ostéoclastique et donc ralentissent le renouvellement de l'os. Nous

étudierons dans un second temps (ii) si la masse volumique moyenne des os de la mâchoire est plus importante chez les patients atteints d'ostéonécrose. Une activité ostéoclastique réduite restreint les stocks de minéraux disponibles pour le remodelage osseux. Nous étudierons enfin (iii) si le volume des lacunes ostéocytaires est plus important chez les patients atteints d'ostéonécrose du fait du remodelage direct des parois lacunaires afin de maintenir l'homéostasie des minéraux.

La première partie rappelle les éléments nécessaires à la compréhension de ce travail, au niveau de l'os de l'imagerie osseuse et de la tomographie X.

Dans un premier temps, nous rappelons les connaissances de base au niveau de la structure et de la fonction de l'os. Nous nous focalisons sur la description du système ostéocytaire et des processus de remodelage, incluant la résorption et la formation osseuse. Compte tenu de notre sujet d'étude, nous décrivons également les BP et leurs mécanismes d'actions. Dans un deuxième temps, nous décrivons les méthodes d'imagerie du tissu osseux à l'échelle micrométrique ou sub- micrométrique. Dans un troisième temps, nous détaillons les principes de la micro-tomographie par rayons X et par rayonnement synchrotron. Après une description des phénomènes d'interaction X-matière, nous expliquons la formation de l'image en tomographie par rayons X. Nous décrivons brièvement le principe des méthodes de reconstructions d'images en tomographie par rayons X, et l'algorithme par rétro projection filtrée. Nous nous intéressons ensuite à la tomographie de phase qui sera utilisée dans la suite de cette étude et décrivons le contraste de phase obtenu en particulier par propagation d'un faisceau cohérent de rayons X tel que ceux qui peuvent être obtenus à partir d'une source synchrotron. Cette technique nécessite l'acquisition d'une ou de plusieurs images radiographiques à différentes distances de propagation qui doivent ensuite être traitées par un algorithme de reconstruction de phase. L'algorithme le plus simple est celui de Paganin. Il permet de reconstruire la phase à partir d'une seule distance sous l'hypothèse que l'objet est homogène et que l'on connaît le rapport delta/beta, i.e. le rapport entre la partie réelle et la partie imaginaire de l'indice de réfraction complexe dans l'échantillon. Des algorithmes exploitant différentes distances de propagation, basés sur une linéarisation du problème direct ont également été proposés, notamment l'approche mixte. La méthode de reconstruction de phase utilisée dans la suite utilise la méthode mixte suivie d'une séquence d'itérations prenant en compte le problème non linéaire. Après cette étape, les radiographies de phase sont utilisées dans un algorithme de reconstruction tomographique par rétroprojection filtrée pour

reconstruire l'image 3D de l'indice de réfraction complexe. Finalement, nous décrivant les systèmes expérimentaux d'imagerie tomographiques qui ont été utilisés à l'ESRF: le système de micro-tomographie parallèle de la ligne ID19 de l'ESRF, ainsi que le système de nano-tomographie de phase divergent de la ligne ID22.

La deuxième partie est consacrée aux trois études qui ont été menées pendant cette thèse.

Dans un premier temps (Chapter 3.1), nous avons analysé à l'échelle sous-micrométrique les propriétés géométriques des lacunes ostéocytaires des os de mâchoire humaine. Notre étude se fonde sur des données collectées à partir de 5 échantillons osseux prélevés chez 2 sujets sains ainsi que chez 3 patients atteints d'ostéonécrose. Les échantillons ont été scannés en micro-tomographie par rayonnement synchrotron sur le système parallèle de la ligne ID19 (taille de voxel de 300nm). Ces images ont été exploitées pour caractériser les lacunes ostéocytaires. Un ensemble de 19208 lacunes ostéocytaires ont été analysées. Les volumes moyens étaient V=296 - 502 μm^3 et leur écart type 153 – 234 μm^3, avec notamment des volumes moyens et des écart-types moindre dans les tissus ostéonaux. Ces lacunes avaient globalement une forme ellipsoïdale définie par 3 axes a>b>c, tels que a=2.2b et a=4c. La densité lacunaire variait entre 15800 et 50200 1/mm3. Nous avons de plus, quantifié la distribution spatiale du réseau lacunaire en calculant une distance relative des lacunes à la matrice minérale. Notre étude montre qu'environ 50% de cette matrice est situé à moins de 11.9 µm de la paroi lacunaire la plus proche. Enfin, nous avons quantifié la fréquence d'occurrence de matière minérale dans les lacunes ostéocytaires qui est apparue plus élevée dans les échantillons de tissu osseux ostéonécrosé. Dans cette étude pilote, le nombre trop restreint d'échantillons ne nous a pas permis de conclure sur les causes et l'évolution de l'ostéonécrose mais nous a permis de dégager différentes propriétés morphologiques pour chaque échantillon analysé.

A noter que cette étude ne nous a pas permis de confirmer que les patients traités par bisphosphonate présentaient des lacunes ostéocytaires plus larges que la normale. Nous ne pouvons donc conclure si les processus de résorption découlent d'une diminution de la minéralisation des zones péri-lacunaires plutôt que d'une quantité plus importante de lacunes ostéocytaires.

Dans le Chapitre 3.2, incluant plusieurs échantillons et les différents sites anatomiques, il est montré que les bisphosphonates se déposent plus facilement dans les os de la mâchoire grâce à un renouvellement osseux plus rapide. Si ces bisphosphonates se déposent dans les lacunes ostéocytaires pendant le processus de minéralisation, un seuil de toxicité de BP peut être atteint après la dissolution minérale provoquée par une diminution du pH pendant une infection. Ce procédé permet d'expliquer en partie l'effet secondaire du bisphosphonate qui n'est autre que l'ostéonécrose de la mâchoire. Cependant, ceci nécessiterait une étude plus approfondie notamment en considérant un plus grand nombre échantillons plus homogènes.

Dans le Chapitre 3.3, nous avons utilisé la nano tomographie de phase sur la ligne ID22 de l'ESRF (taille de voxel = 50 nm) afin d'étudier et comparer la morphologie des réseaux canaliculaires ainsi que les propriétés des tissus osseux au voisinage du réseau lacuno-canaliculaire de la mâchoire humaine dans des patients sains et/ou des patients traités au bisphosphonate. Cette technique permet d'avoir accès à la fois à l'architecture du RLC et fournit une cartographie 3D de la densité électronique de l'échantillon, qui permet d'avoir une idée de la minéralisation du tissu. De récentes études ont supposé que les canalicules seraient aussi impliquées dans les processus d'homéostasie minérale (Qing & Bonewald, 2009). Cependant, aucun échange de minéraux aux frontières canaliculaires n'a encore été observé. Nous avons fait l'hypothèse que la maturation du tissu osseux s'opérait par diffusion à travers l'interface lacune/fluide extra-cellulaire et la surface canaliculaire par gradients de densité. Ces gradients doivent dépendre de la constante de diffusion effective et de l'âge du tissu osseux.

Pour savoir si ce processus de diffusion se produit uniquement aux frontières lacunaires ou à toutes les frontières du réseau RLC, nous avons analysé la densité des tissus au voisinage des lacunes ostéocytaires et au voisinage des canalicules pour des échantillons osseux d'âges différents en considérant des tissus ostéonaux, des tissus interstitiels ainsi que des tissus osseux provenant de patients traités au bisphosphonate. Nous avons aussi pris en compte la morphologie du réseau RLC pour identifier à la fois l'impact des fluctuations à court-terme des minéraux dans le fluide et l'impact de la maturation des tissus osseux pendant la deuxième phase de minéralisation.

Concernant la morphologie du réseau canaliculaire, la porosité canaliculaire a été estimée à environ 2% avec des différences mineures entre les différents tissus analysés. Dans un

deuxième temps, nous avons observé que les diamètres canaliculaires Cn.Dm étaient sensiblement plus grand pour les tissus ostéonécrosés (Cn.Dm = 0.40 ± 0.04 µm) que pour les tissus ostéonaux (Cn.Dm = 0.36 ± 0.01 µm) ou interstitiels (Cn.Dm = 0.37 ± 0.04 µm). Enfin, nous avons mesuré à partir de la carte de distance 3D sur l'image des lacunes, la distance correspondant à 50% de la distribution, paramètre appelé Cn.Dist. Nous avons trouvé que la distance moyenne Cn.Dist50 de toutes les régions analysées était Cn.Dist50 = 1.3 ± 0.4 µm.

En ce qui concerne les propriétés tissulaires, nous avons montré que les gradients de densité induits étaient présents aux interfaces lacunaires et canaliculaires. A partir de ces résultats nous avons fait l'hypothèse que les procédés d'échange de minéraux entre le fluide extra-cellulaire et la matrice minérale se produisait sur chaque surface osseuse et donc du réseau canaliculaire. Nous avons aussi montré que la capacité de la matrice à résorber ou à fournir des minéraux pour ou à partir des matrices extra-cellulaires augmentait (environ 1 ordre de grandeur) par rapport aux cas où aucun échange ne se produisent au niveau de la surface canaliculaire. Selon les morphologies des réseaux lacuno-canaliculaires, nous avons enfin montré que les gradients de densité ne sont pas induits par des fluctuations court-terme des minéraux dans le fluide mais par les processus de minéralisation secondaire.

Les résultats de ces travaux montrent la participation des surfaces canaliculaires dans la diffusion de minéraux, phénomène qui peut être expliqué par un processus de diffusion pendant le procédé de minéralisation. Cette observation est totalement originale et la compréhension de ces phénomènes constitue une avancée significative pour remédier à l'ostéoporose et proposer des traitements adéquats.

Une étude plus approfondie permettrait d'étudier les changements de propriétés tissulaires non seulement pendant les épisodes de minéralisation secondaire mais aussi pendant les fluctuations de minéraux.

Chapitre 4: Dans le but d'étudier la morphologie du RLC et la distribution de la densité massique de l'os cortical de la mâchoire humaine et d'établir une comparaison entre les sujets sains et les patients traités au moyen de bisphosphonate, on a pu montrer que la micro/nano-tomographie par rayonnement synchrotron en contraste de phase est un outil adapté à l'analyse des os à l'échelle micrométrique et sous-micrométrique. Les détails sur la morphologie de la micro/nano-porosité ainsi que les propriétés du tissus minéralisé

environnant à cette échelle présentent un grand intérêt pour la compréhension des fonctions osseuse à toutes les échelles.

Content

1 INTRODUCTION

Bone is a biological material structured in a hierarchical way over several length scales, from the molecular level of collagen to the organ level (Fratzl & Weinkamer, 2007, Weiner & Traub, 1992, Rho *et al.*, 1998). Apparent bone quality in terms of strength, for example, depends on bone properties at all scale lengths. Thanks to recent advances in imaging technologies the three-dimensional ultrastructure of bone became assessable (Langer et al., 2012b). Details on the morphology of the micro/nano porosity as well as properties of the surrounding mineralized tissue at this scale are of high interest in understanding bone function at all length scales.

Under healthy conditions human bone undergoes permanent remodeling in order to adjust its structure to mechanical demands, repair microfractures and maintain mineral homeostasis. This process is called remodeling, which is performed by osteoblasts and osteoclasts, the bone-forming and bone-resorbing cells, respectively. The activity of these cells is believed to be orchestrated by osteocytes, the most frequently occurring type of bone cell, which are housed in cavities of the bone matrix called lacunae. Osteocytes are interconnected through slender canals called canaliculi, which are only several hundred nm in diameter. The osteocyte network plays a central role in sensing the mechanical signals (mechanosensation). The morphology of the lacuno-canalicular network (LCN) is believed to be related to the mechanosensation and mechanotransduction processes of osteocytes (Schneider et al., 2010, Lanyon, 1993, Burger & Klein-Nulend, 1999, Zhou et al., 2009, Wang *et al.*, 1993a, Weinbaum et al., 1994, McCreadie et al., 2004, Vatsa et al., 2008, van Hove et al., 2009, Currey, 2003, Mullins et al., 2007). Furthermore, the LCN ensures the transport of cellular waste and nutrients (Burger & Klein-Nulend, 1999). Additionally, the LCN has been reported to be essential for micro-crack repair by triggering bone remodeling (Currey, 1984a).

In addition to their mechanosensitive function, osteocytes are hypothesized to regulate the metabolism of bone mineral (Westbroek et al., 2002, Nakashima et al., 2011). Well-balanced osteoblast and osteoclast activity is crucial in maintaining bone mass and structure in healthy bone tissue and is altered in bone diseases such as osteoporosis. In the course of osteoporosis or the development of bone metastasis, treatment with bisphosphonates (BP) is a common intervention to suppress bone resorption by inhibiting osteoclast activity (Dhillon & Lyseng-

Williamson, 2008, Liberman et al., 1995). A severe and most often irreversible adverse effect of high-dosage BP treatment is the potential occurrence of osteonecrosis of the jaw (Mercer *et al.*, 2013, Allen & Ruggiero, 2009). Although multiple hypotheses have been formulated recently, the underlying pathophysiological mechanisms of bisphosphonate-related osteonecrosis of the jaw (BRONJ) are still not completely understood (Otto et al., 2010, Bertoldo et al., 2007). In animal models it was possible to show that the bone turnover of jaw bone is higher in comparison to other sites (Huja *et al.*, 2006, Vignery & Baron, 1980), which is potentially explained by high stress and tooth movement (Bertoldo et al., 2007). Osteocytes might be involved in the pathogenesis of BRONJ.

Given its increasingly acknowledged importance, interest in 3D imaging of the lacuno-canalicular network (LCN) has recently increased, mainly carried out using confocal microscopy (Kerschnitzki et al., 2011, Verbruggen et al., 2012), which has the disadvantage of a limited penetration depth. Ptychographic X-ray CT has been demonstrated as a feasible method to resolve the 3D LCN with sub-micron resolution (Dierolf et al., 2010). Serial section scanning electron microscopy (Reznikov et al., 2013) also provides sub-micron resolution but has so far only been applied to demineralized tissues.

The degree of mineralization in the vicinity of the LCN in mice bone has recently been shown to be accessible using an X-ray microscope with a 208 nm pixel size (Nango et al., 2013). Recently, it has been demonstrated that synchrotron phase nano-tomography (SR-PNT) allows the 3D imaging of mass density with an isotropic voxel size ranging down to 60 nm in a field of view larger than 100x100x100 μm^3 (Langer et al., 2012b, Varga *et al.*, 2013). In comparison to conventional attenuation tomography, phase imaging is several orders of magnitude more sensitive to changes in mass density.

In an exploratory study (Chapter 3.1) we used synchrotron radiation CT with attenuation contrast to investigate the osteocyte lacunar geometrical properties in human jaw bone on the sub-micron length scale, based on five jaw bone samples originating from two healthy subjects and three patients suffering from BRONJ.

In a second study (Chapter 3.2) we included a larger set of human bone sections originating from the femoral site (N=7), the tibial site (N=3), BRONJ (N=10) and healthy jaw bone (N=9) and investigated the alterations of mass density and 3D osteocyte lacunar properties using synchrotron μCT in combination with a phase retrieval.

We speculated that the uptake of BP is linked to the turnover time and addressed the following research questions:

(i) Given the higher turnover rate of the jaw, we analyzed whether the mean mass density of human jaw bone is also lower than that of other anatomical sites.

(ii) Since BP suppresses osteoclast activity and therefore turnover time, we then asked if the mean mass density of jaw bone originating from patients suffering BRONJ was higher compared to jaw sections originating from controls.

(iii) Reduced osteoclast activity results in a decreased amount of mineral being available from remodeling processes. We thus raised the question as to whether the volumes of osteocyte-lacunae are increased in BRONJ when compared to controls, due to the direct remodeling of the lacunar wall in order to maintain mineral homeostasis.

Moreover, in a further study presented in Chapter 3.3. we hypothesized that the morphology of the LCN is altered by BP treatment and may have relevance for the course of BRONJ. Thus, (iv) we quantified the morphology of the canalicular network and the bone tissue properties in the vicinity of the LCN using synchrotron radiation nano-CT in combination with a phase retrieval and compared these properties between human jaw bone originating from both healthy subjects and patients treated with bisphosphonates.

It has been speculated that not only the lacunae but also the canaliculi are involved in processes related to mineral homeostasis (Qing & Bonewald, 2009). However, a direct mineral exchange at the canalicular boundaries could not be shown so far. We hypothesized that tissue maturation takes place via a diffusion process occurring through the interface of the extracellular fluid with the mineralized matrix of both the lacunar and canalicular surfaces, resulting in mass density gradients with respect to the distance to these pore boundaries. These gradients would depend on the (unknown) effective diffusion constant and tissue age. Aiming to assess whether diffusion occurs at all LCN boundaries or only at the lacunar surface we (v) investigated tissue properties independently in the lacunar and canalicular vicinities for bone regions with different tissue ages, namely osteonal tissue, interstitial tissue and tissue originating from BP treated patients. We included considerations regarding the morphology of the LCN to potentially explain and differentiate the impact of short-term

mineral fluctuations in the fluid and the impact of tissue maturation during secondary mineralization on the appearance of mass density gradients.

2 BACKGROUND

2.1 BONE

In this chapter, a brief overview of how bone is structured and how it works to fulfill its multi-fold functions will be given. It must be noted that the considerations focus on cortical human bone and on the micron to sub-micron scale.

2.1.1 GENERAL DETAILS ON BONE STRUCTURE AND FUNCTION

According to Wolff's law, it is believed that form follows function. The shape of bone on the organ level depends on the anatomical site and the function it has to fulfill. The frontal bone of the skull has to protect the brain, while the femur, for example, is a load bearing bone, which at the same time enables walking, in interaction with muscles and tendons. Furthermore, bone is important for mineral homeostasis. In summary, bone has to support, protect, allow for locomotion and participate in mineral homeostasis.

Bone marrow is found inside long bones such as the femur. The bone marrow is a mature component for the lymphatic system and also the site of hematopoiesis, the generation of blood cells.

Bone is a biological material structured in a hierarchical way over several length scales, from the molecular level of collagen to the organ level (Fratzl & Weinkamer, 2007, Weiner & Traub, 1992, Rho et al., 1998), see Fig. 2-1. Apparent bone quality in terms of strength, for example, depends on bone properties at all scale lengths. Bone is able to adapt to mechanical conditions through permanent remodeling (Fig. 2-2).

The main constituents of bone are water, collagen and hydroxyapatite (HA). Bone is infiltrated by bone cells, the most abundant ones are osteocytes. There are approximately as many as 20000 – 40000 osteocytes per mm^3 in cortical bone.

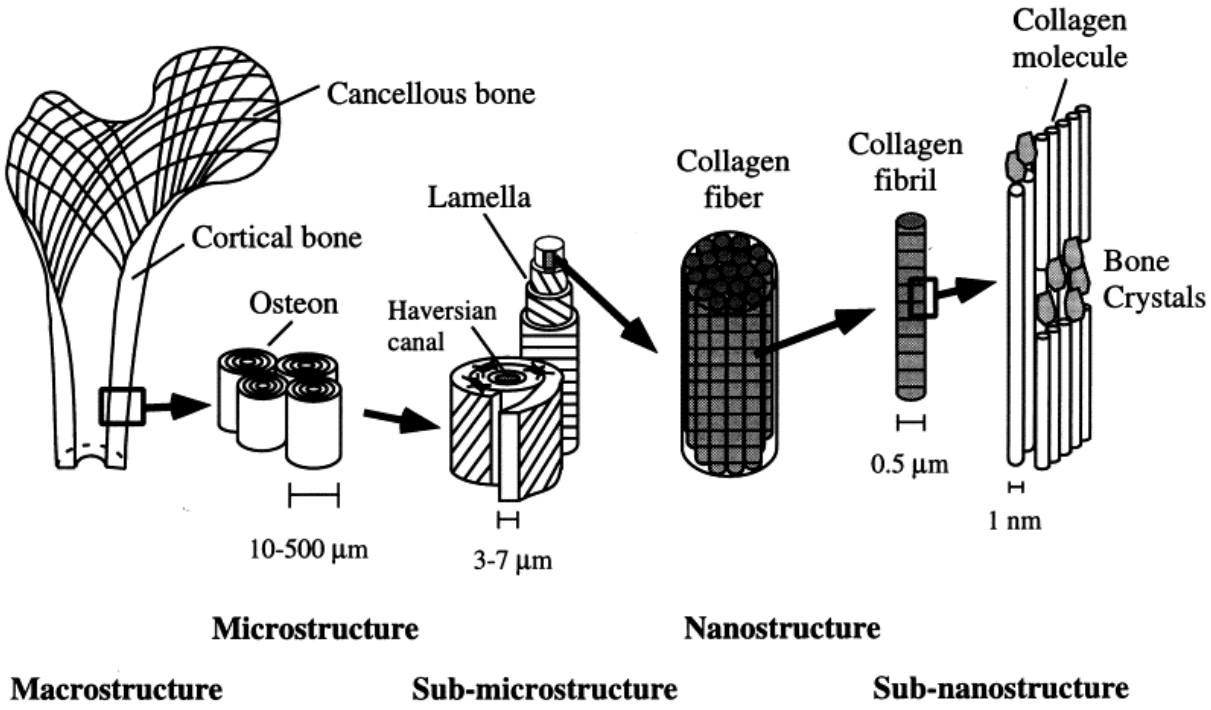

Fig. 2-1 The hierarchical structure of bone from the macro-scale to the sub-nanoscale. (from (Rho et al., 1998))

2.1.2 MODELING AND REMODELING OF BONE

Under healthy conditions bone undergoes continuous remodeling to adapt to spatially and temporarily (such as after a period of long bed rest or a space flight (LeBlanc *et al.*, 2007)) variable demands. This takes places through a delicate equilibrium of resorption and formation which is performed by osteoclast and osteoblast cells, respectively. Osteoclasts, the bone resorbing cells, are large multi-nuclei cells of up to 40 µm in diameter and with 15-20 nuclei. A thorough description of osteoclast function can be found in (Vaananen *et al.*, 2000). The mono-nuclei osteoblasts are bone forming cells. Osteoid, the extracellular matrix that consists mainly of Type I collagen, is formed by osteoblasts. After osteoid is formed, the osteoblast is also responsible for mineralization of the extracellular matrix. The osteoblast differentiates into osteocyte after it is trapped in its own formed extracellular matrix. Osteocytes are interconnected with each other via cell processes housed in canals called canaliculi. Newly formed osteonal bone maturation takes place during a rapid primary and a slower secondary increase in mineralization. This increase requires the supply and precipitation of mineral into the bone matrix. The delivery of mineral can only occur via

interstitial fluid, through interfaces such as the Haversian system and the pore network of osteocytes. Stimulated by biological and mechanical signals (Klein-Nulend *et al.*, 2013), osteocytes are believed to orchestrate the activity of osteoclasts and osteoblasts.

The fundamental functional unit of human bone is the osteon (or Haversian system). An osteon is cylindrical in shape and about 0.1 µm - 0.5 µm in diameter. The central tunnel, called the Haversian canal, contains the blood vessels and nerves. Concentric layers of bone matrix containing the bone cell network surround the Haversian canal. The regions between adjoining osteons are called interstitial tissue. Each osteon is separated from the surrounding bone matrix by a highly mineralized wall called the cement sheath.

Bone remodeling results in a heterogeneous distribution of mineralized tissue units with variable degrees of mineralization. This heterogeneity can be assessed from the distribution of bone mineralization density.

The apoptosis of osteoytes, the process of programmed cell death, is believed to have an important role in initiating the remodeling process (Jilka *et al.*, 2013). In micropetrosis (Frost, 1960), the lacuna is filled up with hypermineralized tissue. The appearance of highly mineralized occlusions (pearls) in the lacunae has been proposed as an intermediate step of this process (Carpentier *et al.*, 2012) and has been observed in both aging (Busse *et al.*, 2010) and bone diseases (Carpentier et al., 2012).

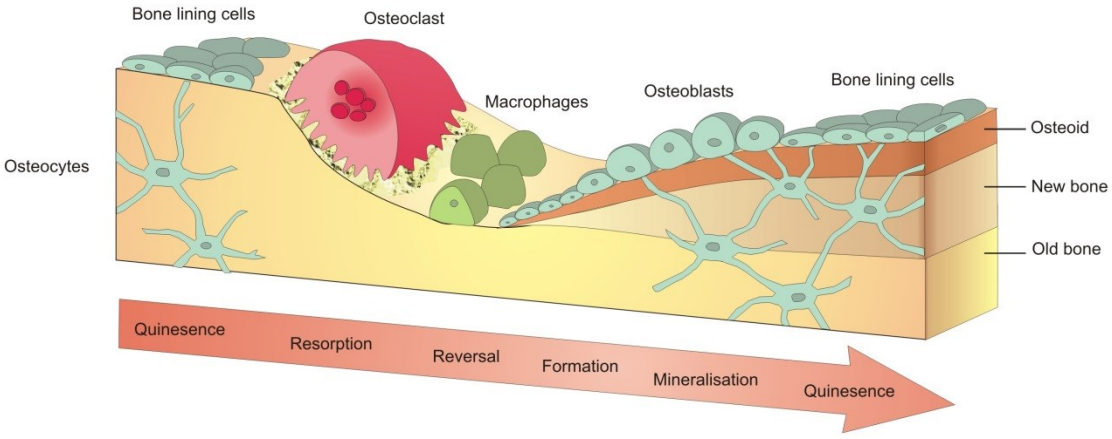

The bone remodelling process.
Bone is continuously remodelled at discrete sites in the skeleton in order to maintain the integrity of the tissue. During this process, old bone is resorbed by osteoclasts and replaced with new osteoid, secreted by osteoblasts. First osteoclasts are activated, and the resorption phase takes approximately 10 days. Following resorption, unclassified macrophage-like cells are found at the remodelling site in the intermediate, or reversal phase. Osteoblast precursors are then recruited , which proliferate and differentiate into mature osteoblasts, before secreting new bone matrix. The matrix then mineralises to generate new bone and this completes the remodelling process. Copyright BTR©

Fig. 2-2 Schematic drawing of the remodeling process performed by osteoclasts resorbing the mineralized bone matrix. New bone is subsequently laid down by osteoblasts. With kind permission from: http://www.york.ac.uk/res/btr/Image%20Library/Bone%20remodelling.jpg

2.1.3 BONE METABOLISM BEYOND OSTEOBLAST/OSTEOCLAST ACTIVITY

After the process of initial mineralization, which is still part of the process of remodeling described in the previous section, a *secondary mineralization* process takes place, which adds about 10 % more mineral over a period of several years (Parfitt, 2003). In (Parfitt, 2003) it is also outlined that an average turnover of about 12 % per year at a total body calcium of 1000 g and a bone loss of about 1 % per year leads to a net calcium flux of about 30 mg out of an adult skeleton each day. However, much larger fluxes of calcium between the extracellular fluid (ECF) and the bone matrix have been reported than could be explained through osteoblast/osteoclast activities (Parfitt, 2003, Marenzana *et al.*, 2005, Pirklbauer & Mayer, 2011).

It is believed that osteocytes resolve calcium from the peri-lacunar space and replace it according to demand, in order to maintain calcium homeostasis (Atkins & Findlay, 2012). The process of calcium removal from the peri-lacunar matrix is called osteocytic osteolysis (Belanger *et al.*, 1967) and it has recently became the object of research again (Qing & Bonewald, 2009, Teti & Zallone, 2009). It is believed that the calcium concentration in the ECF is controlled by the parathyroid hormone (PTH) (Talmage & Mobley, 2008), a non-collagenous protein. This study also reports that it is via PTH that the concentration of

calcium in the ECF is elevated from the basic level of 35 mg/l to the required physiological level of 50 mg/l. Excess mineral ions are limited by the renal threshold for calcium which has to be coordinated with the processes of mineral exchange at the ECF-bone matrix interface by PTH (Talmage & Mobley, 2008). A large amount (~ 90 %) of the ECF-bone interface makes up the lacuna-canalicular surface (Atkins & Findlay, 2012).

The role of non-collagenous proteins in regulating the mineralization process is of great interest in literature (Hunter *et al.*, 1996). For example, non-collagenous proteins which are found at the borders of the collagen matrix attached to the minerals in the ECF inhibit crystal growth, while crystals that are not in contact with non-collagenous protein in the collagen matrix grow normally (Talmage & Mobley, 2008). The authors of (Talmage & Mobley, 2008) conclude that the calcium movement into and out of hydroxyapatite is due to crystal growth and crystal dissolution, respectively. These two processes appear through equilibrium processes at the surfaces (Talmage & Mobley, 2008) and potentially explain the stability of the calcium supply demanded by all kinds of physiological processes.

2.1.4 THE OSTEOCYTE-LACUNAR CANALICULAR NETWORK

Osteocytes are the most abundant bone cells, embedded in small cavities (lacunae) of the extracellular matrix during the deposition of new tissue during remodeling. They are interconnected and communicate via cell processes extending into slender tunnels called canaliculi, see Fig. 2-3 and Fig. 2-4. Lacunae are some hundreds of μm^3 in size, while the diameter of the canaliculi in human bone is in the range of 200-900 nm (Marotti *et al.*, 1995). Osteocytes are involved in bone remodeling and mineralization as they orchestrate the delicate equilibrium between osteoclast and osteoblast activity through their ability to sense biological and mechanical signals (Bonewald, 2011, Klein-Nulend et al., 2013). However, the details of mechanosensation and mechanotransduction processes are not yet fully understood (Klein-Nulend et al., 2013, Schneider et al., 2010, Zhou et al., 2009, Wang et al., 1993a). The morphology of the lacuno-canalicular network (LCN) plays a crucial role in mechanosensation (Anderson & Knothe Tate, 2008, Knothe Tate, 2003, Knothe Tate, 2011) and is related to bone tissue quality (Schneider et al., 2010, Kerschnitzki *et al.*, 2013) and has been reported to be adapted to the anatomical location (Carter *et al.*, 2013b, Mishra & Knothe Tate, 2003). Furthermore, given the close relationship between bone diseases and remodeling, the osteocyte is believed to have particular importance and has recently gained increasing

attention. LCN morphology is believed to be altered in various bone diseases although little data is available (Mullender *et al.*, 1996, Qiu *et al.*, 2003, Mullender *et al.*, 2005, van Hove et al., 2009). Furthermore, the LCN ensures the transport of cellular waste and nutrients (Burger & Klein-Nulend, 1999). The LCN has also been reported to be essential for micro-crack repair by triggering bone remodeling (Currey, 1984b). The role of osteocytes in the metabolism of phosphate has recently been investigated (Nakashima et al., 2011, Feng *et al.*, 2013). Moreover, a recent study in mice demonstrated osteocytic osteolyis during lactation (Qing *et al.*, 2012), confirming that osteocytes also actively participate in calcium homeostasis. Alterations in lacunar size have also been observed in response to changes in the mechanical environment, e.g. enlarged lacunae have been reported in mice after space flights (Blaber *et al.*, 2013), or after glucocorticoid treatment (Lane *et al.*, 2006). Both lacunar size and density were found to be altered in newly-formed bone after antiresorptive and anabolic pharmaceutical treatment in ovariectomized rats (Tommasini *et al.*, 2012). The distribution of osteocytes is thus not only crucial for proper sensing of mechanical signals across the bone matrix, but also for easy access to mineral reservoirs. The distance between the extracellular tissue and the LCN is therefore of particular importance and has recently been demonstrated to be strongly related to the thickness and orientation of mineral particles (Kerschnitzki et al., 2013). The canalicular network provides a direct interface with the bone tissue which is much larger and much closer to the mineralized matrix compared to the interface formed by the lacunar walls (Kerschnitzki et al., 2013). It has therefore been hypothesized that cell dendrites are involved in the active role of the osteocytes in tissue remodelling (Kerschnitzki et al., 2013, Qing et al., 2012, Qing & Bonewald, 2009). However, no measurement could support this hypothesis so far, due to the lack of adequate three-dimensional quantitative imaging modalities at the length scales of the canaliculi (Webster *et al.*, 2013).

Whether bone cell dendrites can penetrate through the cement line is controversial: cell dendrites are connected through the cement wall (Milovanovic *et al.*, 2013), and the cement wall disrupts the connections of the cells at the boundary of the osteon (Kerschnitzki et al., 2011).

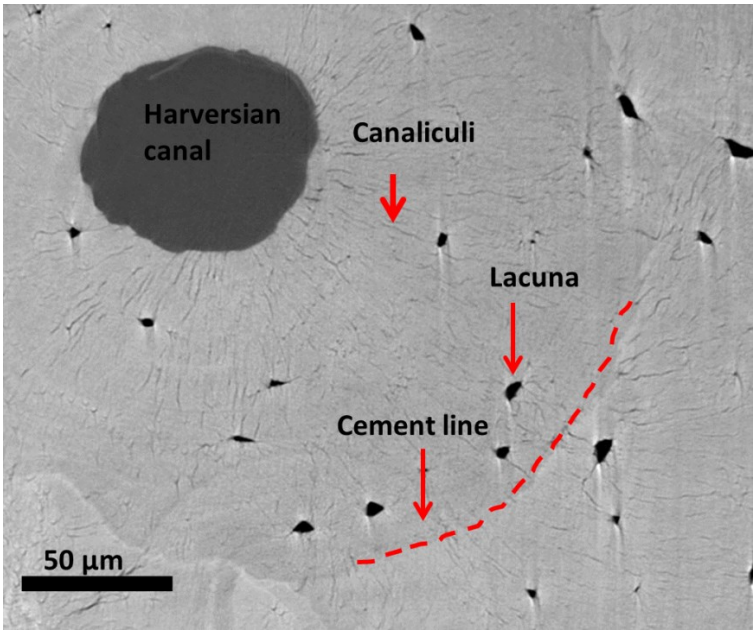

Fig. 2-3 Reconstructed slice obtained through synchrotron radiation µCT of human cortical jaw bone, for details of image acquisition see section 3.1.2.2 . The osteocyte-lacunae and the canaliculi network can be seen (indicated). The gray color corresponds to attenuation, with brighter gray corresponding to a higher attenuation. The osteonal tissue separated from the interstitial tissue by the cement line (indicated) appears less bright, indicating a higher mineralization of the interstitial tissue.

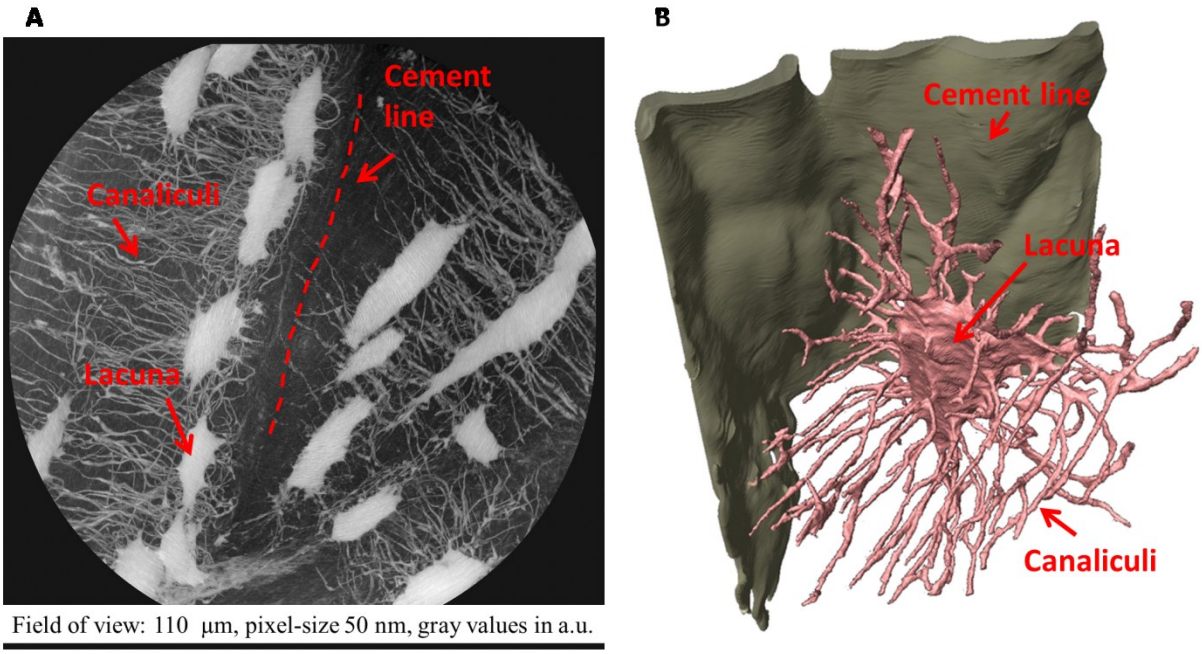

Fig. 2-4 A minimum intensity projection illustrating the high connectivity of the osteocyte lacunae through the canalicular network. The cement line separating bone units formed at different points in time is visible and no intersections of the canaliculi are apparent. For details of image acquisition see section 3.3.2.2B: Volume rendering of an osteocyte lacuna and its canaliculi. (Reprinted from (Langer et al., 2012b))

2.1.5 Bisphosphonate Related Osteonecrosis of the Jaw

A well-adjusted level of osteoclast vs. osteoblast activity is crucial in healthy tissue and is altered in bone diseases such as osteoporosis. In the course of osteoporosis or development of bone metastasis, treatment with bisphosphonates (BP) is one common intervention to suppress bone resorption by inhibiting osteoclast activity (Dhillon & Lyseng-Williamson, 2008, Liberman et al., 1995). A severe and usually irreversible adverse effect of high-dosage BP treatment is the potential occurrence of osteonecrosis of the jaw (2009, Ruggiero *et al.*, 2009, Mercer et al., 2013, Kuhl *et al.*, 2012, Allen & Ruggiero, 2009). Although multiple hypotheses have been formulated recently, the underlying pathophysiological mechanisms of bisphosphonate related osteonecrosis of the jaw (BRONJ) are still not completely understood (Lesclous *et al.*, 2009, Otto et al., 2010, Meiller *et al.*, 2012, Bertoldo et al., 2007).

In animal models it has been shown that the bone turnover of jaw bone is higher compared to other sites (Huja et al., 2006, Vignery & Baron, 1980), a potential explanation for which is

high stress and tooth movement (Bertoldo et al., 2007). Whether or not the uptake of BP in the jaw bone is increased compared to other anatomical sites is controversially discussed in a pilot study. Using a rat model, the uptake of BP in the jaw bone was found to be similar to the uptake of BP in long bones (Bauss *et al.*, 2008) while others concluded that the uptake of BP depends on bone turnover (Cremers *et al.*, 2005, Bertoldo et al., 2007). In fact, in (Bauss et al., 2008) the BP concentration was determined in whole-bone hydrolyzates using gas chromatography, thus local concentration could not be assessed. In addition to this, the administration time of 9 days could be too short in comparison to the bone turnover time in order to observe the impact of turnover on BP deposition. In (Bertoldo et al., 2007) the potential cause of BRONJ is proposed to be based on an increase of BP concentration over time, until a critical concentration is reached and a triggering event such as tooth extraction occurs. The trigger event causes locally high doses of BP to be released, which induces osteoclast apoptosis and slows wound healing. The wound region becomes more sensitive to infection and finally results in osteomyelitis and osteonecrosis (Fig. 2-5).

Another potential explanation for the cause of BRONJ relies on the toxicity of BP at high doses (Allen & Burr, 2008), which are reached in the jaw bone due to the increased deposition.

Another hypothesis is that the BP accumulation of bone is sufficient enough to be directly toxic for the oval epithelium, causing the healing of soft tissue lesions to fail, e.g. due to injuries during tooth removal. The failure of wound healing could then lead to secondary infection of the underlying bone and BRONJ (Reid *et al.*, 2007).

Otto et al. (Otto et al., 2010) speculated whether the pH level is the “missing part in the pathogenesis puzzle”. They argue that BP binds to bone at a neutral pH level, and the dissociation between BP and bone mineral takes place during bone resorption under acid pH conditions. Further, they conclude that an infection can lead to a reduced pH level, resulting in an increased release of BP from the bone. Eventually, “it is conceivable that BP-derivatives specific toxic levels are exceeded in response to a prolonged or localized acidification, which in turn may trigger the cascade of pathways that cumulate in BRONJ” (Otto et al., 2010).

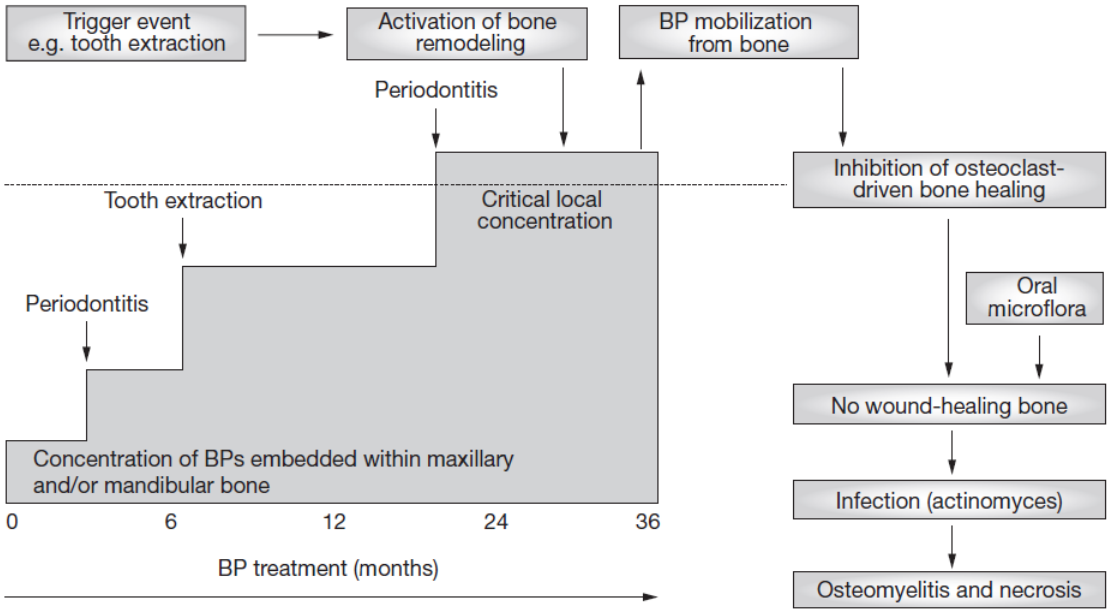

Fig. 2-5 Mechanism of bisphosphonate accumulation in the jaw and a hypothetical pathogenic role in osteonecrosis. During BP treatment, dental procedures or periodontal pathology that induce high cellular turnover in alveolar bone facilitate the preferential accumulation of BPs in the maxillary and/or mandibular bone. When a critical concentration of BP in the bone is achieved, a trigger event (e.g. a tooth extraction) activates bone remodeling and may release locally pharmacological doses of BPs that then inhibit osteoclast-driven bone healing. The contamination of the bony wound by oral microflora (i.e. by a member of the Actinomycesgenus) induces necrotic osteomyelitis. The timing of BP treatment is provided as an example. Abbreviation: BP, bisphosphonate. Figure and caption from (Bertoldo et al., 2007), reprinted with kind permission from NPG.

2.2 IMAGING OF BONE AT THE MICRON AND SUBMICRON SCALE

Since bone is a highly hierarchical material the apparent properties (such as resistance against external forces, or the degree of mineralization) of which may depend on substructures: properties at the coarser length scale are determined by the structure at the finer scales. Assessment on the micro/nano length scales may help to understand how bone adapts to fulfill its multifold functions. In this thesis, we imaged bone in 3D by means of synchrotron radiation computed tomography on the micron and sub-micron scale. In this chapter, a brief overview of other imaging modalities on the micron and sub-micron length scale will be given and compared in terms of strengths and weaknesses. A more detailed comparison may be found in (Webster et al., 2013).

2.2.1 2D IMAGING AT THE MICRON AND SUB-MICRON SCALE

There are various ways of imaging bone in 2D on the micron length scale. All microscopy modalities using visible light are limited in spatial resolution, due to diffraction to about 0.2 µm. In histology, where thin sections of tissue are stained, different tissue types can be differentiated.

When imaging with monochromatic light, such as light emitted by LASER, electronic transitions can be investigated, giving access to the molecular properties of the probed specimen, such as in Raman spectroscopy (Raghavan, Sahar et al. 2012). For many molecules the electronic transitions are tabulated and characterization of the sample then becomes possible. This method can be extended by using polarized light because the probability that electronic transitions can be induced by the light depends on the polarization of the incoming light. However, the principle remains the same. Many studies based on Raman spectroscopy were performed on bone, e.g. (Hofmann *et al.*, 2006), (Isaksson *et al.*, 2010), (Paschalis *et al.*, 2001). Similarly to Raman, infrared light absorption spectroscopy gives access to the chemical properties of the probed volume (Boskey & Pleshko Camacho, 2007, Paschalis *et al.*, 1996).

When moving away from visible light, which has an energy in the order of 1 eV, towards waves with shorter wavelengths such as X-rays, which have energies in the order of 1000 to 100 000 times higher than visible light (Fig. 2-6), much smaller features can be observed as the wavelength is reciprocally proportional to the energy. The high energy does not only enable the investigation of states of the outer electrons but also those of the inner electrons.

While the energy levels of outer electrons are specific to the chemical composition and environment of the probed material, the energy-levels of the inner electrons are specific to the element the electron belongs to. Using X-ray fluorescence techniques, elemental composition can be obtained (Pemmer *et al.*, 2013), with the spatial resolution depending on the optics and investigated elements. At the same spatial resolution, chemical properties such as coordination and bonding length can be obtained using X-ray absorption spectroscopy (Laurencin *et al.*, 2010). Crystalline morphology, for example the thickness of HA, can be obtained using X-ray diffraction techniques (Li *et al.*, 2010, Kerschnitzki et al., 2013).

Electron microscopy has been extensively used to study bone on the micron and sub-micron length scale, for example using techniques such as quantitative backscattered electron imaging (qbei) (Ruffoni *et al.*, 2007, Roschger *et al.*, 2008, Bach-Gansmo *et al.*, 2013). To image bone on the sub-micron scale and gain access to the ultrastructure, scanning electron microscopy has proved to be suitable (Mahamid *et al.*, 2011b, Reznikov et al., 2013). Alteration of the canalicular network with tissue age was recently investigated across two-dimensional planes using an acid etching technique in combination with electron microscopy (Milovanovic et al., 2013).

Mapping of mechanical properties of bone can be obtained using techniques such as nano-indentation (Rodriguez-Florez, Oyen et al. 2013), atomic force microscopy (Milovanovic *et al.*, 2012) or scanning acoustic microscopy (Raum, 2008).

2.2.2 3D IMAGING AT THE MICRON AND SUB-MICRON SCALES

The 3D assessment of the LCN and its surrounding bone matrix is of great interest for understanding bone functions (e.g. mechanosensation, osteocyte osteolysis). In the past, 3D imaging of the LCN has been mainly carried out using confocal microscopy (Kerschnitzki et al., 2011, Verbruggen et al., 2012, McCreadie et al., 2004) with the disadvantage of limited in-depth information. Ptychographic X-ray CT proved to be feasible in order to 3D resolve the LCN on the sub-micron scale (Dierolf et al., 2010), with the disadvantage of long acquisition times. Serial section scanning electron microscopy (Reznikov et al., 2013) allows for sub-micron resolution but is still challenging in terms of measuring time due to the sectional nature of the technique and thus fully destructive. The degree of mineralization in the vicinity of the lacuanar-canalicular network in mice bone was recently shown to be accessible using an X-ray microscope at 208 nm pixel size (Nango et al., 2013).

Synchrotron Radiation micro-computed tomography (SR μCT) enables 3D imaging of bone tissue at the cellular length-scale and has been shown to be an appropriate tool for investigating 3D lacunar morphology (Carter et al., 2013b, Dong *et al.*, 2013a, Carter *et al.*, 2013a, Hesse *et al.*, 2013 UNDER REVIEW, Dong *et al.*, 2013b, Vatsa et al., 2008, van Hove et al., 2009, Hannah *et al.*, 2010).

Recently, it has been demonstrated that synchrotron phase nano-tomography (SR-PNT) enables 3D images of mass density with an isotropic voxel size ranging down to 60 nm in a field of view larger than 100x100x100 μm^3 (Langer et al., 2012b, Varga et al., 2013). Another key property of this technique is that it is orders of magnitude more sensitive to differences in mass density than conventional synchrotron absorption tomography. The amount of time for collecting a full holotomographical scan is approximately 2 hours.

2.3 X-RAY COMPUTED TOMOGRAPHY

In this chapter a brief introduction will be given concerning X-rays and the interactions of X-rays with matter, followed by an introduction into X-ray computed tomography. A short background description of synchrotron radiation will be given, describing in particular the tomography setups installed at ID19 and ID22 (now ID16) at the ESRF.

2.3.1 FUNDAMENTAL PRINCIPLES OF X-RAYS

Like visible light, X-rays are electromagnetic waves (Fig. 2-6) that can be characterized by their wavelength and amplitude. X-rays, first discovered by W.C. Röntgen[1] in 1895, became an important tool, not just for medical applications or material research. See Fig. 2-7 for one of the first X-ray images ever. Ever since the discovery of X-rays, X-ray sources have been constantly increasing their power, ranging from rather simple X-ray tubes to synchrotrons and free electron lasers. Electromagnetic waves with energies higher than those of ultraviolet light are called soft X-rays. X-ray energies above 5 -10 keV are called hard X-rays. The energy, E, of an electromagnetic wave depends on its wavelength: $E = h\frac{c}{\lambda}$, with h being Planck's constant[2], c being speed of light, and λ the wavelength. The wavelength and angular frequency, ω, are related via $c = \lambda\frac{\omega}{2\pi}$.

---

[1] Wilhelm Conrad Röntgen (1845 - 1923) was a German physicist. He earned the first Nobel Prize in Physics in 1901 for his discovery of the X-rays.

[2] Max Karl Ernst Ludwig Planck (1858 – 1947) was a German theoretical physicist who won the Nobel Prize in Physics in 1918 for his quantum theory.

h= 6.62606957(29) 10^{-34} Js

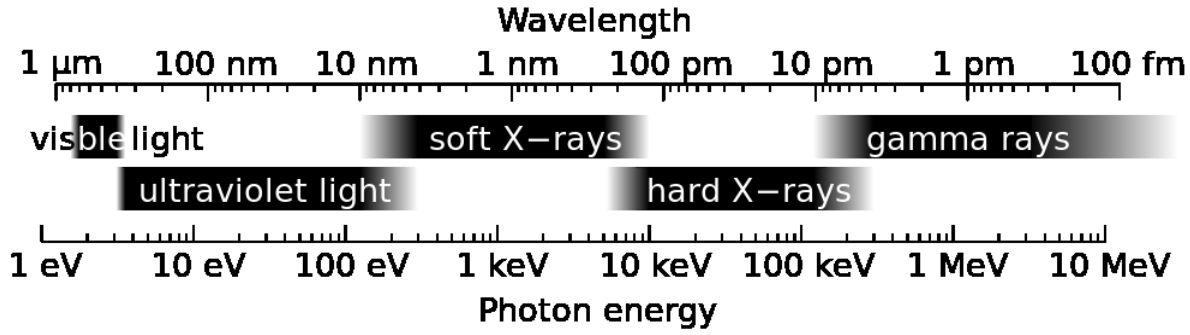

Fig. 2-6. Part of the electromagnetic spectrum showing photon energies and their corresponding wavelengths. (http://commons.wikimedia.org/wiki/File:X-ray_range.svg)

Fig. 2-7 One of the first x-ray pictures ever. It shows the hand of Röntgen's wife and was presented in Freiburg in January 1896. (from Wikimedia commons: http://commons.wikimedia.org/wiki/File:First_medical_X-ray_by_Wilhelm_R%C3%B6ntgen_of_his_wife_Anna_Bertha_Ludwig%27s_hand_-_18951222.gif*)*

2.3.2 X-RAY INTERACTION WITH MATTER

The interactions of X-rays with matter strongly depend on the energy of the X-ray beam and of the element considered for interaction. In the following, a very brief overview of the main interactions will be given. The following description of X-ray interaction with matter follows nomenclature and argumentation from (Als-Nielsen & McMorrow, 2011). The interaction of X-rays with matter forms the foundation for X-ray imaging or diagnosis.

2.3.2.1 Scattering

X-ray scattering can be attributed to either inelastic (Compton) or elastic (Thomson) scattering.

Compton scattering (inelastic scattering)

In Compton[3] scattering, the scattered X-ray beam has a smaller energy than the incident beam. In the simplest case, Compton scattering by a free electron, the incident beam transfers energy to the electron. The change in wavelength is proportional to the Compton scattering length defined by

$$\lambda_C = \frac{2\pi}{mc} = 0.00386\ \text{Å}\,, \qquad (2\text{-}1)$$

with m being the mass of the particle. The ratio of the energy of the incoming photon (E^i) and that of the scattered photon (E^f) can be expressed as:

$$\frac{E^i}{E^f} = \frac{\lambda^f}{\lambda^i} = 1 + \lambda_C k(1 - cos\,\Psi)\,, \qquad (2\text{-}2)$$

The wavelength, λ^i, of the incoming X-ray is related to the length of the wavevector, **k**, through $k = \frac{2\pi}{\lambda^i}$, λ^f denotes the wavelength of the scattered X-ray. The scattering angle, Ψ, is

[3] Arthur Holly Compton (1892 - 1962) was an American physicist. In 1927 he earned the Nobel Prize for his discovery of the Compton-effect.

the angle between the initial and the final propagation direction of the X-ray. The phenomenon described in Eq. 2-2 is known as the Compton effect.

Thomson scattering (elastic scattering)

The Thomson[4] scattering length is equal to the classical electron radius r_0:

$$r_0 = \frac{e^2}{4\pi\epsilon_0 mc^2} = 2.82\ 10^{-5}\ \text{Å}, \qquad (2\text{-}3)$$

with *e* being the charge of the electron, and ϵ_0 being the electric constant.

The ratio of Compton and Thompson scattering length is called the fine structure constant and is equal to about 1/137.

Considering the scattering from an atom, and treating the electrons as a charge cloud surrounding the nucleus with a number density, $\rho(\mathbf{r})$, the charge in a volume element $d\mathbf{r}$ at position $\mathbf{r}$ is $-e\,\rho(\mathbf{r})\,d\mathbf{r}$. The total number of electrons, Z, in the atom is then equal to the integral over $\rho(\mathbf{r})$. The wave vector transfer $\boldsymbol{Q}$ is defined as $\boldsymbol{Q}=\boldsymbol{k}^i-\boldsymbol{k}^f$, the superscripts i and f indicating the initial and final state, respectively. In order to calculate the scattering amplitude, all contributions in $d\mathbf{r}$ must be weighted by the phase vector $e^{i\boldsymbol{Q}\cdot\boldsymbol{r}}$, integration over $d\mathbf{r}$ gives (in units of $-r_0$) :

$$f^0(\boldsymbol{Q}) = \int \rho(\boldsymbol{r}) e^{i\boldsymbol{Q}\cdot\boldsymbol{r}} d\boldsymbol{r} \qquad (2\text{-}4)$$

For $Q \rightarrow 0$, the integral of the charge density becomes equal to Z. If $\lambda^{\mathbf{i}}$ becomes smaller compared to the size of the atom, destructive interference of the waves scattered from the electron in the atom occurs, which results in $f^0(\boldsymbol{Q}) = 0$ for $Q \rightarrow \infty$.

$f^0(\boldsymbol{Q})$ is called atomic form factor or atomic scattering length. It is the Fourier[5] transform of the charge distribution.

---

[4] Sir Joseph John Thomson (1856 - 1940) was a British physicist. He was awarded the 1906 Nobel Prize for Physics for the discovery of the electron and his work on the conduction of electricity in gases.

The elements considered in the present work are generally smaller than 2 Å; 2 Å wavelength of an X-ray corresponds to 6.2 keV.

The considerations made regarding scattering from an atom can be extended to molecules or even crystals. Further interference effects must then be taken into account; a more profound description of these can be found in (Als-Nielsen & McMorrow, 2011). The scattering described above is discussed in terms of classical Thomson scattering from free electrons, known as kinematical diffraction.

Allowing the electrons to be bound, the model of the atomic scattering length, written in units of $-r_0$, can be elaborated to:

$$f(Q,\omega) = f^0(Q) + f'(\omega) + if''(\omega) \qquad (2\text{-}5)$$

where $f'$and f'' are the real and imaginary parts of the dispersion corrections which are frequency dependent (ω denotes the to the X-ray energy corresponding frequency). They are also related to absorption. The dispersion corrections become most important when the energy is close to the energy of the absorption edges, they are also called resonant scattering terms. The dispersion corrections are mainly dominated by electrons of the K-edges, see below.

Photoelectric Absorption

When the energy of the incoming photon, E^i, is bigger than the binding energy of an electron in the atom of an inner shell electron, E^{bind}, the electron can leave the atom and will have a kinetic energy of $E^{kin} = E^{bind} - E^i$. This effect is called photoelectric absorption. The created hole in the inner shell is subsequently filled by an electron from an outer shell. The energy released by this transmission can either cause a fluorescence X-ray emission or the emission of a secondary outer electron, which is called an Auger electron, see Fig. 2-8. Auger[6] transitions are more probable for lighter elements, while the emission of a fluorescence photon becomes dominant for elements with higher atomic numbers. The monochromatic fluorescent X-rays give a unique relation to the kind of atom observed.

---

[5] Jean Baptiste Joseph Fourier (1768-1830) was a French mathematician and physicist.

[6] Pierre Victor Auger (1899-1993) was a French physicist who worked in the fields of atomic and nuclear physics and in cosmic ray physics.

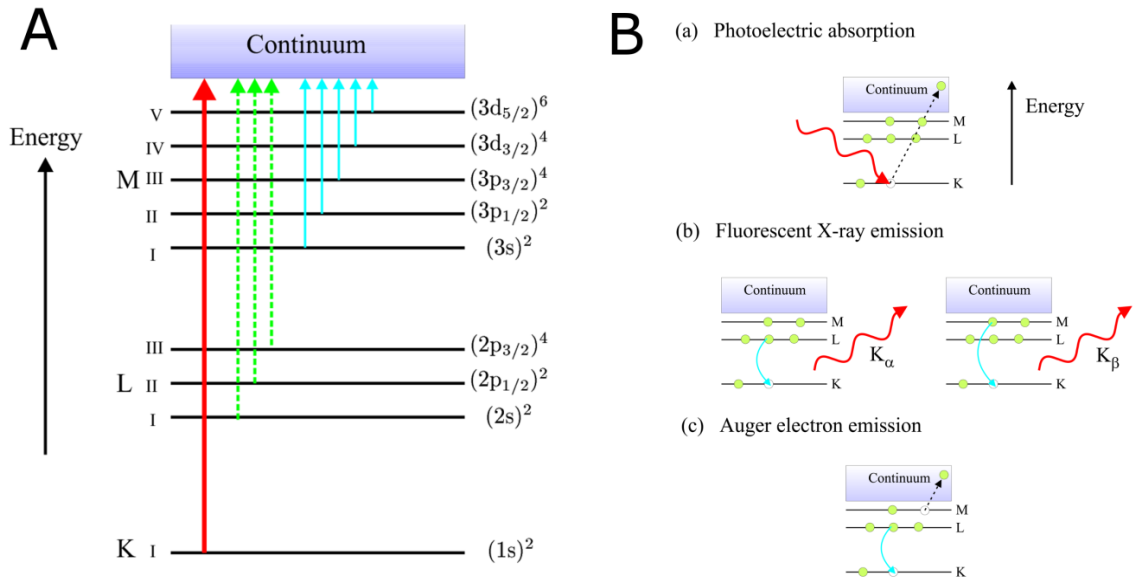

Fig. 2-8 Summary of the nomenclature for labeling the absorption edges is shown in A. The schematic energy level diagram of an atom is shown in B: The created hole in an inner shell, here the K shell, is subsequently filled by an electron from an outer shell which has less binding energy. The difference in binding energy is released by either emitting a fluorescent X-ray (b) or an Auger electron (c). (b): Here the outer electron comes from the L-shell, causing K-α emission (b- left side) or from the M-shell causing K -β emission (b- right side). (c): If the energy through the relaxation process is transferred to an electron with less binding energy than the one which fills the hole, it can leave the atom with a kinetic energy, E^{kin}. (Images takes from (Als-Nielsen & McMorrow, 2011))

The photoelectric absorption of the X-ray beam strongly depends on the atomic number, Z, and the X-ray energy, E, varying approximately as Z^4 and E^{-3}.

The transmission, T, of an X-ray through a homogeneous sample of thickness z is given by:

$$T = \frac{I}{I_0} = e^{-\mu z} \qquad (2\text{-}6)$$

where I and I_0 are the intensities of the X-ray after and before passing the sample, respectively. μ denotes the linear absorption coefficient:

$$\mu = \frac{N_A}{A}\rho_m\sigma_{tot} \quad (2\text{-}7)$$

where N_A, A, ρ_m and σ_a are Avogadro's number[7], atomic mass number, mass density and total absorption cross-section, respectively. To illustrate, the left panel of Fig. 2-9 shows the linear attenuation coefficient of two materials for a range of energies. For the X-ray regime σ_{tot} can be expressed as the sum of cross-sections due to photoelectric absorption ($\sigma_{photoelectric}$), elastic ($\sigma_{elastic}$) and inelastic ($\sigma_{Compton}$) scattering.

Comparison of the cross sections

In (Wang, 2007) the different cross sections due to elastic and inelastic scattering and photoelectric absorption are summarized using several approximations. There it is shown that the amplitude of the elastic scattering is about proportional to *Z/E*. The square of this amplitude gives the intensity, or cross section:

$$\sigma_{elastic} \propto \left(\frac{Z}{E}\right)^2. \quad (2\text{-}8)$$

For inelastic scattering the cross section due to the scattering for the X-ray regime is approximated to be:

$$\sigma_{Compton} \propto Z. \quad (2\text{-}9)$$

And finally, the cross section due to photoelectric effect is approximately proportional to:

$$\sigma_{photoelectric} \propto \frac{Z^5}{E^{3.5}}. \quad (2\text{-}10)$$

[7] Lorenzo Romano Amedeo Carlo Avogadro di Quaregna e di Cerreto (1776 -1856) was an Italian scientist. As a tribute to him, the number of elementary entities in 1 mole of a substance, 6.02214179(30) 10^{23}, is known as the Avogadro constant.

2.3.2.2 The refractive index

The phenomena in visible light where the beam changes its direction when passing through different media is well known and described by Snell's law[8]. For glasses and visible light the refractive index, *n*, is roughly about 1.5 and depends on the energy (or frequency) of the electromagnetic wave. Resonant behavior occurs when the energy of the electromagnetic wave corresponds to electronic transitions. The X-ray energy is generally higher than most of the possible electronic transitions, except for those of the inner shell electrons of heavier elements, resulting in a value for n that is very close to 1 and smaller than 1 for X-rays. In X-rays, the tiny deviation of n from 1 (about 10^{-5}), called δ, leads to a very small critical angle for the total external reflection, α_c. Using Snell's law, one finds that $\alpha_c = \sqrt{2\delta}$.

Refraction and phase shift

A phase shift of $-\pi$ occurs between the incident and scattered wave at each electron. The scattering length for an electron was already shown to be r_0. The refractive index, n, can be derived from the density of electrons and r_0. Neglecting absorption processes the relationship is:

$$n = 1 - \delta \qquad (2\text{-}11)$$

where

$$\delta = \frac{2\pi\rho r_0}{k^2}. \qquad (2\text{-}12)$$

The length of the wavevector **k** is equal to $\frac{2\pi}{\lambda}$, here ρ denotes the electron density. In terms of atomic scattering length and atomic density δ can be written as:

$$\delta = \frac{2\pi\rho_a f^0(0) r_0}{k^2} \qquad (2\text{-}13)$$

where ρ_a denotes the atomic number density. This equation can be formulated in terms of numbers N_j of atoms of a certain element *j* and mass density, ρ, to

[8] Willebrord Snellius (1580 - 1626) was a Dutch astronomer and mathematician. His name has been linked to the law of refraction of light. It is now known that this law was already discovered by others hundreds of years earlier.

$$\delta = \frac{\lambda^2 r_0 Z \rho_a}{2\pi} = \frac{\lambda^2 r_0 N_A}{2\pi} \rho \frac{\sum_j N_j Z_j}{\sum_j N_j A_j} = \frac{\lambda^2 r_0 N_A}{2\pi} \rho \frac{\sum_j Z_j}{\sum_j A_j}. \quad (2\text{-}14)$$

For most elements the ratio of $\frac{Z_j}{A_j}$ is about 0.5. With this approximation the Eq. 2-14 can be written as

$$\delta \approx \frac{\lambda^2 r_0 N_A}{2\pi} \rho \frac{1}{2} = \frac{r_0 N_A}{4\pi} \rho \lambda^2 \approx 1.35\ 10^{-6}\ \rho \lambda^2 \quad (2\text{-}15)$$

with ρ in g/cm^3 and λ in Å**,** which results in $\delta \propto \frac{Z}{E^2}$.

If absorption is considered in the refraction process, *n* has to be modified in:

$$n \equiv 1 - \delta + i\beta \quad (2\text{-}16)$$

The wave of incident propagation in the medium with depth *z* can then be expressed as

$$e^{i\mathrm{nkz}} = e^{i\,(1-\delta)\mathrm{kz}}\, e^{-\beta \mathrm{kz}}, \quad (2\text{-}17)$$

where β is linked to the linear absorption length μ through:

$$\beta = \frac{\mu}{2k} \quad (2\text{-}18)$$

Substituting μ by the sum of the cross sections defined in Eq.2-8 to 2-10 gives:

$$\beta \propto \left(\frac{Z^2}{E^3}\right) + \left(\frac{Z}{E}\right) + \left(\frac{Z^5}{E^{4.5}}\right). \quad (2\text{-}19)$$

To illustrate, the ratio of delta to beta is shown in the right panel of Fig. 2-9 for two different materials. There it can be seen that delta is much higher than beta, thus imaging of delta provides a higher sensitivity to the probed material.

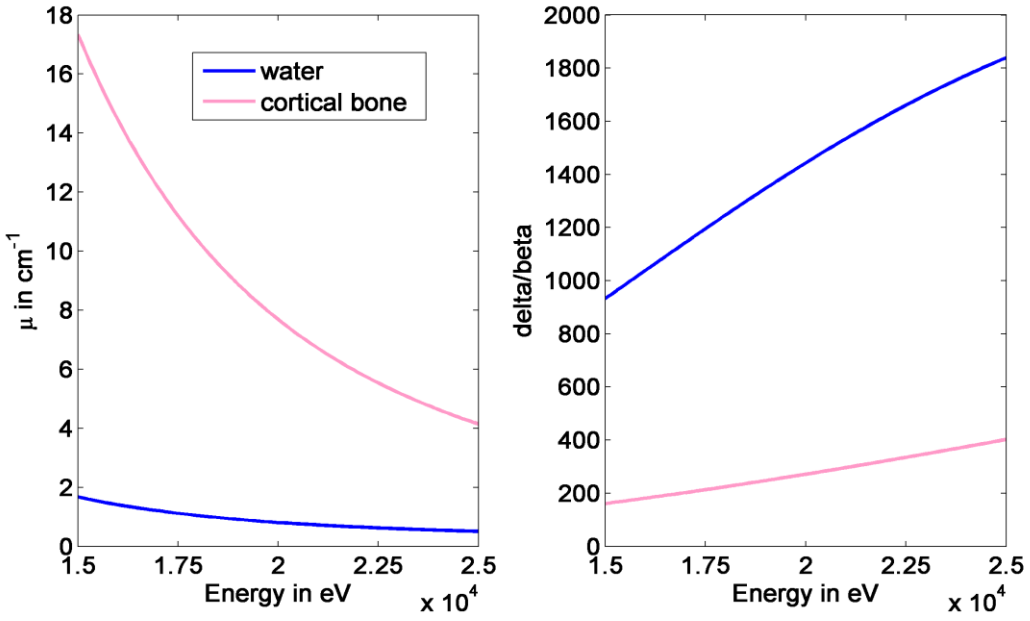

Fig. 2-9 Left: Linear attenuation coefficient for water and cortical bone is plotted for X-ray energies between 15 and 25 keV (values taken from the XOP software (del Río & Dejus, 2004), bone: cortical bone (ICRU-44) (ICRU, 1989)). Note that the linear attenuation coefficient is defined as the mass attenuation coefficient multiplied by the mass density. Right: The ratio of delta to beta is shown for a range of X-ray energies for two different materials.

2.3.3 SYNCHROTRON RADIATION

A synchrotron takes advantage of the fundamental principle that accelerated charged particles emit electro-magnetic radiation. In synchrotron light sources, such as the ESRF, X-rays are generated by accelerated electrons. After electrons are produced by an electron gun, in a concept similar to a normal cathode ray tube, they are pre-accelerated in a linear accelerator and subsequently injected into a so-called booster synchrotron. There they reach their final energy, with which the electrons finally circulate at a constant speed in the storage ring.

In the storage ring the radiation is produced in bending magnets that are used to keep the electrons in a closed orbit, and in insertion devices (ID), namely wigglers and undulators, placed on the straight sections. A commonly used characteristic of a beam is its *brilliance*:

$$Brilliance = \frac{\frac{Photons}{s}}{(mrad^2)(mm^2 source\ area)(0.1\ \%\ bandwidth)}.$$

The definition of brilliance accounts for several beam properties such as (i) number of emitted photons per second, (ii) the collimation of the beam is expressed in units of $mrad^2$, (iii) the source area, and (iv) the spectral distribution (or bandwidth) of the beam. The brilliance of the ESRF (June 2011) is shown in Fig. 2-10.

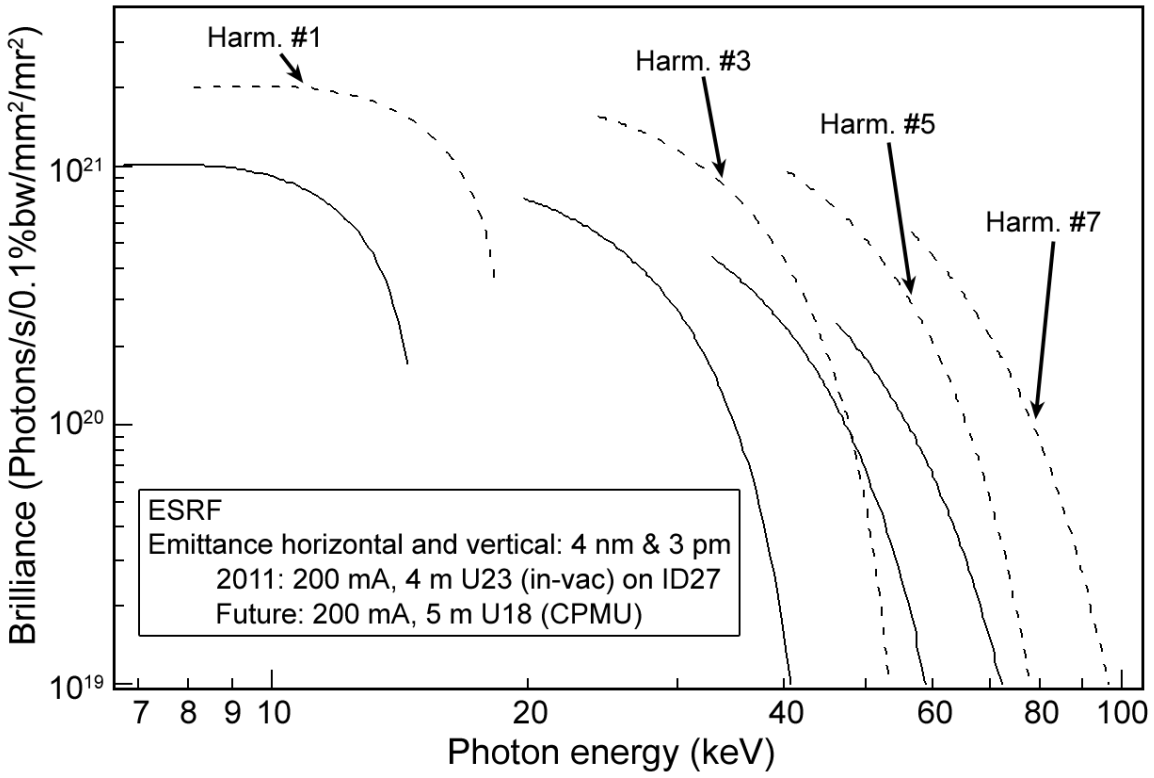

*Fig. 2-10: Brilliance of the ESRF as of June 2011 (*http://www.esrf.eu/Accelerators/Performance/Brilliance*). For comparison, the brilliance produced by X-ray tubes is around 10 orders of magnitude smaller, while X-ray lasers reach peak brilliance of values of up to 10^{30} but in a far smaller range of available energies.*

2.3.4 FUNDAMENTALS OF COMPUTED TOMOGRAPHY

In X-ray computed tomography (CT), tomographic images (or slices) are computed based on X-ray projection images obtained from multiple angles. While the primary goal of this technique was clinical imaging, the technique has spread to many other fields, in particular thanks to the development of micro-CT. Applications of micro-CT range from biomedical imaging (Jensen *et al.*, 2013, Zhao *et al.*, 2012, Langer *et al.*, 2011, Preininger *et al.*, 2012) to material science (Tolnai *et al.*, 2012, Morgeneyer *et al.*, 2008) and paleontology (Pradel *et al.*, 2009, Fernandez *et al.*, 2013). Under certain conditions, quantification of the composition of the inner part of the investigated object is possible. The spatial resolution of desktop micro-CT systems is technically limited by the signal to noise ratio due to the available flux of the X-ray source. However, using synchrotron radiation enables much higher spatial resolution ranging down to less than 100 nm (Varga et al., 2013, Langer et al., 2012b).

2.3.4.1 Principle of CT

The refractive index, n, as a function of the spatial coordinates, $\mathbf{r}(x, y, z)$, $n(\mathbf{r}) = 1 - \delta(\mathbf{r}) + i\beta(\mathbf{r})$ is considered to fully describe the 3D imaged object in the event of using hard X-rays, where propagation and dynamical effects inside the object can be neglected (Langer et al., 2012b). The attenuation and phase shift of the X-ray induced by the object along a straight path through the sample, can be described as projection, p, through β and δ, respectively:

$$A_\theta(\mathbf{r}) = \frac{2\pi}{\lambda} \int \beta(\mathbf{r}) ds \qquad (2\text{-}20)$$

$$\varphi_\theta(\mathbf{r}) = \frac{2\pi}{\lambda} \int \delta(\mathbf{r}) ds, \qquad (2\text{-}21)$$

where the subscript, θ, indicates a given angle of propagation of the X-ray with respect to the sample (see Fig. 2-11 and Fig. 2-12). The coordinate system (x,y,z) may be fixed to the sample with its origin in the center of rotation. It is related to the coordinate system fixed to the X-ray (x_s,y_s,z) by:

$$\begin{pmatrix} x_s \\ y_s \end{pmatrix} = \begin{pmatrix} \cos\theta & \sin\theta \\ -\sin\theta & \cos\theta \end{pmatrix} \begin{pmatrix} x \\ y \end{pmatrix}. \qquad (2\text{-}22)$$

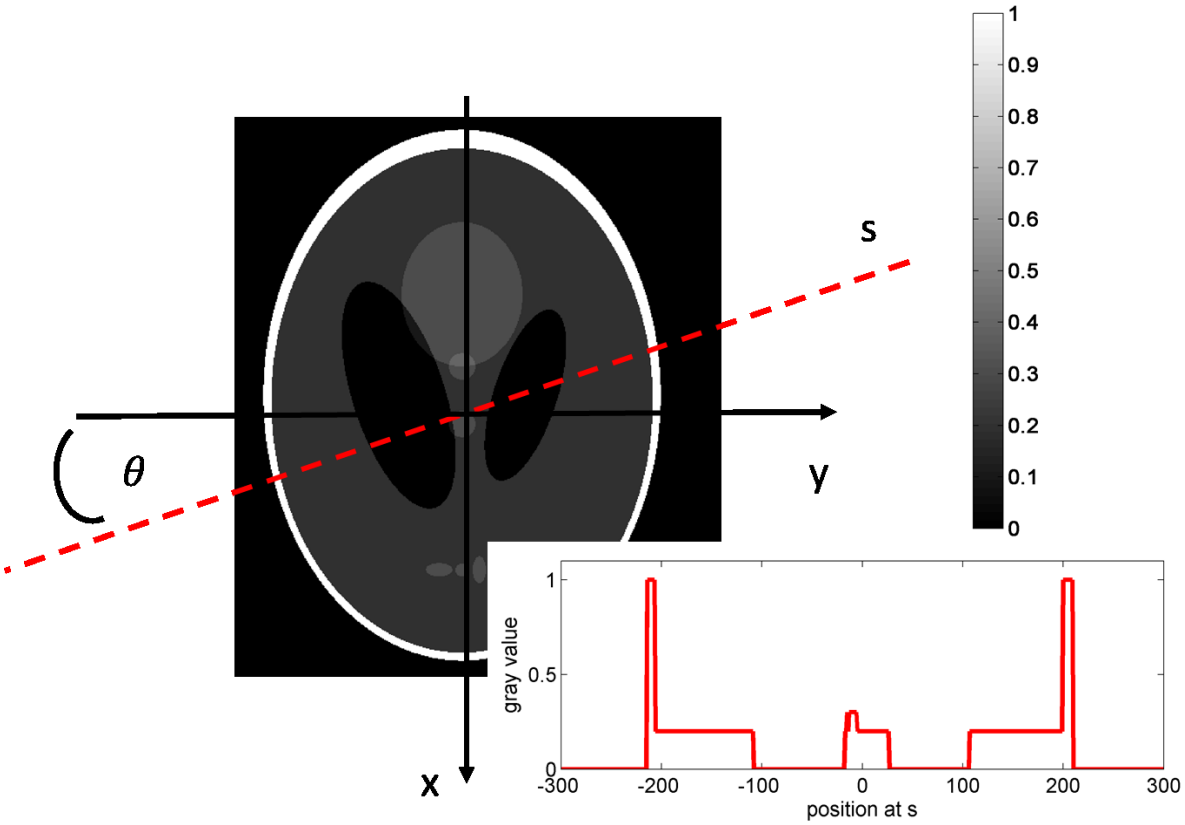

Fig. 2-11 Synthetic 2D data (Shepp-Logan-Phantom) with a gray value range between 0 and 1. x and y are parallel to the plane of the image, if z is perpendicular to x and y. The center of rotation may be the origin of the coordinate system (indicated by the crossing of the x and y axis). For a given angle, θ, the path of a X-ray is indicated by the red dotted line, and the profile of the gray level corresponding to the indicated path is shown in the lower right panel.

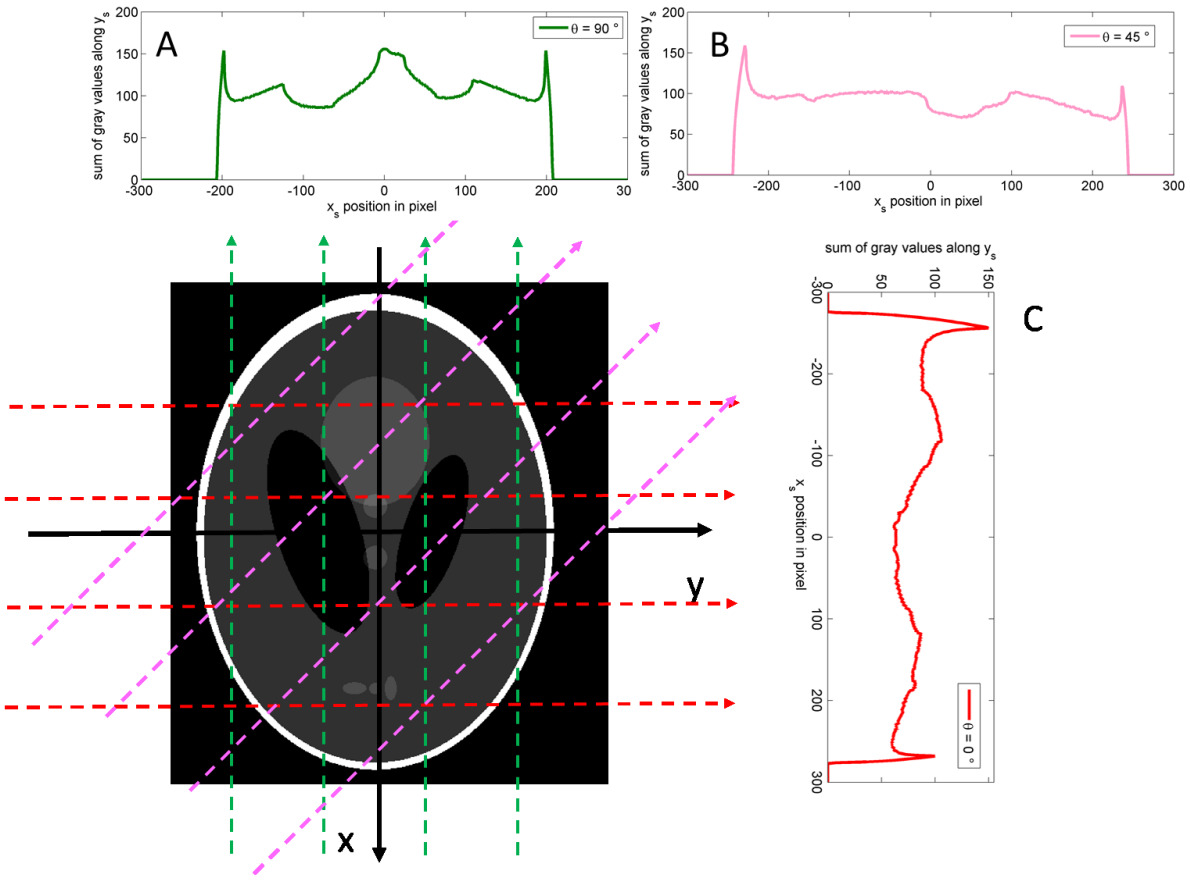

Fig. 2-12 Here the projections through the Shepp-Logan phantom are shown for 0, 45 and 90° of the X-ray with respect to the x axis. In panels A, B and C, x_s denotes the axis perpendicular to the propagation direction of the X-ray and perpendicular to the z-axis. y_s denotes the axis parallel to the X-ray and perpendicular to the z-axis.

The projections $p_\theta(x_s)$ through an arbitrary object function $g(x_s,y_s)$, with x_s,y_s being in the coordinate system of the X-ray beam, can be written as:

$$p_\theta(x_s) = \int g(x_s cos\theta - y_s sin\theta, x_s sin\theta + y_s cos\theta) d\, y_s. \quad (2\text{-}23)$$

The set of all projections when θ and x_s are varying defines the Radon Transform of the object g.

Image reconstruction consists of recovering the image g from its Radon Transform. A major result is the Fourier slice theorem, covered in the next section.

2.3.4.2 Fourier slice theorem

Consider the Fourier transform of a projection $p_\theta(x_s)$

$$\tilde{p}_\theta(R) = \int p_\theta(x_s)\, e^{-2\pi i x_s R} dx_s. \qquad (2\text{-}24)$$

Substituting the definition of the projection (2.23) into this definition gives:

$$\tilde{p}_\theta(R) = \int \int g(x_s cos\theta - y_s sin\theta, x_s sin\theta + y_s cos\theta)\; e^{-2\pi i R x_s} dy_s dx_s. \quad (2\text{-}25)$$

Substituting x_s and y_s with Eq. 2-22 produces the two-dimensional Fourier transform of the object function g with respect to its coordinates *(x,y)*:

$$\tilde{p}_\theta(R) = \int \int g(x,y)\; e^{-2\pi i R(x\, cos\,\theta + y\, sin\,\theta)}\, dy\, dx\,,$$

which can be written as:

$$\tilde{p}_\theta(R) = \tilde{g}\,(R\, cos\,\theta\,, R\, sin\,\theta) \qquad (2\text{-}26)$$

where $u = R\ cos\,\theta$ and $v = R\ sin\,\theta$. This equation is known as the Fourier slice theorem. It means that the Fourier transform of a parallel projection through a 2D object function for an angle θ, is equal to a slice (a line along the direction θ) of the two-dimensional Fourier-transform of the object function (Kak & Slaney, 1988).

If an infinite number of projections through the object for different angles were considered, $\tilde{g}\,(u,v)$ would be entirely known. The object function in real space could then be calculated using its inverse Fourier transform, with $\boldsymbol{u}$*=(u,v)*:

$$g(\boldsymbol{x}) = \int \int \tilde{g}\,(\boldsymbol{u})\, e^{2\pi i \boldsymbol{u}\cdot\boldsymbol{x}}\, d\boldsymbol{u} \qquad (2\text{-}27)$$

However, in practice there are only a finite number of rotation angles and a finite number of pixels in the detector. The transformation from polar coordinates to Euclidean space requires interpolation.

2.3.4.3 Filtered back projection

A more efficient reconstruction technique is the Filtered Back Projection (FBP) algorithm. This method is based on the backprojection operator, which is the dual of the Radon Transform. Intuitively, this operator *Bp* is equal to the sum of the backprojection of all projections and defined as:

$$Bp(x,y) = \int_0^{\pi} p_\theta(x\cos\theta + y\sin\theta)d\theta \tag{2-28}$$

It can be shown that the backprojection of all projections provides a convoluted version of the original object. However, if the projections are first filtered with an appropriate filter before backprojection, the original object can be directly obtained: this defines the FBP algorithm. It can be written as:

$$g(\boldsymbol{x},\boldsymbol{y}) = \int_0^{\pi} q_\theta(x\cos\theta + y\sin\theta)d\theta, \tag{2-29}$$

with q being the convolution of p_θ and a filter h(x_s):

$$q_\theta(x_s) = (p_\theta * h)(x_s) = \int p_\theta(x_s')h(x_s - x_s')dx_s'. \tag{2-30}$$

$$g(x,y) = B(p_\theta * h) \tag{2-31}$$

With a detector with *N* horizontal pixel the number of projections, *M*, needed to archive a sufficient sampling in the Fourier space can be approximated as:

$$M \approx \frac{\pi}{2}N.$$

To illustrate, a Radon-transform corresponding to a 2D phantom is shown in Fig. 2-13. Reconstructions for different numbers of projections are illustrated in Fig. 2-14.

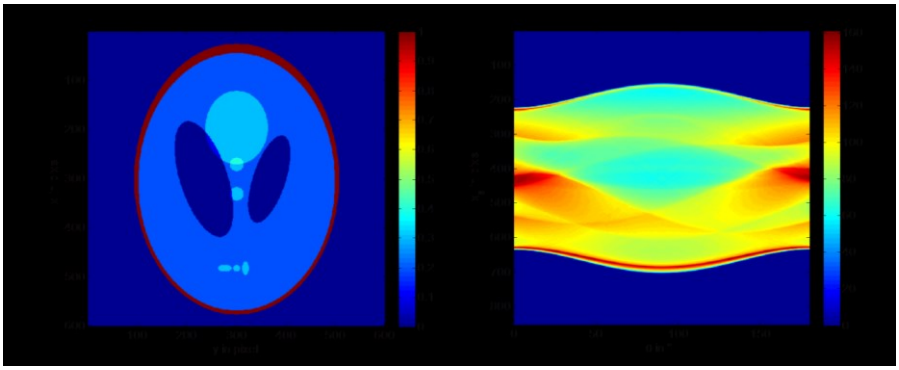

Fig. 2-13 A: 2D phantom (Shepp-Logan phantom) of 600 by 600 pixel size. Color bar in grey-level units between 0 and 1. B: to a corresponding Radon transform calculated for 500 projection angles with equal step width between 0 and 180 degrees. The color bar corresponds to the sum of the intensities along the respective line. The coordinates were introduced in the previous section.

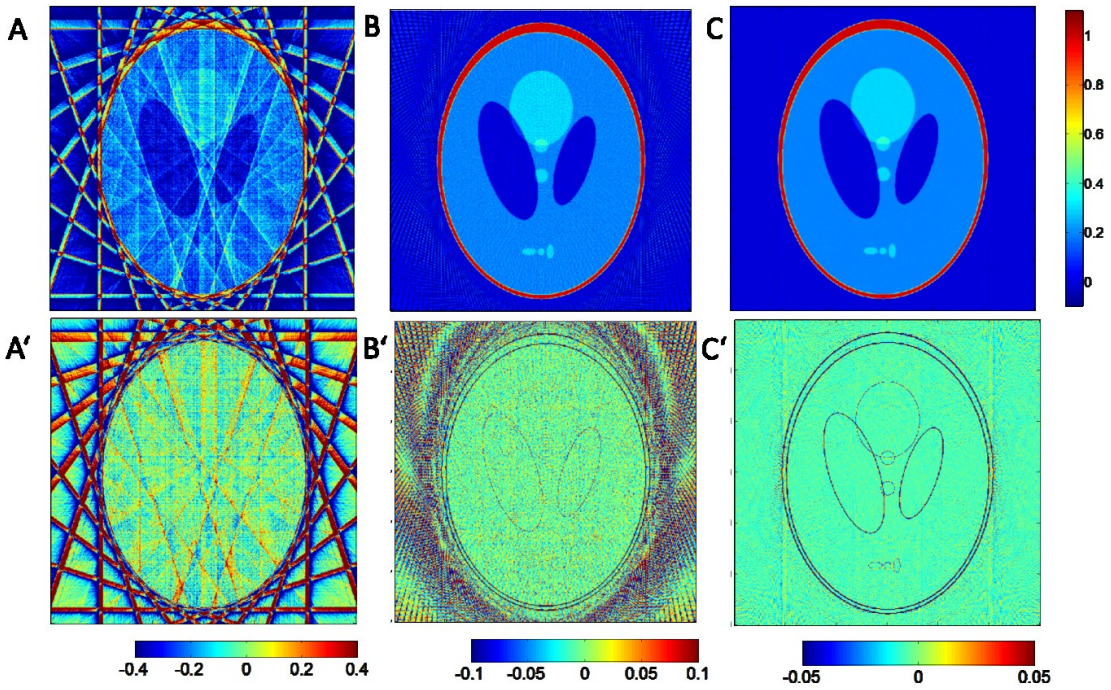

Fig. 2-14 A, B and C show inverse radon transformations based on 10, 100 and 500 projections of the radon transform of the Shepp-Logan phantom, respectively. The color-bar for images A, B and C is shown on the right. A', B' and C' show the subtractions of the original Shepp-Logan phantom from the reconstructed ones shown in A, B and C. The computation of A, B and C is done in Matlab using the radon and iradon functions. The stripes visible in A' demonstrate the artifact caused by too few projections which cause under-sampling in the Fourier space.

2.3.5 RETRIEVING THE PHASE SHIFT

In previous sections it was shown that the phase shift induced by the object when the X-ray passes through can be more pronounced than the attenuation of the X-ray on the same path (Fig. 2-9).

In the present work, the phase retrieval is restricted to propagation-based methods, based on leaving some space between the sample and the detector in order to allow for Fresnel diffraction caused on micro structures, which will lead to interference. The phase maps are then recorded at the detector.

However, retrieving the phase from the phase map may be complicated. Once the phase is retrieved from the recorded projections it can be used as input to reconstruct the 3D distribution of δ of the object using the filtered back projection algorithm, for example. In the following, I will briefly introduce two different phase retrieval algorithms.

2.3.5.1 Paganin approach

The algorithm to retrieve the induced phase shift suggested by David Paganin (Paganin *et al.*, 2002) is non-iterative, based on imaging at one sample detector distance. In the Paganin method, the phase is retrieved using the assumption of a linear relationship between the absorption index (β) and the refractive index decrement (δ). The δ/β ratio for a given energy has to be used as input. For example, for cortical bone (ICRU-44) (ICRU, 1989), the δ/β ratio at an energy of 16.87 keV has to be set to 199, based on the XOP software (del Río & Dejus, 2004). The high δ/β ratio demonstrates the higher sensitivity of imaging the phase (δ) compared to imaging the attenuation (β).

The setup has to meet some conditions, which have to be fulfilled even though in practice some variations from the following requirements are tolerable (Weitkamp *et al.*, 2011) in order to calculate the phase shift induced by the imaged object from the measured intensity distribution in the detector. These are: (1) the imaged object consists of a single homogenous material, (2) a monochromatic and (3) plane incident wave is used, (4) the distance, d, between imaged object and detector fulfills the near-field condition.

The near-field condition is: $d \ll \frac{s^2}{\lambda}$, where s is the size of the smallest discernible feature in the object and λ, the wavelength of the incident wave. In practice the critical distance, d_c,

should be smaller than $\frac{(2\Delta)^2}{\lambda}$, Δ being the pixel-size of the detector (Weitkamp et al., 2011). A radiograph with phase contrast is shown in Fig. 2-15. A slice reconstructed after the Paganin method and FBP is shown in Fig. 2-16. The impact of different δ/β ratios on the outcome of the reconstructed slice using the Paganin method is illustrated in Fig. 2-17 and Fig. 2-18. There, it can be seen that the increased sensitivity is apparently countered by a blurring of the image (Fig. 2-17) which results in a loss of spatial resolution and a broadening of the histogram of the intensities Fig. 2-18.

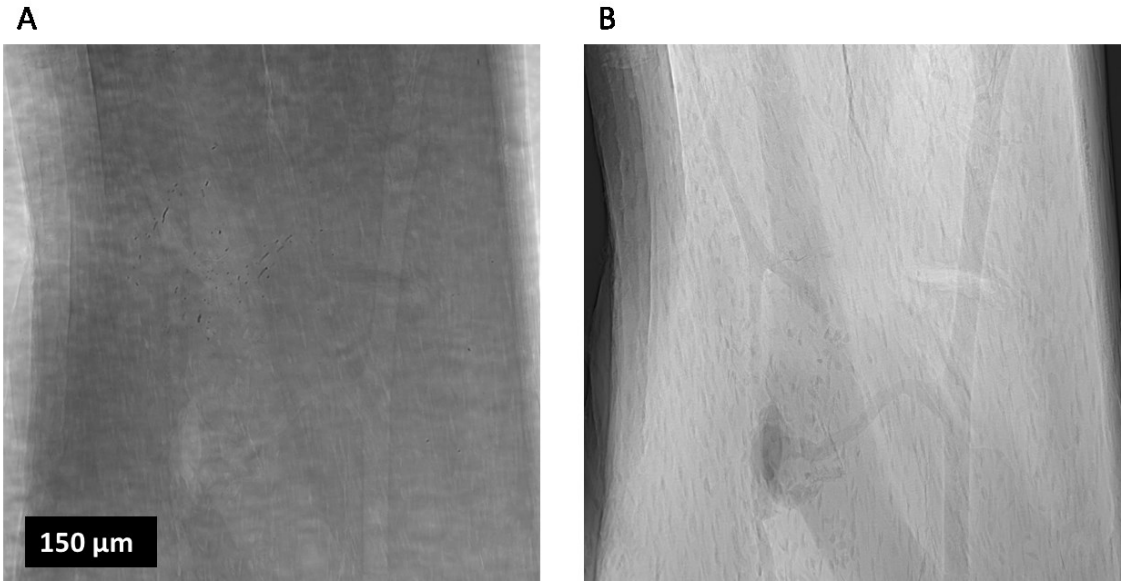

Fig. 2-15 A: Phase contrast radiograph through a cortical piece of bone measured on ID19, pixel-size 300 nm, E=19 keV, d~ 10 mm. B is the same image after flat-field correction (log(I_0-dark/I-dark)).

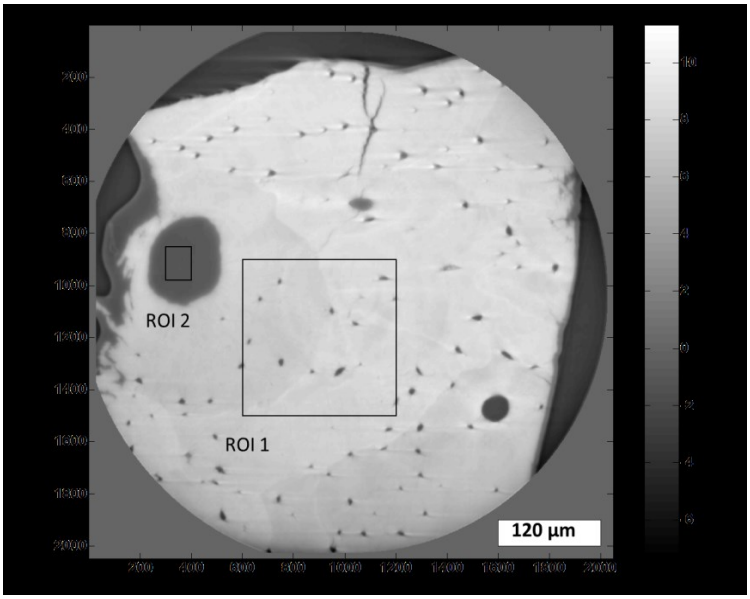

Fig. 2-16 Reconstructed slice using Paganin's method (delta/beta=250 according to the theoretical value at E=19keV). The reconstructed attenuation (µ in 1/cm) may be corrupted, as the full specimen is not inside the field of view. Furthermore, artifacts are visible, caused by motion of the sample during the scan. This motion is very likely due to cracking of the sample, since a motion correction was performed which overcame any kind of linear motion.

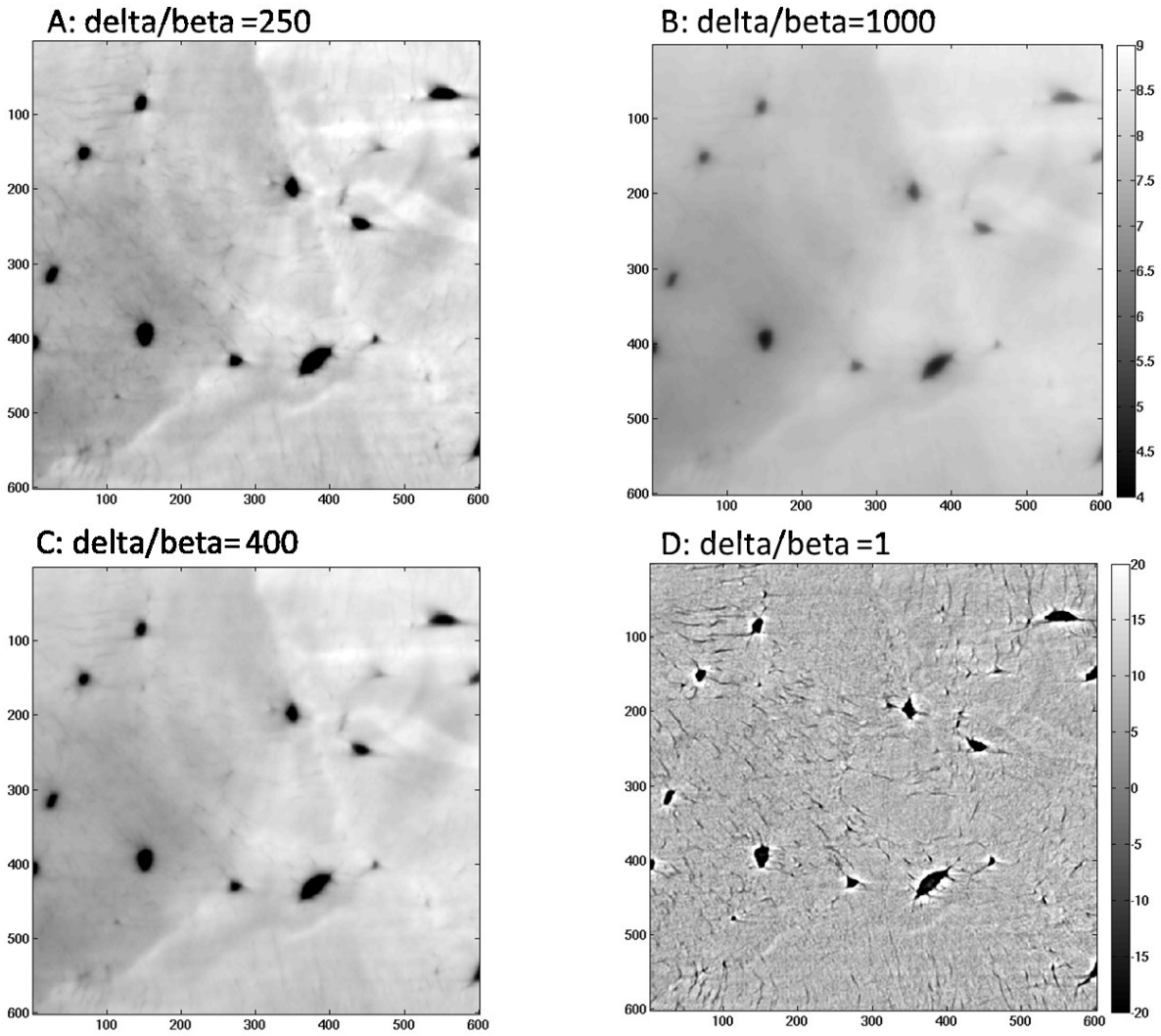

Fig. 2-17 ROI1, as indicated in the previous figure, is shown for reconstructed slices using different delta/beta ratios. The same color bar is used for A, B and C, while in D the color bar is extended to adjust to the contrast. It can be seen that differentiation of the different tissue types (osteonal vs. interstitial tissue) is easier in the reconstructions A, B and C. However, the increased sensitivity is apparently countered by a blurring of the image which results in a loss of spatial resolution.

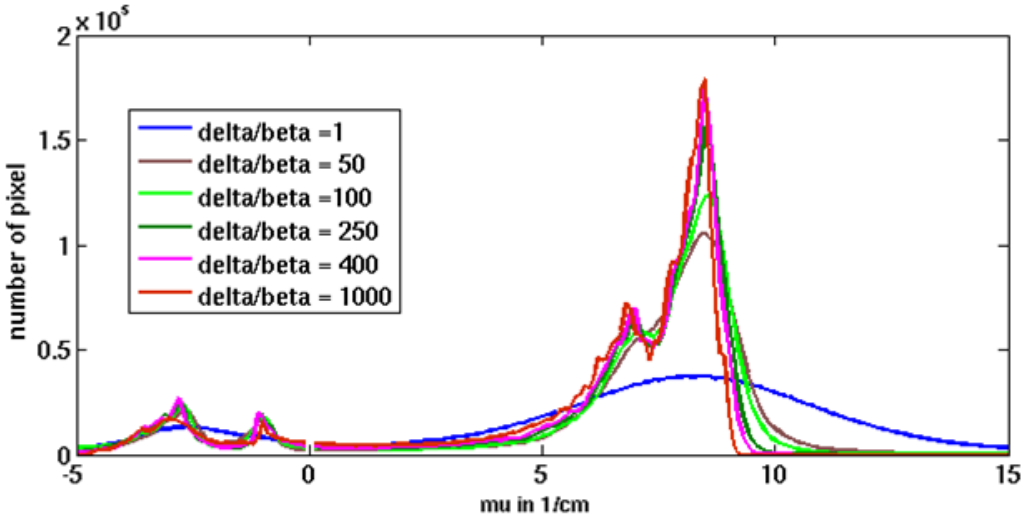

Fig. 2-18 Histograms of the attenuation distributions for different δ/β ratios of ROI 1 (see Fig.2-16). It can be seen that the width of the peaks corresponding to bone-tissue are narrower for higher δ/β ratios, indicating a higher sensitivity to the mass density of the bone-tissue.

2.3.5.2 X-ray in-line phase tomography towards heterogeneous objects

Although the Paganin method is computationally rather fast and only radiographs at one distance, d, have to be collected, the disadvantages are clearly that the imaged object has to be homogeneous and the *δ/β* ratio has to be known.

Linearized solutions based on several distances have been proposed to quantitatively determine the refractive index decrement (Cloetens *et al.*, 1999) and compared using simulated and experimental phantoms (Langer *et al.*, 2008). However, the correct determination of the low frequencies from the Fresnel diffraction patterns is challenging, due to the weak transfer of low frequency information by the Fresnel transform. The introduction of prior knowledge in the object domain has been proposed to allow for non-homogeneous sample compositions (Langer *et al.*, 2012a). Recently, it has been shown that knowledge about the object composition gained from the attenuation index-based reconstruction can be used as a prior in the phase retrieval, (see Fig. 2-19 a) (Langer *et al.*, 2014). There the priors are based on an empirical relationship between the refractive and the attenuation index. In a first step, the attenuation index of the imaged object is reconstructed, ideally for a distance of zero between imaged object and detector. The found empirical relationship serves then as an

initial estimation of the refractive index and a forward projection of this estimate at each projection angle is finally used to construct the phase maps (Langer et al., 2014), see Fig. 2-19-d. However, the composition of the imaged object must still be roughly known. In imaging of bone, where the composition is fairly well known, this technique appears promising.

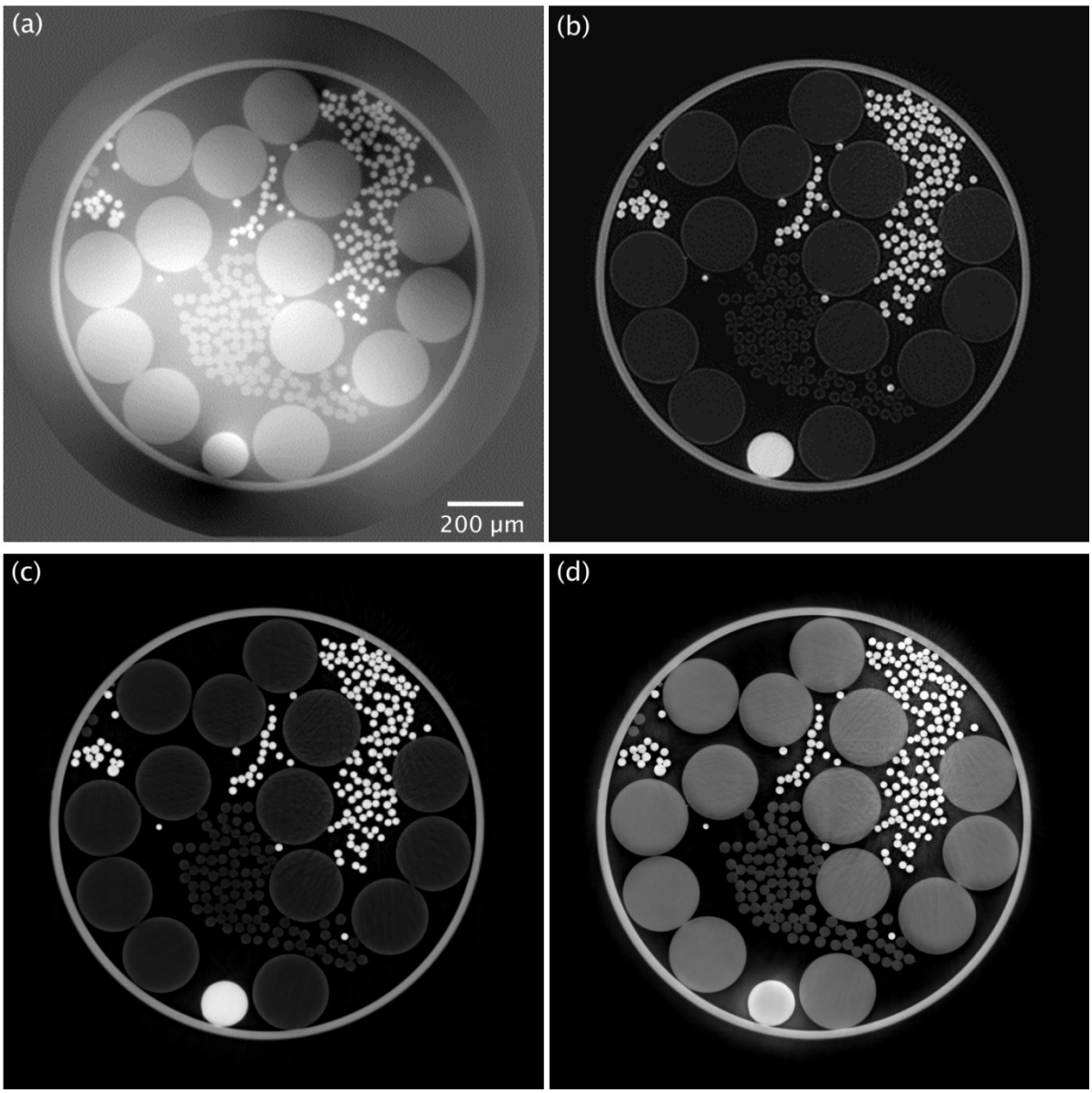

Fig. 2-19 Reconstructed slices of the test object constructed from fibers of Al, Al_2O_3, PP and PET. X-ray energy: 22.5 keV, pixel size: 0.7 µm, propagation distances: d= [2, 10, 20, 45] mm. (a) Using the mixed approach (b) Mixed approach with homogeneity prior (δ/β=367, set to Al), (c) Paganin's method (δ/β=367, set to Al) and (d) the method described above using the attenuation index reconstruction for prior of the phase retrieval. (reprinted from (Langer et al., 2014))

2.3.6 TOMOGRAPHY SETUPS AT END STATIONS ID19 AND ID22 AT THE ESRF

2.3.6.1 ID19 setup

A schematic of the tomography setup at the end station ID19 is shown in Fig. 2-20. The X-ray beam is generated and amplified by the insertion device (either one of the two undulators or a wiggler). The X-ray beam exhibits a high degree of coherence due to the small source size and the long source to sample distance of more than 100 m. The available energy range is between 6 and 100 keV. The X-ray beam can be monochromatized by either a Si crystal monochromator or a multilayer. The sample to detector distance can be varied, allowing phase-retrieval approaches based on the collection of radiographs at multiple distances.

After passing the sample, the X-ray beam is converted into visible light by a fluorescence screen. The visible light is then detected by a charge coupled device based detector (CCD) in combination with a changeable microscopy objective, enabling different effective pixel sizes.

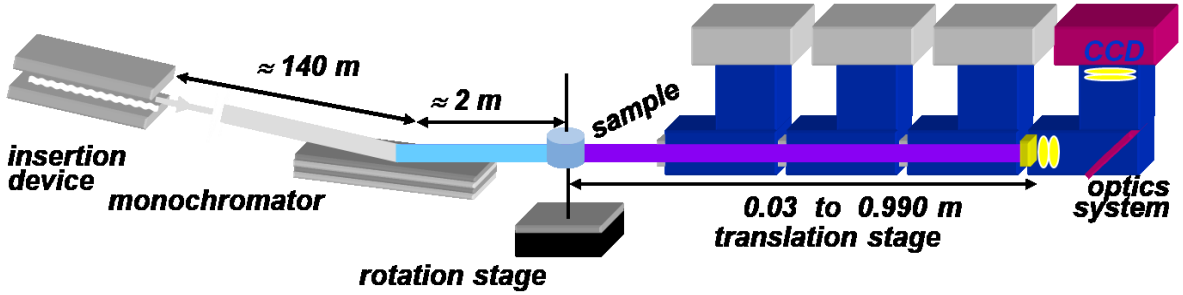

Fig. 2-20 After the X-ray beam is generated by the insertion device, the beam propagates for more than 100 m. Depending on the experimental requirements, the beam might then be monochromatized before it propagates through the sample and is subsequently converted into visible light that is detected by a charge coupled device based detector.

2.3.6.2 ID22NI setup

The experimental setup is situated within a distance of more than 60 m from the insertion device (undulators). The two multilayer optics in KB configuration perform both the focusing and monochromatizing of the X-ray beam. A detailed technical description can be found in (Martinez-Criado *et al.*, 2012). The major difference compared to the ID19 setup is that the beam after the optics is not parallel but cone-shaped, enabling the image to be magnified. The

magnification, M, depends on the position of the sample with respect to the focus position, see Fig. 2-21.

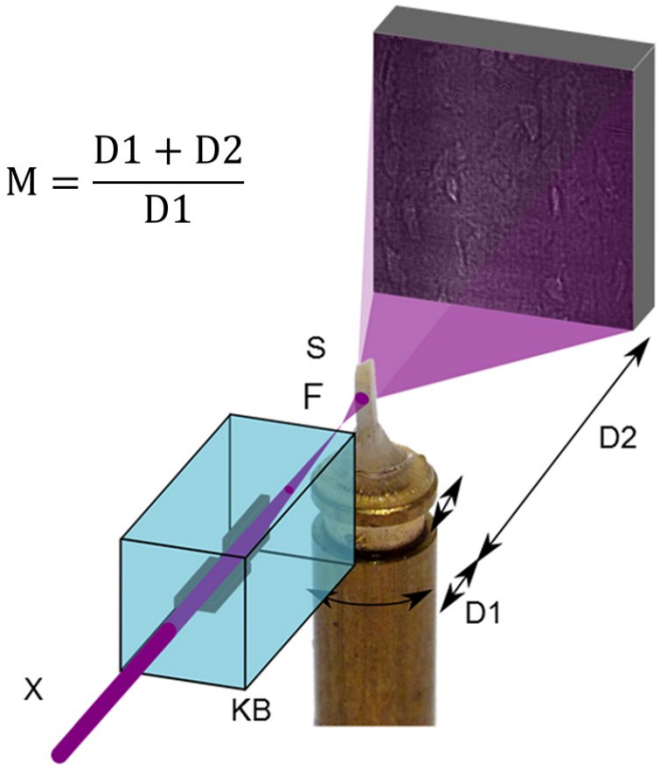

Fig. 2-21 The X-ray beam produced by an undulator is monochromatized and focused by a mirror system in KB configuration. The sample (S) mounted on a rotation stage is positioned between the focus position (F) and a detector system. The closer the sample is positioned to the focus position, the higher the magnification (M). (reprint from (Langer et al., 2012b))

3 EXPERIMENTAL STUDIES

3.1 OSTEOCYTE LACUNAR GEOMETRICAL PROPERTIES IN HUMAN JAW BONE ON THE SUB-MICRON LENGTH SCALE

3.1.1 ABSTRACT

The architectural properties of the osteocyte cell network provide a valuable basis for understanding the mechanisms of bone remodeling, mineral homeostasis, ageing, and pathologies. Recent advances in synchrotron microtomography now enable unprecedented three-dimensional imaging of both the bone lacunar network and the extracellular matrix. Here, we investigated the 3D morphological properties of the osteocyte lacunae in both healthy and bisphosphonate related osteonecrotic (BRONJ) human jaw bone based on synchrotron X-ray computed tomography images, with a spatial isotropic voxel size of 300 nm. BRONJ is a relatively new disease with increasing incidence, which remains poorly understood. A step forward in elucidating this condition is to assess whether, and how, the morphology of the osteocyte lacunar network is modified in the affected jaw tissue. We evaluated thousands of cell lacunae from five specimens, of which three originate from patients diagnosed with bisphosphonate-associated osteonecrosis. We reported the first 3D quantitative results at sub-micron resolution on such specimens. We observed that the differences in lacunar properties are dominated by the donor. While we cannot report any significant impact of BRONJ on the lacunar properties within this study, we observed that the tissue affected with BRONJ tends to have a higher percentage of osteocyte lacunae containing small mineralized spheroidal objects.

3.1.2 METHODS

3.1.2.1 Specimen preparation

Five human jaw bone sections (cubes of about 1 mm^3 in size) were extracted from three female donors suffering from BRONJ (aged 43, 63 and 76, respectively) during the surgical intervention used to treat necrosis. Healthy control samples were obtained from debris from wisdom tooth removal from two female donors aged 25 and 52. All sections originated from similar anatomical regions, i.e. the proximal body of the mandible. All patients signed an informed consent form. Ethical approval was granted by the Ärztekammer Bremen. After

removal, the bone specimens were placed in tissueTec (Sakura Finetec, USA, Inc) and stored frozen at -20 °C until further processing. The specimens were selected from a visually non-necrotic region and cropped while in the frozen stage using a cryotome (CM 3050 S, Leica, Germany) until they reached a size of approximately 0.5 mm in diameter. The cut bone samples were then fixed in 70 % ethanol for transport to the imaging site.

3.1.2.2 SR-µCT

SR-µCT measurements were performed in air at the ID 19 experimental station at the ESRF using the settings established by Pacureanu et al. (Pacureanu *et al.*, 2012). The energy of the X-ray beam was set to 19.1 keV. High flux with a sufficiently narrow energy window could be achieved using a pink beam mode, directly using the first harmonic of the undulator radiation. The X-rays were converted to visible light using a scintillator. A magnifying visible light optics system and a CCD camera were used for detection. An effective pixel size of 300×300 nm^2 was selected. Images were reconstructed with a filtered back projection algorithm.

3.1.2.3 Image analysis

Data processing was performed using custom designed toolboxes and functions written in C++ and Matlab R2009b (The Mathworks Inc., Natick, MA, USA) (available on request). For visualization and manual ROI selection, the software ZIBAmira (Zuse Institut Berlin, Berlin, Germany) (Stalling D, 2005) was used.

Segmentation:

Two binary masks corresponding respectively to the bone and lacunae 3D images were calculated for each sample based on thresholding and 3D image processing methods. The thresholds were adjusted manually for a set of several sub-volumes from different samples so that a good match with a visual segmentation was achieved. Subsequently, the same threshold value was used for all samples. Using a connected components analysis calculated with a connectivity of 16, the largest non-bone volume within the image was identified, including Haversian canals (HC) as well as cavities (lacunae and all other pores, e.g. micro-cracks) connected to the edge of the sample, while excluding internal pores. The inverse of this domain was taken as the first mask, which defined the total volume (TV) of the sample. Bone volume (BV) denotes the total volume minus the lacunae.

In a second step, the lacunae were segmented within the total volume. Morphological operations with a 3D ball-shaped structuring element were used to smooth the lacunar shape and to exclude canaliculi connected to the lacunae. The resulting image was labeled using 3D connected components analysis and was further filtered in order to remove canaliculi or other kinds of small pores such as micro cracks (Fig. 3-1, Fig. 3-5 A). Lacunar volume (Lc.V) was quantified using the voxel count of the individual connected components. Objects with volumes larger than 50 μm^3 but smaller than 1000 μm^3, and with the anisotropy of their shape (defined by the ratios of square roots of eigenvalues of the covariance matrix) being smaller than 10, were defined as lacunae (Fig. 3-5 C, D). In order to investigate lacunar properties exclusively originating from osteonal tissue, one, or if possible two osteons per sample were segmented manually.

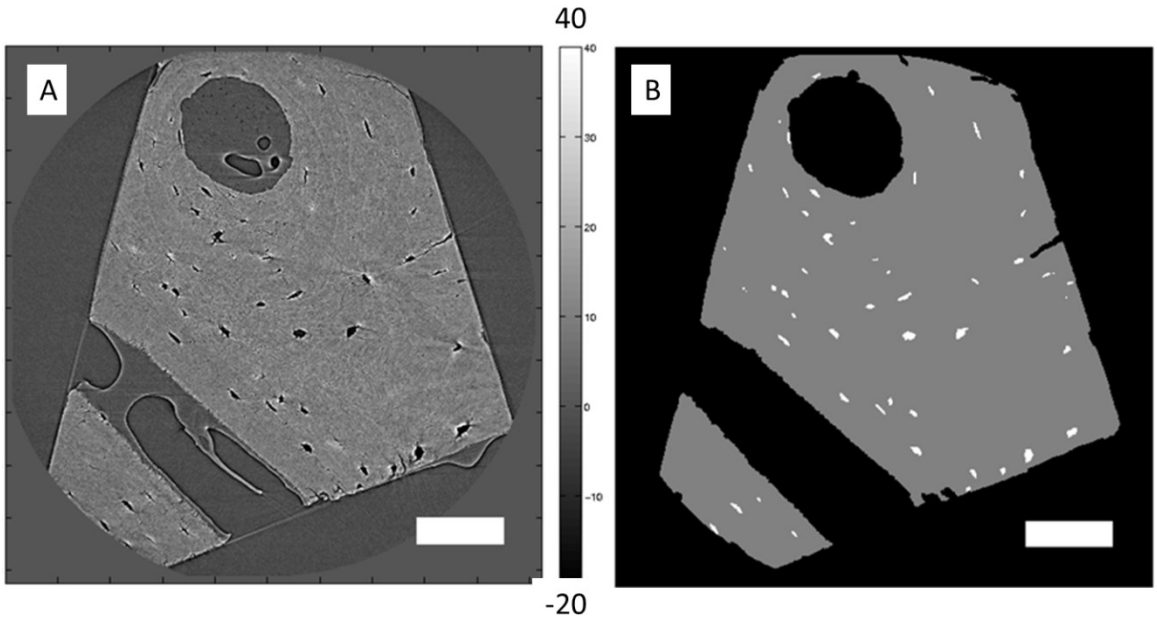

Fig. 3-1: A: Virtual slice through the reconstructed 3D attenuation data, color bar in units of 1/cm, scale bar 100 µm. The irregular features visible inside the HC are most likely due to remaining tissueTec or remnants of the vessel system. B: segmentation of the non-bone area (black), bone area (gray) and lacunae (white).

Detection of pearls inside lacunae:

For each detected lacuna, the binary lacunar mask was eroded, multiplied by the corresponding raw data and binarized to obtain the inner region of each lacuna. The threshold

was selected manually and kept constant throughout the study. A connected component analysis was performed on each lacunar region to check whether it contained a dense object. If the size of a connected component found within the lacunar region exceeded 50 voxels (corresponding to 1.35 μm^3) the object was considered as a pearl and the housing lacunae denoted as Lc_{pearl}. A manual verification on 100 randomly selected pearls from various samples and locations was performed and no erroneous automatic selections were found. Lacunae found to contain a pearl are indicated in Fig. 3-2.

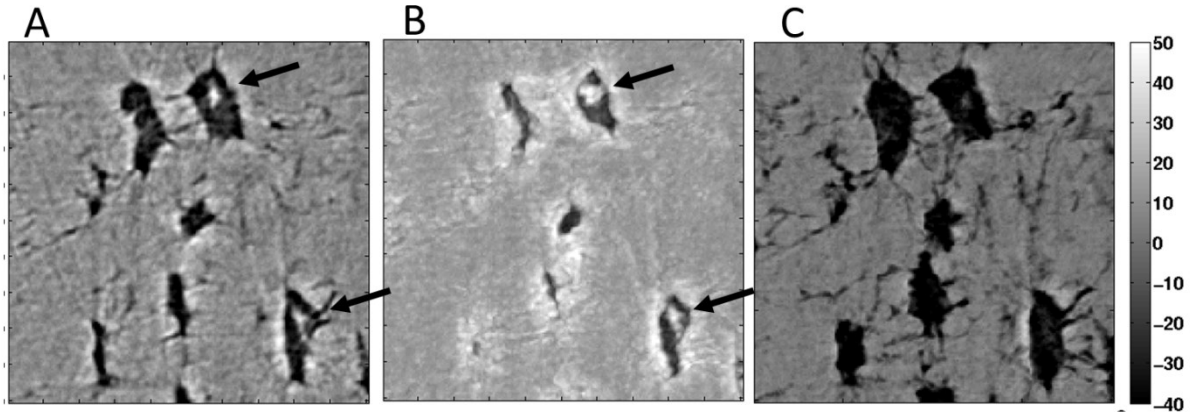

Fig. 3-2 Sub-region from a reconstructed 3D image. A: a single slice is shown. B: maximum intensity projection along z for a z-range of 7 slices. C: minimum intensity projection along z for a z-range of 7 slices. Two lacunae found to contain a pearl are indicated in A and B. The size of each panel is 60 x 60 μm^2. The color bar is the same for all three panels.

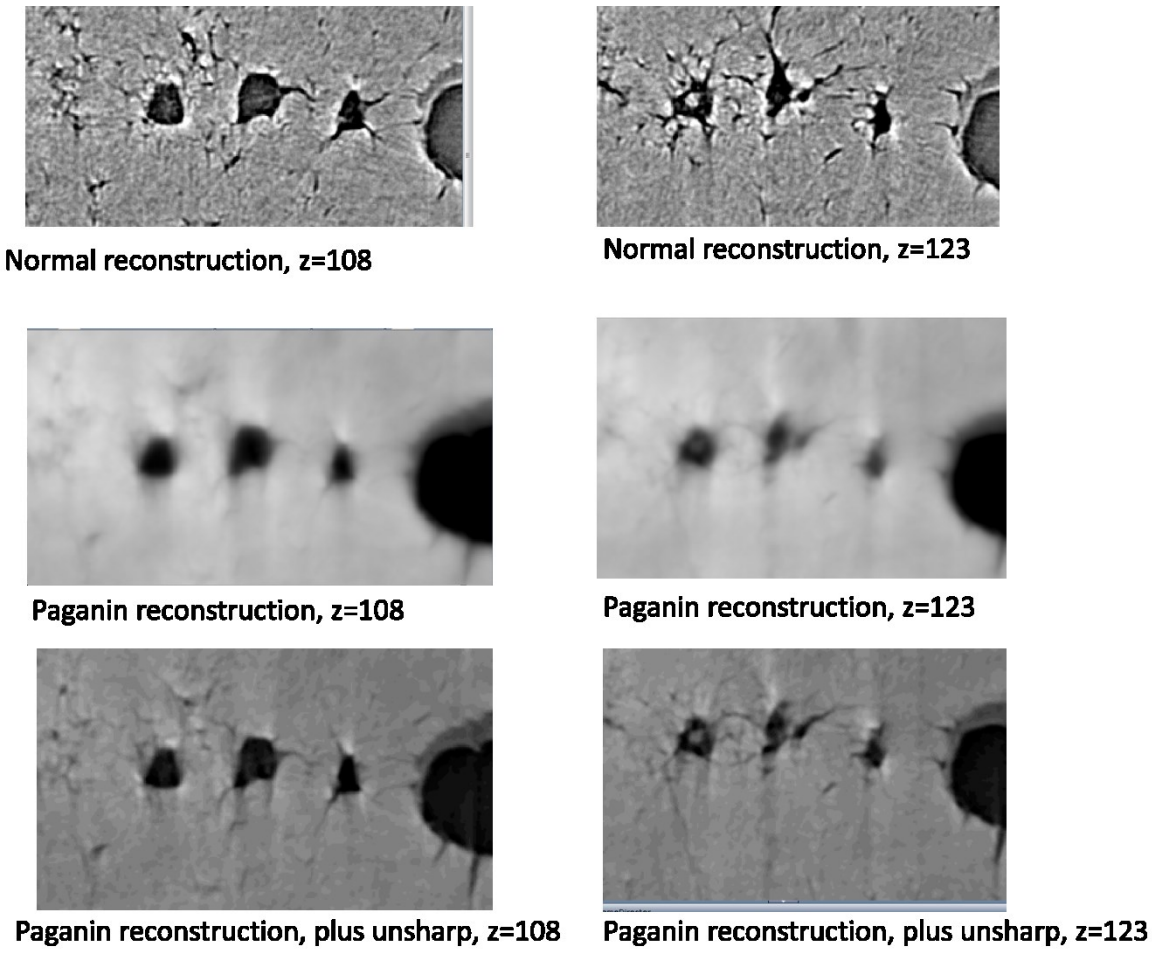

Fig. 3-3 Two slices of one sample reconstructed with the "standard method" used in the manuscript (top panel) and with a simple phase retrieval - Paganin's method, using no filter (middle panel) and an unsharp filter (lower panel). The lacunae shown on the left-hand side do not contain a pearl but remnants of soft tissue are visible (the density of the remnants is much smaller than that which we call pearl. The left lacuna in the right-hand slices does reveal a pearl (red arrow). If this object were a phase artifact of the remnant soft tissue, it would not be visible in the reconstructions based on Paganin's method. However, as Paganin's method blurs the images, small features appear less sharp than those seen when using a conventional attenuation based tomographic reconstruction method.

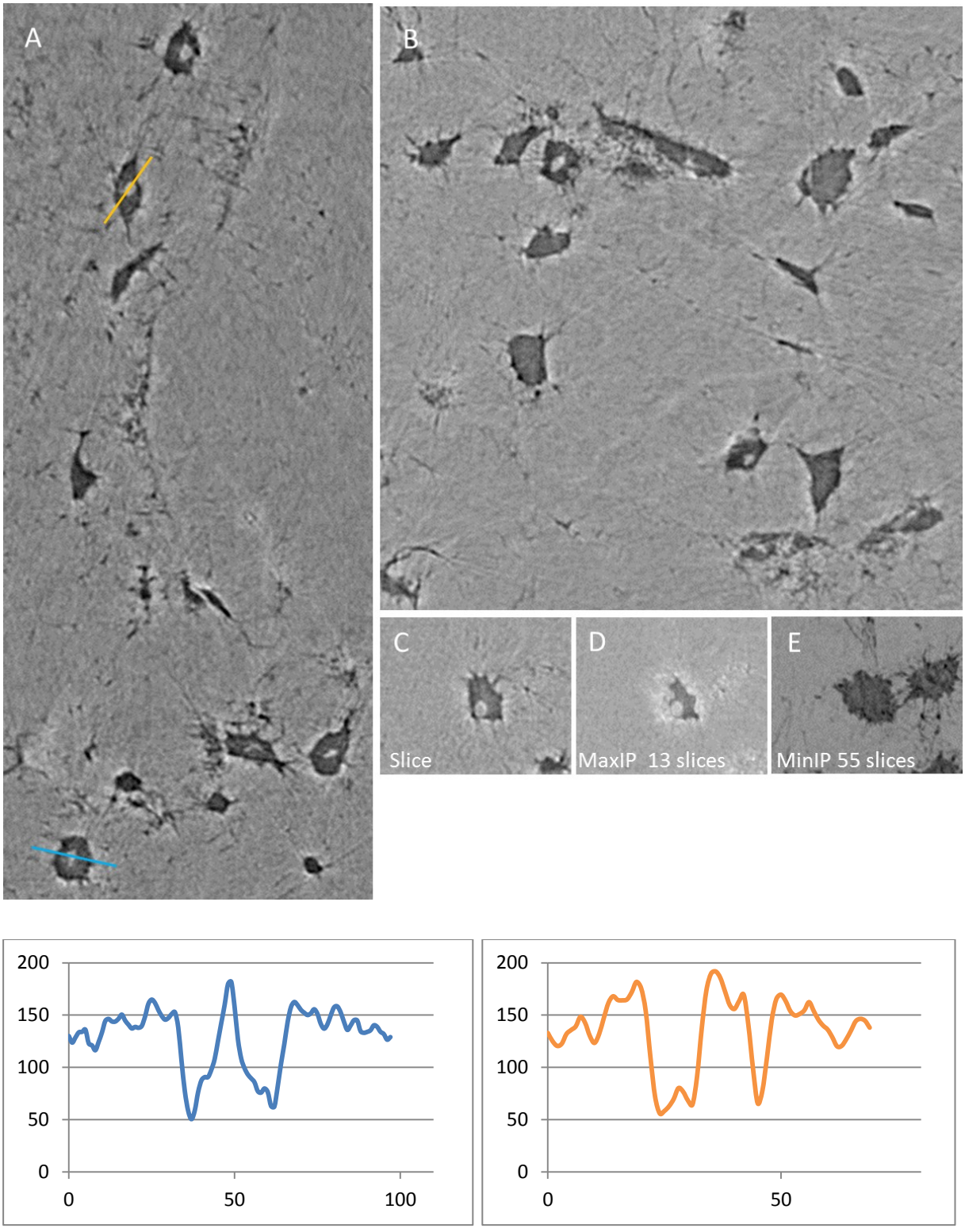

Fig. 3-4 (A) (B) Regions of interest (ROI) from reconstructed slices showing lacunae containing mineralized structures. Note that the lacunae exhibit a lack of organization and lack shape consistency, suggesting a potential malfunction of the local tissue. (C) ROI in a slice showing one lacuna containing a mineralized structure. (D) Max. intensity projection over 13 slices. Although phase contrast effects can be observed, note that the size of the

structure is large enough to not be entirely covered by fringes. (E) Minimum intensity projection over 55 slices. The 2 graphs are profile plots of the lines (blue, orange) on panel (A). These reflect the "edge" effects but also support the thesis that the structures inside the lacunae are indeed calcified.

Shape-based description of lacunae:

The shape of the lacunae was quantified by eigenvalue analysis of the covariance matrix of each binary lacunar mask. Let, $\lambda_1 > \lambda_2 > \lambda_3$ be the square root of the eigenvalues and $(\overrightarrow{u_1}, \overrightarrow{u_2}, \overrightarrow{u_3})$ be the corresponding eigenvectors. Therefore $\overrightarrow{u_1}$ represents the major orientation axis of each lacuna. The ratios of the square root of the eigenvalues were used to describe the anisotropy of the lacuna shape, namely $\frac{\lambda_1}{\lambda_2}, \frac{\lambda_1}{\lambda_3}, \frac{\lambda_2}{\lambda_3}$.

Distance from the bone matrix to the lacunae:

The distance from the extracellular tissue matrix to the osteocyte lacunae was quantified with a Euclidean distance transform. For each voxel characterized as mineralized tissue, the shortest distance to the nearest osteocyte lacuna was calculated (Fig. 3-5 B). The histograms of the distance distribution were normalized to the area under the curves. From the cumulative distribution function, the distances in which 50 % and 95 % of the mineralized matrix are located are denoted as $Lc.Dist_{50}$ and $Lc.Dist_{95}$, respectively. The median of the distance transformation is equal to $Lc.Dist_{50}$.

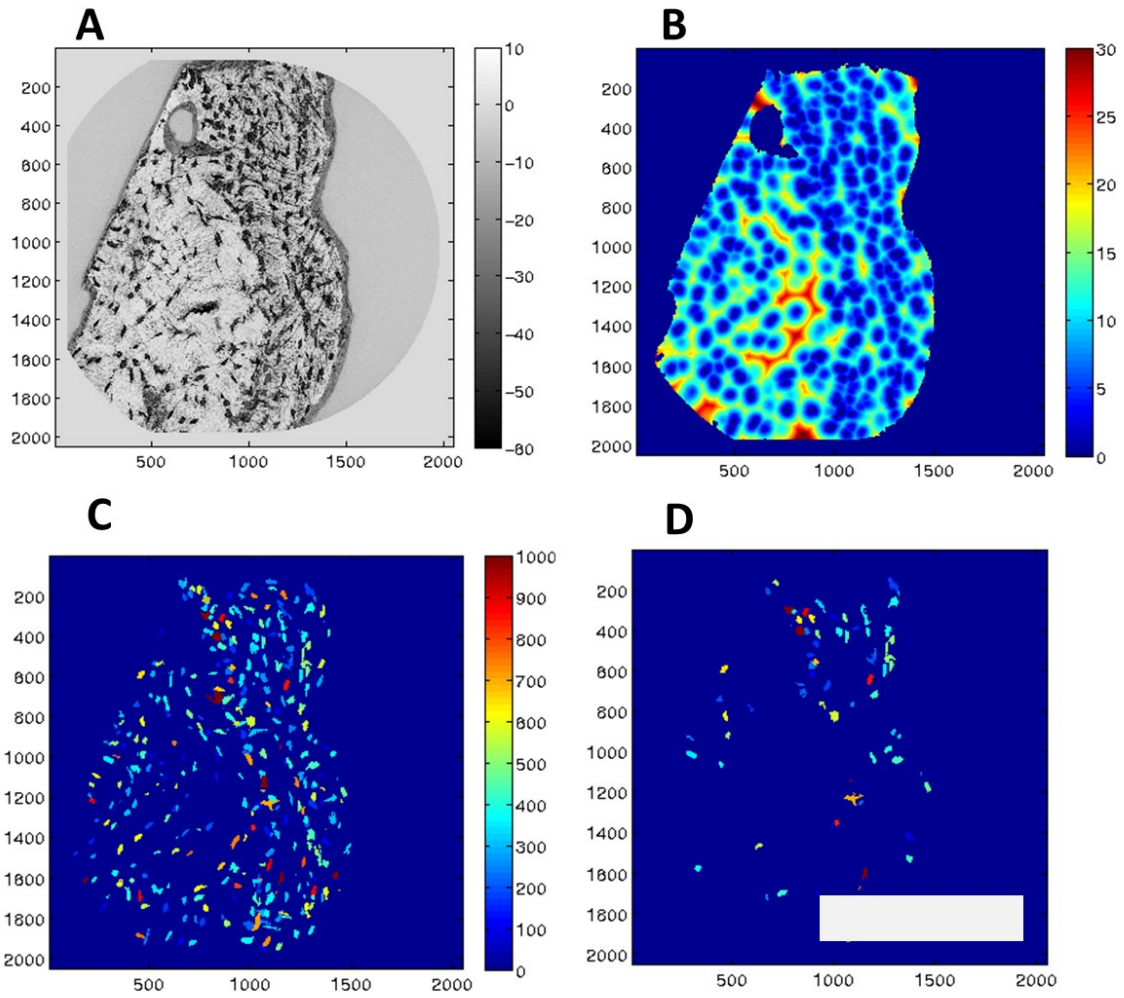

Fig. 3-5 A: Minimum intensity projection of the reconstructed attenuation values across a z-range of 100 slices (30 µm). B shows one slice of a distance map calculated for the 3D image. C: Maximum intensity projection along z for 100 slices of the segmented lacunae, the color code represents the volume of each lacuna in µm^3. D Same as C, but only lacunae containing a pearl are shown. The scale bar represents 300 µm.

3.1.2.4 Statistical analysis:

The normality of the distributions for the investigated parameters was determined using Lilliefors tests. Despite the fact that some parameters were found to be non-normal, the difference between groups was tested with ANOVA and N-way ANOVA. The significance for all tests was considered at the 5% level. Differences between lacunar properties of different donors, quantified by F-statistics, were assessed by ANOVA, followed by post hoc multiple comparison Tukey-Kramer tests. The grouping criteria for the N-way ANOVA were: group 1: BRONJ vs**.** healthy, group 2: respective donor (1, 2, 3, 4, or 5), group 3: pearl vs**.** no

pearl. All tests were performed using the MATLAB Statistics Toolbox (MATLB, RA2012A, The MathWorks Inc., Natick, MA, USA).

3.1.3 RESULTS

For each sample, the lacunar density (N.Lc/BV), the $Lc.Dist_{50}$, the $Lc.Dist_{95}$, the mean and standard deviation of the lacunar size (Lc.V) and the ratio of the square roots of the eigenvalues (EV) are presented in *Table 3-1*. Further significant differences between samples were found when considering the osteonal tissue exclusively, as illustrated in Fig. 3-6. Out of the 19208 lacunae analyzed in total, 1753 were found to contain a pearl. Lacunae containing a pearl were found to be significantly different in size and shape to those that do not contain a pearl. The histograms of the lacunar volumes for all samples are plotted in Fig. 3-7.

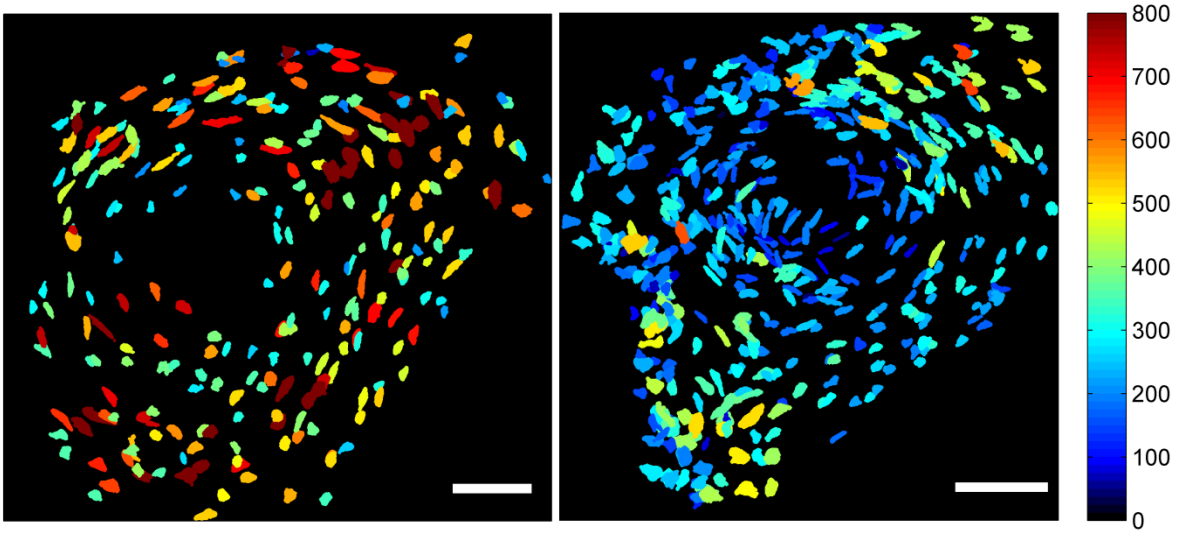

Fig. 3-6 Lacunae from two different osteons of different samples, projected closely along the osteon long axis and color-coded by size volume. Scale bar: 50 µm.

The overall mean volume for all lacunae was found to be 380 ± 190 μm^3. On average, lacunae were found to have a ellipsoidal shape, with the longest axis being on average 4.1 times longer than the shortest axis, while the ratio of the second longest axis was still 1.9 times longer than the shortest axis. The mean ratio of the longest to the second longest axis was found to be 2.3. The histograms of the ratio of the square roots of the eigenvalues are shown in Fig. 3-8.

We found that 50 % and 95 % of the mineralized tissue is located within less than 12 µm and 24 µm distance from the closest lacuna on average, respectively (see Fig. 3-9).

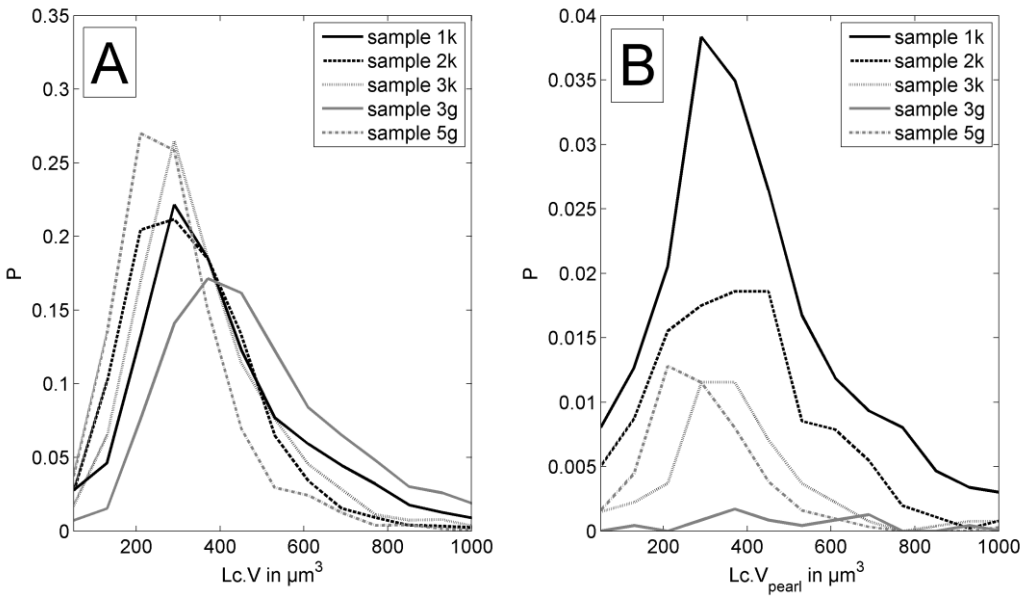

Fig. 3-7 Histograms of lacunar volume for each specimen, considering all lacunae (A) and the lacunae containing a pearl (B). All histograms are normalized to the absolute volume of all lacunae.

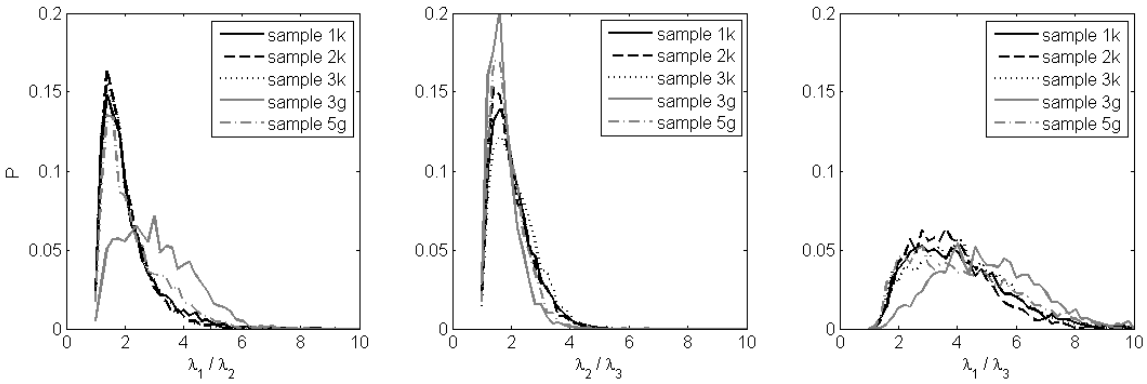

Fig. 3-8 Normalized histograms of the ratios of the different eigenvalues are shown. A: λ_1/λ_2, B: λ_2/λ_3, C: λ_1/λ_3

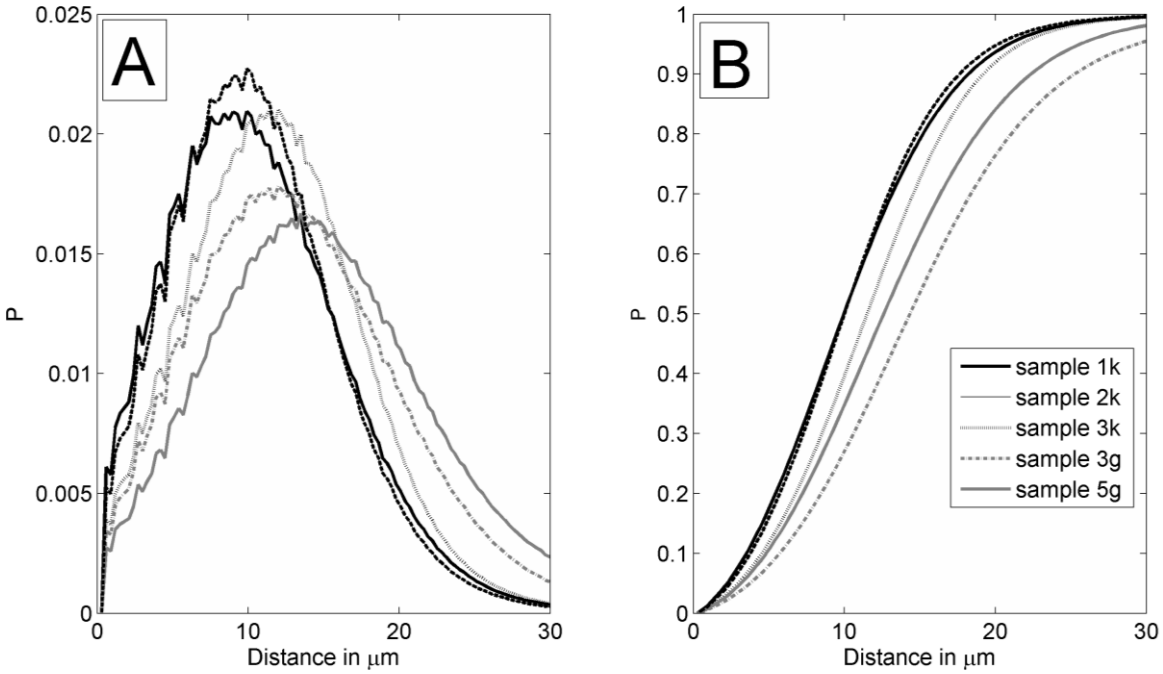

Fig. 3-9 Histograms of the Euclidean distance transform (A) of the 5 investigated samples and their corresponding cumulative functions (B)

Table 3-1 *Summary of investigated properties for each bone sample. N.Lc denotes the number of lacunae, N.Lc/BV the number of lacunae per bone volume, and* $Lc.Dist_{50}$ *and* $Lc.Dist_{95}$ *the distance to the lacunae within which 50 % and 95 % of the bone volume are located, respectively. Lc.V denotes the volume of the lacunae,* λ_i *stands for eigenvalue i of the covariance matrix. The subscript "pearl" refers to lacunae that were found to contain a pearl. The properties are independently reported for lacunae that were located in osteonal tissue (OT) as well as for the whole specimen*

		N.Lc	N.Lc$_{pearl}$	N.Lc/BV in 1/mm^3	Lc.Dist$_{50}$ in µm	Lc.Dist$_{95}$ in µm	Lc.V in µm^3	std	Lc.V$_{pearl}$ in µm^3	std	λ_1/λ_2 all Lc	std	λ_1/λ_2 Lc$_{pearl}$	std	λ_1/λ_3 all Lc	std	λ_1/λ_3 Lc$_{pearl}$	std	λ_2/λ_3 all Lc	std	λ_1/λ_2 Lc$_{pearl}$	std
Sample 1k	all tissue	5682	961	50200	10.2	20.9	429	220	538	233	2.1	0.9	1.9	0.8	3.9	1.6	3.4	1.3	2.0	0.7	1.9	0.6
(BRONJ, 43 y.o.)	OT	655	118	47000	-	-	378	186	471	197	1.8	0.6	1.6	0.4	3.5	1.2	3.0	1.0	2.0	0.6	2.0	0.6
Sample 2k	all tissue	5081	509	46300	10.1	20.3	343	166	427	169	2.0	0.8	2.0	0.7	3.7	1.3	3.4	1.1	1.9	0.6	1.8	0.5
(BRONJ, 76 y.o.)	OT	135	9	29600	-	-	315	136	419	206	2.5	1.0	2.1	0.5	3.9	1.4	3.2	0.6	1.6	0.4	1.6	0.3
Sample 3k	all tissue	2812	124	30800	11.6	21.9	366	175	495	192	2.0	0.8	1.7	0.4	4.0	1.5	4.1	1.1	2.1	0.7	2.5	0.7
(BRONJ, 63 y.o.)	OT	753	43	30200	-	-	337	150	475	197	2.1	0.8	1.7	0.4	4.4	1.4	4.2	1.2	2.2	0.7	2.5	0.8
Sample 3g	all tissue	2368	17	15800	14.6	29.6	502	234	676	278	3.0	1.2	2.1	0.6	5.0	1.7	3.7	1.2	1.7	0.5	1.8	0.5
(healthy, 25 y.o.)	OT	772	3	13300	-	-	492	229	691	139	3.3	1.3	2.7	0.8	5.5	1.7	4.3	1.8	1.7	0.5	1.6	0.3
Sample 5g	all tissue	3265	142	30400	12.8	26.7	296	153	424	219	2.3	1.0	1.9	0.8	4.1	1.7	3.4	1.5	1.9	0.6	1.7	0.5
(healthy, 52 y.o.)	OT	619	27	31300	-	-	267	120	391	163	2.2	0.9	1.8	0.4	4.1	1.5	3.2	1.0	2.0	0.6	1.9	0.5
overall average	all tissue	19208	1753	34700	11.9	23.9	383	189	495	211	2.2	0.9	1.9	0.7	4.0	1.5	3.5	1.2	1.9	0.6	1.9	0.6
	OT	2934	200	30280			371	172	462	192	2.4	0.9	1.7	0.4	4.4	1.5	3.3	1.0	2.0	0.6	2.1	0.6

Table 3-2 Results of the statistical analysis. 3 –factor ANOVA, group 1: BRONJ vs. healthy, group 2: respective donor (1, 2, 3, 4, or 5), group 3: pearl vs. no pearl.

Property	all tissue F-Value Bronj vs control	all tissue F-Value different donor	all tissue F-Value pearl vs no pearl	osteonal F-Value Bronj vs control	osteonal F-Value different donor	osteonal F-Value pearl vs no pearl
Lc.V	-	719	627	-	205	89.7
λ_1/λ_2	-	331.6	46.9	-	198.3	19.7
λ_2/λ_3	-	66	66	-	-	53.1
λ_1/λ_3	-	179.8	160.4	-	134.4	23.7

3.1.4 DISCUSSION

This paper reports for the first time on the geometrical properties of osteocyte lacunae in human jaw bone quantified from 3D images with sub-micron resolution. The size and shape measurements of the lacunae in jaw bone were found here to be in line with those reported for other human bone sites (Carter et al., 2013b, Hannah et al., 2010). However, we did not observe a bimodal distribution of the lacunar volumes, which has previously been discussed by Hannah et al. (Hannah et al., 2010).We found that the average size of lacunae located inside osteonal tissue is smaller than the overall average lacunar size (osteonal and interstitial tissue confounded), suggesting that lacunae become larger with tissue age. However, it should be noted that this comparison is hampered by the fact that for the confounded group, a separation into osteonal and interstitial tissue is not possible. Studies of human femoral bone which investigate the change of lacunar size with respect to donor age have revealed contradictory results, reporting the decrease of lacunar size with age (Carter et al., 2013a), or no impact of age on lacunar size (McCreadie et al., 2004).

We found a variation in the lacunar density, ranging from about 16 000 per mm^3 up to 50 000 per mm^3, which is higher than the range reported for the femoral site (Carter et al., 2013b). However, the lacunae density found in the investigated specimens is in line with values found

for the human femur (Carter et al., 2013b), and also for other mammals, e.g. cortical sheep bone (Metz *et al.*, 2003). The shape achieved, expressed by the ratio of the square root of eigenvalues, is comparable to what is reported for a human femoral site (Carter et al., 2013b), assuming that in this study the eigenvalues were used instead of the square root of them to quantify the anisotropy . However, a precise comparison is limited due to the different resolutions of the imaging techniques. In the present study, we worked with an isotropic voxel size of 0.3 µm which is several times higher than the ones used in other studies investigating the 3D morphology of osteocyte-lacunae (Carter et al., 2013b, Hannah et al., 2010).

We present quantitative 3D data on the location of the bone matrix in terms of distance to the lacunae on this length scale. The distances we found in the human jaw are larger than those reported in a study on ovine fibrolamellar bone, where the authors found that 80% of the matrix is located within 10 µm of the closest lacuna (Kerschnitzki et al., 2013). The measurement of $Lc.Dist_{50}$ and $Lc.Dist_{95}$ might give a superior description of lacunae-to-matrix relationship in comparison to parameters normally reported (such as porosity, density, or distance to neighbors), as it combines lacunae density and spatial lacunae distribution into one parameter. A similar approach was used to describe changes in the vascular-trabecular interdistance in a rat model (Langer et al., 2011), where the authors report mean distances of about 20 to 80 µm.

Finally, we compared lacunar properties that contained dense sub-cellular objects, denoted pearls, with the properties of all other lacunae. First, we observed that the specimens originating from patients suffering from BRONJ contained a higher percentage of lacunae with pearls (~5-15 %) than the healthy specimens (~1-4 %). This suggests that the formation of such highly calcified structures might be fostered by the BP treatment. We also found that lacunae containing pearls were larger than the other lacunae and significantly different in terms of shape. Those differences were observed both when considering the whole sample and in exclusively osteonal tissue. The F-values, however, were smaller compared to those describing differences between the donors. Nevertheless, it should be noted that during the automatic segmentation we only retained pearls not connected to the lacunar wall, and defined minimum sizes for both the pearls and the lacunae. This means that lacunae containing small pearls attached to the lacunar wall and lacunae filled with mineral in a high proportion were not accounted for. Due to these segmentation criteria, the probability to segment a pearl might be higher for larger lacunae. We predict that images acquired at a higher spatial resolution

could reveal an increased incidence of lacunae with such highly mineralized small aggregates. We did not report the size of the mineralized object due to the limited spatial resolution and partial volume effects, which could make a small but very dense object appear larger than it actually is. Additionally, it could be possible that in a few cases, phase artifacts caused by remnants of soft tissue inside the lacunae were falsely identified as pearls. However, we were able to verify that pearls indeed exist and the high-density objects we observed were not artifacts due to imaging or remnants of the cell body, by imaging human cortical specimens at a higher resolution (50 nm) using phase-nanoCT. The imaging setup for this technique has been described elsewhere (Langer et al., 2012b). In the phase-nanoCT, image pearls were found and segmented by simple thresholding (Fig. 3-10). The cell lacuna with canaliculi was segmented using the method from (Pacureanu *et al.*, 2010). It is probably the same kind of dense spherical structures which can be seen in the supplementary videos in Langer et al. (Langer et al., 2012b). Dense mineral-bearing vesicles of sub-micron sizes inside bone forming cells have also been reported in the context of crystallization pathways (Mahamid *et al.*, 2011a). Osteoblasts and osteocytes containing vesicles of approximately 1 μm diameter have been shown to contain several dense globules of approximately 80 nm diameter (Mahamid et al., 2011b).

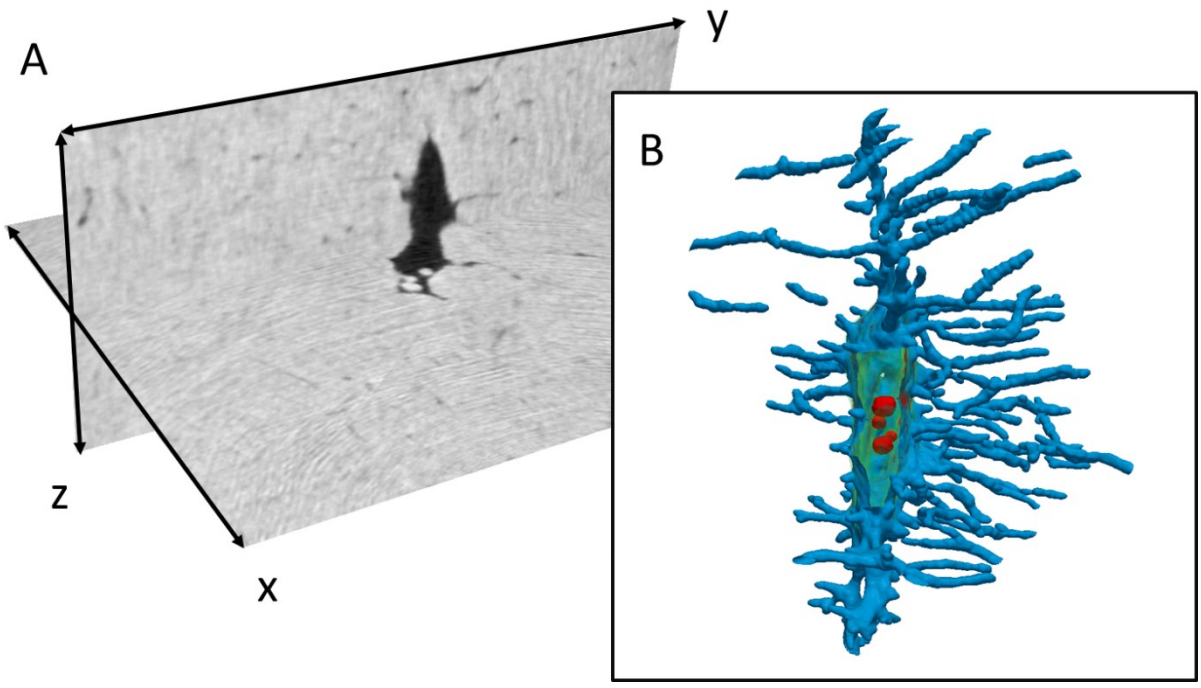

Fig. 3-10 "Pearls" visualized with a higher resolution imaging technique (SR phase nano CT at 50 nm isotropic voxel size). A: Two perpendicular slices of a region of interest from a reconstructed volume. The black color corresponds to zero mass density and white color to high mass density. In the center of the image the osteocyte lacuna is visible, containing several spheroidal, very dense objects. The volume measures 711x900x450 (xyz) voxels with 50 nm pixel size. B: Shows the volume rendering of the lacuna and the canaliculi in panel A, with the pearls found inside the lacuna rendered in red..

Due to the resolution of the setup used in the present study, we cannot resolve those fine structures and it remains unclear to what extent the mineralized objects we report here could be due to the course of cell apoptosis or necrosis, or to what extent they may also be caused by such mineral-containing vesicles.

There are some limitations to this study. The number of analyzed specimens is not sufficient to relate the findings to the course of BRONJ, and the effects of age, site and BRONJ are not separable within the present study. Furthermore, even though each analyzed volume contains several thousand lacunae, this number is relatively small compared to the total number of osteocytes in the jaw bone, and it is not clear how representative it is. In addition, we tested the investigated parameter for normal distribution and found no normal distribution for Lc.V

and for the square root of the eigenvalues. However, we still decided to perform parametric statistical testing, in order to have a multi-factorial test, assuming that the impact of the violation is small compared to the level of significance we reported. Still, it must be noted that all F-values could be overestimated. The quantification of cell lacunae also does not reveal how many of them contained viable osteocytes. A further study would explore the diversity of properties in the human jaw bone in a larger number of specimens and at a higher resolution scale.

Nevertheless, we were able to present osteocyte lacunar properties in 3D on the nanometer scale including several thousands of lacunae from five patients. The 3D data sets and measurements at such high precision are unprecedented in human jaw bone. Moreover, the quantification of lacunae and the mineralized structures found inside some of them in both healthy and BRONJ affected specimens will form the basis for more extended and targeted studies in the future.

3.1.5 CONCLUSION

Based on five jaw bone samples originating from two healthy subjects and three patients suffering from BRONJ, we reported on properties of lacunae (N=19 208) such as average volume (296 - 502 μm^3) and the distribution of the volumes for each specimen, quantified by the standard deviation (153 – 234 μm^3). We observed that the mean and standard deviation of lacunar size are smaller in osteonal tissue compared to the entire sample. The average shape of all lacunae can be described as an ellipsoid characterized by its axes $a>b>c$, where $a=2.2b$ and $a=4c$. The lacunar density varied between 15800 and 50200 per mm^3. Additionally, we quantified the spatial distribution of the lacunae by using a measure of the distance between the lacunae and the mineralized matrix, and found that on average 50% of the mineralized matrix volume is located within 11.9 µm of the closest lacunar boundary. Furthermore, we described the frequency of lacunae containing mineralized objects and found this to be higher in BRONJ samples. In this pilot study we have not related our findings to the course or cause of BRONJ due to the small number of specimens. However, we found that the differences in morphological properties are statistically significant between all five investigated specimens.

3.2 ALTERATIONS OF MASS DENSITY AND 3D OSTEOCYTE LACUNAR PROPERTIES IN BISPHOSPHONATE-RELATED OSTEONECROTIC HUMAN JAW BONE

3.2.1 ABSTRACT

Osteonecrosis of the jaw in association with bisphosphonates (BRONJ), used for treating osteoporosis or cancer, is a severe and most often irreversible side effect whose underlying pathophysiological mechanisms remain largely unknown. Osteocytes are involved in bone remodeling and mineralization where they orchestrate the delicate equilibrium between osteoclast and osteoblast activity and through the active process called osteocytic osteolysis. Here, we hypothesized that (i) changes of the mineralized tissue matrix play a substantial role in the pathogenesis of BRONJ, (ii) the osteocyte lacunar morphology is altered in BRONJ. Synchrotron μCT with phase contrast is an appropriate tool for assessing both the 3D morphology of the osteocyte lacunae and the bone matrix mass density. In the present study, we used this technique to investigate the mass density distribution and 3D osteocyte lacunar properties at sub-micrometer scale in human bone samples from the jaw, femur and tibia. First, we compared healthy human jaw bone to human tibia and femur in order to assess the specific differences and address potential explanations of why the jaw bone is exclusively targeted by the necrosis as a side effect of BP treatment. Second, we investigated the differences between BRONJ and control jaw bone samples to detect potential differences to aid an improved understanding of the course of BRONJ. We found that the apparent mass density of jaw bone is significantly smaller compared to that of tibia, consistent with a higher bone turnover in jaw bone. The variance of the lacunar volume distribution was significantly different depending on the anatomical site. The comparison between BRONJ and control jaw specimens revealed no significant increase in mineralization after BP. We found a significant decrease of osteocyte-lacunar density in the BRONJ group compared to the control jaw. Interestingly, the osteocyte lacunar volume distribution was not altered after BP treatment.

3.2.2 MATERIAL AND METHODS

3.2.2.1 Specimen preparation

Nineteen human mandibular jaw bone sections (blocks of about 1-3mm^3 in size) were extracted from 12 female and 7 male donors (aged between 19 and 84 years) of which 8 female and 2 male donors were suffering from BRONJ. The healthy control samples were obtained from debris during wisdom tooth removal. The BRONJ samples were obtained from surgeries necessary for the treatment of the necrosis. All jaw sections originated from similar anatomical regions of the mandible. Patients included in this study suffering from BRONJ have previously received high-dosage BP (>11 months).

Furthermore, 7 cadaver specimens originating from the human femoral midshaft (age and gender: 60^m, 66^f, 68^f, 70^f, 71^m, 87^f years) and 3 cadaver specimens originating from the human tibia midshaft (age: 29^m, 56^m, 88^m year old) were included in the present study (the superscripts m and f refer to male and female, respectively), see Table 1. The femora were collected and prepared as described previously (Dall'Ara *et al.*, 2013). After removal, the jaw bone sections were embedded in Tissue-Tek® O.C.T.^{TM} (Sakura Fintec Europe B.V., Alphen aan den Rijn, Netherlands) solution and stored frozen at -20 °C until further processing. Following thawing, the specimens were drilled down to a diameter of about 0.5 mm using a high precision lathe (Lakshmanan *et al.*, 2007). For the BRONJ samples, this sub-volume was selected from a region in which no necrotic tissue was observed. The cut bone samples were fixed in 70 % ethanol for transport. Tibia bone cores were machined with a coring tool and precision circular saw to a length of 4mm and diameter of 4mm, similar to the sample preparation described in (Kazakia *et al.*, 2008). Then, to fit the field of view, the tibia samples were cut from cortical bone (diameter: 500 µm, height: 1 mm) using a high precision drilling machine. About 12 hours before imaging, the samples were placed inside the measurement hutch in order to allow adjustment to humidity and temperature.

3.2.2.2 Synchrotron Radiation phase contrast µCT

The SR µCT data were obtained at ESRF (European Synchrotron Radiation Facility, Grenoble, France) at beamline ID22NI. The X-ray beam was focused using Kirkpatrick-Baez reflective optics (Langer et al., 2012b). The scans used in the present study were performed for each sample by collecting 1201 projections, each with 0.2 s exposure time, over a total range of 360°. The energy was set to 16.874 keV, and the sample-detector distance was 282

mm, resulting in a $(350\ nm)^3$ isotropic voxel size in the reconstructed image. Due to the coherence of the synchrotron source, the intensity of the recorded radiograph includes phase contrast (Marinescu *et al.*, 2013, Cloetens *et al.*, 1997). Reconstruction was performed using Paganin's method (Paganin et al., 2002), coupled to the conventional filtered back projection algorithm.

In the Paganin method the phase is retrieved by simply assuming a linear relationship between the absorption index (β) and the refractive index decrement (δ). For cortical bone (ICRU-44), the δ/β (delta/beta) ratio at the given energy was set to 199 based on the XOP software (del Río & Dejus, 2004). The high ratio of delta/beta demonstrates the higher sensitivity of imaging the phase (δ) compared to imaging the attenuation (β). The reconstructed 3D image made of 2048^3 voxels corresponds to a map of the refractive indices stored in units of $2\pi/\lambda$, with λ being the wavelength of the X-ray beam (here λ=0.0735 nm). This map is linearly related to mass density (Langer et al., 2012b) which was shown to be associated with the degree of mineralization (Raum *et al.*, 2006). The spatial resolution with these settings allowed an easy distinction of osteocyte lacunae and larger pores from the mineralized tissue matrix (Fig. 3-11). However, the canalicular network could be not resolved.

3.2.2.3 Image segmentation

In order to segment osteocyte lacunae inside the bone tissue volume (BV), the histogram of the whole 3D image was computed (Fig. 3-13 A). A threshold was determined for each image using the multi-class Otsu's method in the open-source software ITK (Kitware) (Yoo *et al.*, 2002) to separate mineralized tissue from non-mineralized pores. The resulting binary image was then labeled using a 3D connected component (CC) analysis method (Dong et al., 2013a). Objects smaller than 50 μm^3 or larger than 1000 μm^3 were considered not to be lacunae and were excluded from further analysis.

3.2.2.4 Extraction of quantitative parameters

The 3D image of each sample was virtually divided along the sample length into 3 equally sized volumes of interest (VOI). The lacunae connected to the border, which could be truncated, were removed to avoid including bias in the analysis. Bone volume (BV) was considered as the entire mineralized tissue excluding osteocyte lacunae and other pores. The lacunae were segmented as described above and their volumes were computed for each VOI. The median ($Lc.V_{med}$) and the variance ($Lc.V_{var}$) were extracted from the histogram of the

lacunar volumes. Lacunar porosity was derived as the ratio of the summed volume of all lacunae to the bone volume (Lc.TV/BV) and the lacunae density was defined as the number of lacunae per bone volume (N.Lc/BV). Furthermore, for each VOI, the distance within which 50 % of the mineralized bone tissue is located with respect to the closest lacunar surface ($Lc.Dist_{50}$) was computed as the median of the Euclidean distance transform of the bone tissue (Dong et al., 2013b).

Additionally, we used the reconstructed complex refractive index distribution, which is linearly related to the mass density, to compute the apparent mass density distribution (MDD^r) of each sample (Fig. 3-13 B). The MDD^r was calculated within the BV domain and was normalized by its area under the curve. Since the reconstructed complex refractive index might be biased due to a constant delta over beta ratio used in the Paganin phase retrieval (Weitkamp et al., 2011), absolute values of mass density could not be retrieved and hereinafter the superscript *r* denotes relative values for all mass density parameters. However, since the different bone samples can be considered comparable in terms of size and composition, this allows quantitative comparison of the relative difference in mass density between the bone samples.

Following the well-established approach for the description of BMDD by Roschger et al. (Roschger et al., 2008), five parameters were extracted from the MDD^r, i.e. MDD^r_{Mean} (the mean relative mass density within the evaluated distribution), MDD^r_{Peak} (the most frequent relative mass density value), MDD^r_{Low} and MDD^r_{High} (the 0.5^{th} and 99.5^{th} percentiles), and MDD^r_{FWHM} (the full width at half maxima of the distribution). The threshold of P=0.005 was arbitrarily chosen and is a compromise between maintaining good sensitivity for low and high values in the MDD^r and minimizing potential artifacts using the partial volume effect for MDD^r_{Low}.

Eventually, the vascular porosity was estimated after coarsening the segmented volumes by a factor of five and cleaning the volumes from objects smaller than 1600 voxel (8575 μm^3). The canal volume (Ca.V) was quantified using voxel counting and canal surface (Ca.S) was determined from the number of voxel located within one voxel Euclidean distance to the pore boundary. The following parameters were quantified: canal volume to bone volume ratio (Ca.V/BV), canal surface to bone volume ratio (Ca.S/BV) and canal surface to canal volume ratio (Ca.S/Ca.V).

All post-processing was done using MATLAB 2012a (The MathWorks Inc., Natick, MA, USA).

3.2.2.5 Statistical analysis

All statistical analyses were performed using the statistics toolbox of MATLAB. The normality of the distributions of each investigated parameter was determined by the Jarque-Bera test (Jarque, 1987). Differences with respect to anatomical sites, healthy and BRONJ groups were assessed by analyses of variance (ANOVA), followed by post hoc multiple comparison Bonferroni tests. The sample size did not allow a robust analysis of age and gender effects. All statistical results were considered significant for $p < 0.05$.

3.2.3 RESULTS

Cross sectional μCT images and the corresponding segmented lacunar areas of a jaw bone sample are shown in Fig. 3-11. A 3D volume rendering of the osteocyte lacunae with subsections of one jaw and a femur sample image are shown in Fig. 3-12. These representative images exhibit distinct differences in the distribution and alignment of the lacunae in the different anatomical sites. The relative mass density histogram of the jaw specimen shown in Fig. 3-11 is shown in Fig. 3-13. The normalized histograms of the three adjacent sub-volumes of the same specimen in Fig. 3-14 illustrate the local intra-sample variability of MDD^r.

The average properties for the three different anatomical sites and the BRONJ samples are summarized in Table 3-3.

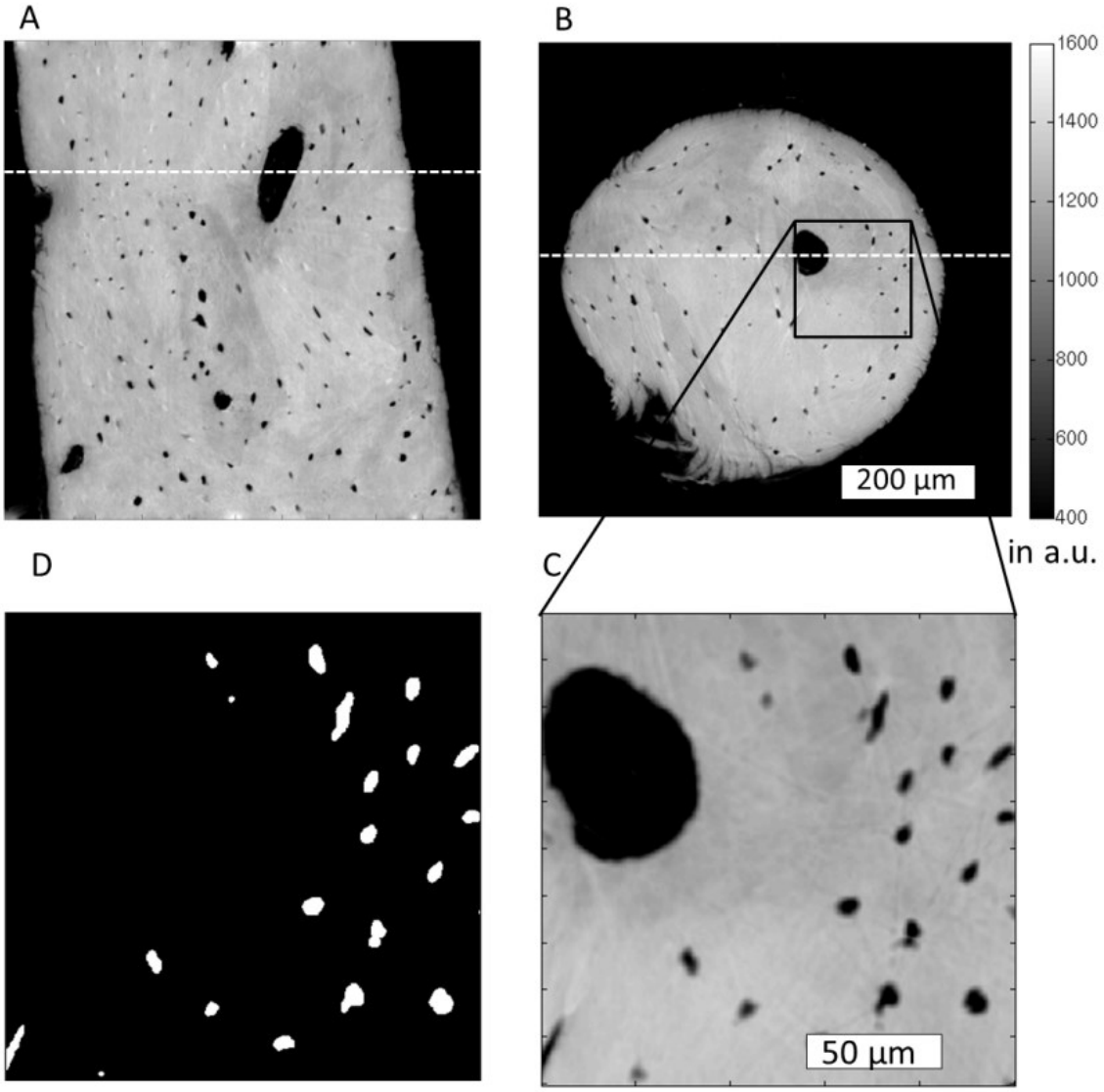

Fig. 3-11 Slides of a reconstructed volume corresponding to a control jaw specimen are shown in A (x-y-plane) and B (x-z-plane). The white dashed lines in A and B indicate where A is located in B and vice versa. C shows a minimum intensity projection, the projection range is 30 pixels (10.5 µm). D shows the lacunae mask corresponding to C, also in the form of an intensity projection (z-range = 30 pixels). Color bar in mass density of a.u.

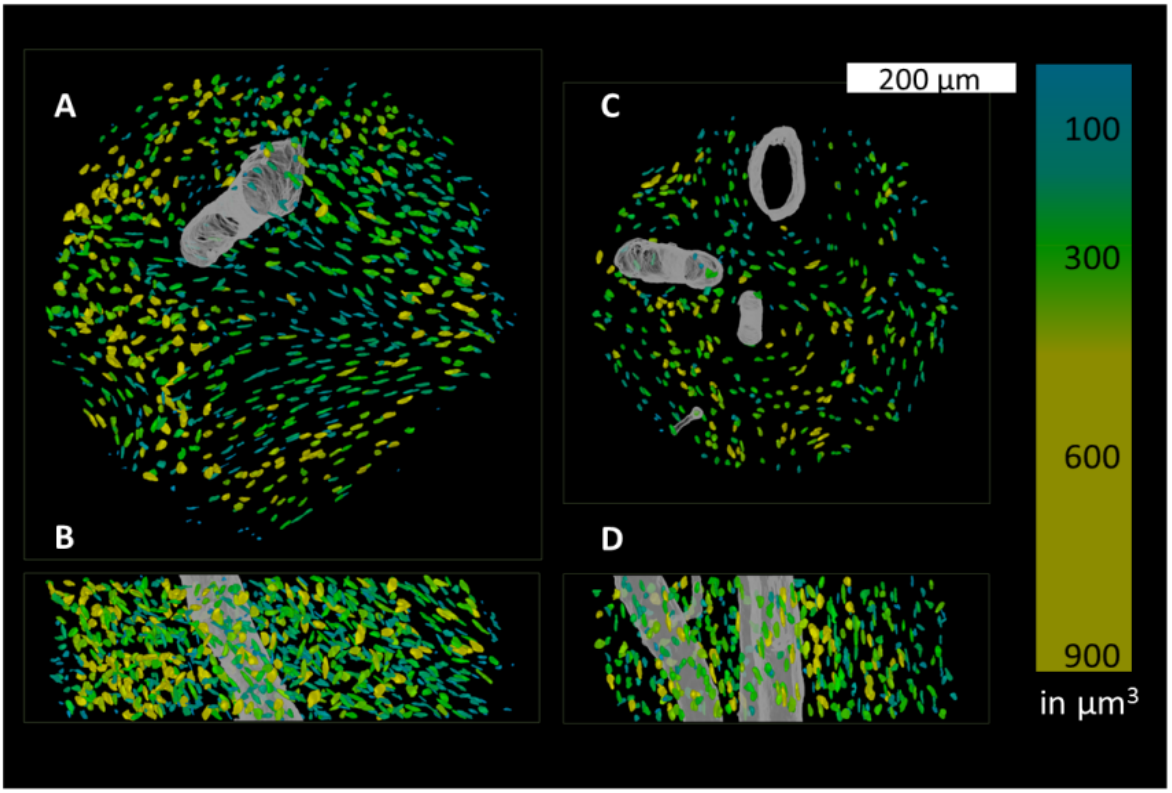

Fig. 3-12 Volume renderings of two subsections originating from the jaw (A, B) and the femur (C, D. A and C show the lacunae and canals from a "top-down" perspective while B and D are shown from a "front-on" perspective. The volumes of the lacunae are color-coded in units of μm^3.

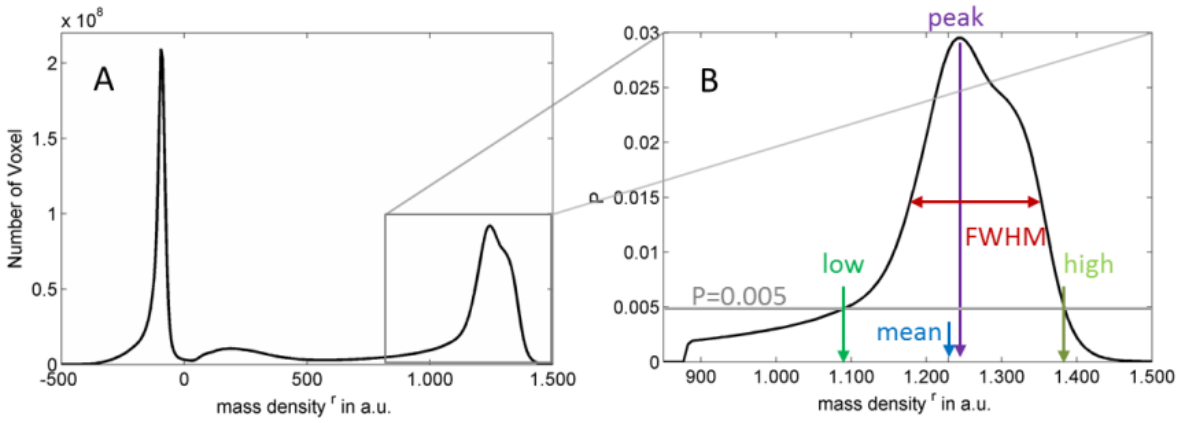

Fig. 3-13 In (A) a relative mass density distribution is shown. The peak at around -100 is due to the air outside the sample, and the broad peak at about 200 is due to the glue used to attach the sample that managed to travel up the sample. In (B) the MDD^r after segmentation is shown, the parameters derived from it are indicated.

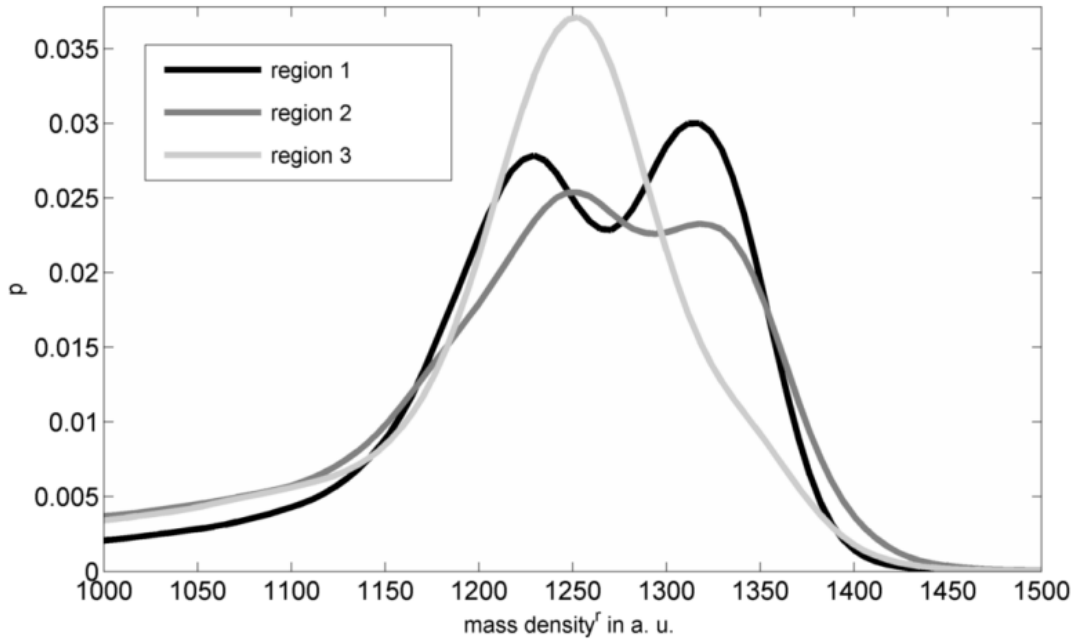

Fig. 3-14 The MDD^r are shown for the three regions, with region 1, region 2, and region 3 being the top, the middle and the lower sub-section of one specimen scanned, respectively.

Table 3-3 Mean and standard deviation for the different properties for the sites averaged over the ROI investigated. The * indicates that those properties are statistically significantly different between the BRONJ and control jaws.

	Tibia	Femur	Jaw (control)	Jaw (BRONJ)
Age of donor	58 (24)	69 (10)	43 (15)	67 (14)
Number of ROI	9	21	26	30
Number of different donors	3	7	9	10
N.Lc	12530	11867	18665	15349
$Lc.V_{med}$ in μm^3	194 (27)	224 (42)	277 (117)	269 (80)
$Lc.V_{var}$ in 1000 μm^6	6.4 (1.9)	11.0 (3.6)	22.0 (11.5)	26.6 (8.9)
$Lc.Dist_{50}$ in µm	11.1 (0.4)	15.2 (0.8)	12.9 (1.5)	13.9 (1.1)*
Lc.TV/BV in %	0.76 (0.09)	0.45 (0.09)	0.79 (0.32)	0.69 (0.17)
N.Lc/BV in 1000 mm^{-3}	38 (5)	20 (2)	27 (6)	23 (4)*
MDD^r_{Mean} in a.u.	1301 (17)	1219 (29)	1208 (66)	1225 (52)
MDD^r_{Peak} in a.u.	1322 (24)	1254 (68)	1277 (52)	1270 (48)
MDD^r_{FWHM} in a.u.	104 (38)	149 (72)	170 (66)	142 (38)
MDD^r_{Low} in a.u.	1194 (21)	1080 (33)	1048 (90)	1073 (73)
MDD^r_{High} in a.u.	1408 (24)	1373 (33)	1360 (42)	1370 (45)

3.2.3.1 *Differences between anatomical sites*

The average lacunar volume ranged from 194 μm^3 in the tibia samples to 277 μm^3 in the jaw bone. Both median values and variance (Fig. 3-15 A-B) were higher in the jaw bones compared to the other anatomical sites. Distinct distributions of lacunar volume between samples from the jaw bone and those obtained from the peripheral skeletal sites are also illustrated in Fig. 3-16, which shows comparable, almost normal distributions for tibia and femur samples, but a remarkable asymmetry towards high volumes in the jaw bone samples. The average distance, in which 50 % of the tissue matrix located with respect to the closest lacunae is located ($Lc.Dist_{50}$), was highest in the femur, followed by the jaw bones, and lowest in the tibiae (Fig. 3-15 E). However, the standard deviation in jaw bone was considerably higher than in the other skeletal sites. For all investigated sites, an average

lacunar density (N.Lc/BV) larger than or equal to 20.000 mm^{-3} was found (Fig. 3-15 D). Variations between the anatomical sites reflected those observed for $Lc.Dist_{50}$, i.e. the lacunar density was highest in the tibia and lowest in the femur. The lacunar density in the jaw bones was in between those of the other two sites.

Mean, low, and high values of the relative mass density distribution were significantly higher in the tibia compared to jaw and femur (Figs. 3-15 G-H). In contrast, the heterogeneity of MDD^r within the evaluated sub-volumes, as expressed by MDD^r_{FWHM} was higher in the jaw bone than in tibia samples.

The average and standard deviation of Ca.V/BV, Ca.S/BV and Ca.S/Ca.V of all sections were found to be (7 ± 5) %, (0.004 ± 0.003) μm^{-1}, and (0.06 ± 0.03) μm^{-1}, respectively. All values are summarized in Table *3-4*. ANOVA revealed no significant differences between the different anatomical sites or between jaw sections from healthy donors and BRONJ.

Table 3-4 Mean and standard deviation of investigated morphometric properties of the segmented vessel pores for the different anatomical sites and pathology. Ca.V: canal volume, BV: bone volume, Ca.S: canal surface.

	Tibia	Femur	Jaw (control)	Jaw (BRONJ)
Ca.V/BV in %	5 (4)	8 (6)	7 (7)	7 (4)
Ca.S/Ca.V in μm^{-1}	0.06 (0.04)	0.06 (0.03)	0.07 (0.04)	0.06 (0.02)
Ca.S/BV in μm^{-1}	0.002 (0.001)	0.003 (0.001)	0.005 (0.004)	0.004 (0.002)

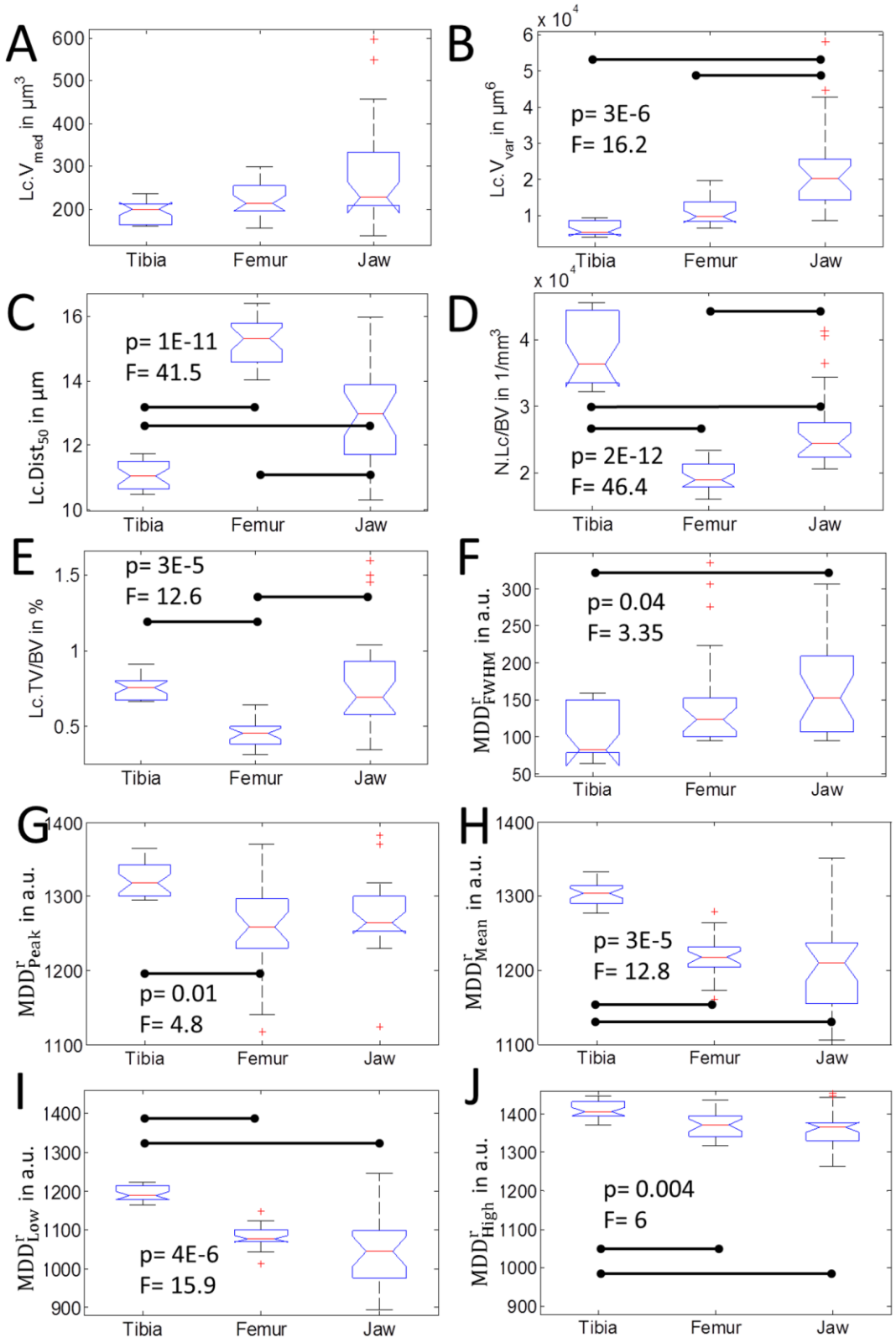

Fig. 3-15 Summarized results from ANOVA on lacunar properties and MDD^r for different human sites are shown. Significant differences between groups are indicated by a horizontal bar. If the significance level was reached, the F-Value and p-Value are reported.

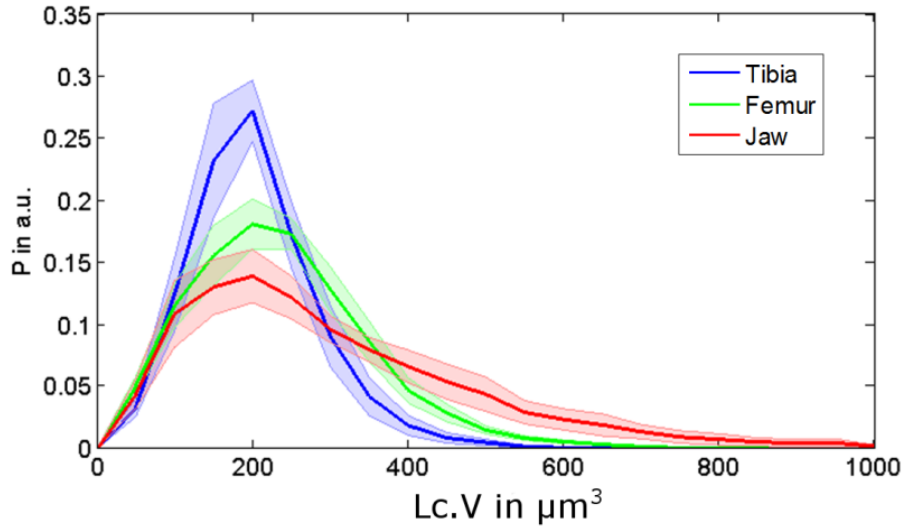

Fig. 3-16 Histograms of the lacunar volumes for the three different sites are shown. Histograms are normalized to the area under the total number of lacunae for each site. Bin-size is set to 50 µm^3. The transparent areas indicate the standard error for each site based on the individual samples.

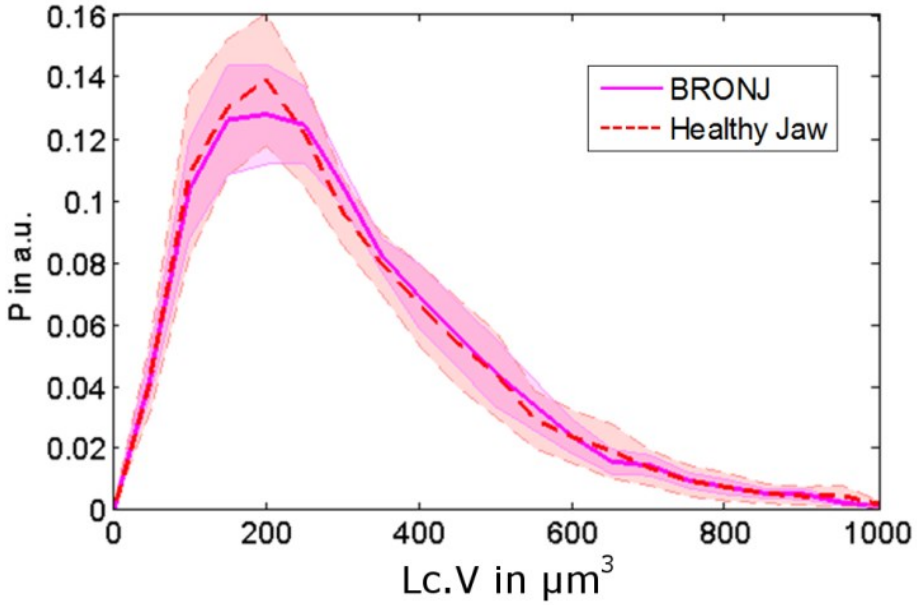

Fig. 3-17 Histograms of all jaw lacunae grouped in either BRONJ or healthy bone. The shaded areas correspond to the standard error based on the different samples. Histograms are normalized to the absolute amount of lacunae, bin-size is 50 µm^3. It must be noted that even though the histograms of the two groups look very similar, there are differences between the histograms of individual donors.

3.2.3.2 *Differences between BRONJ and control jaw bones*

In the BRONJ sample group, significantly lower lacunar densities ($F = 5.1$, $p < 0.028$) were observed (Table 3-3). The lower lacunar density was associated with higher $Lc.Dist_{50}$ values ($F = 6.7$, $p < 0.012$). It should be noted that the values observed in the BRONJ samples are still within the range observed at the other skeletal sites (see Table 3-3). All other evaluated parameters were not statistically significantly altered between BRONJ samples and healthy jaw bone controls. Most strikingly, the lacunar volume distributions of BRONJ and control jaw bone samples were almost identical (Fig. 3-17).

3.2.3.3 Estimating the absolute number of osteocyte lacunae for human subject

The values we obtained for the spatial lacunar density range from 20 000 (femora) to 38 000 per mm^3 (tibia) with jaw in between at about 25 000 per mm^3. Even if an overall average of at least 20 000 lacunae per mm^3 (equals to 20 billion lacunae/liter) is assumed, the impressive number of about 50 billion osteocytes can be found for adults within the whole human skeleton, having estimated the overall cortical and trabecular bone volume to be about 2 liters (relative human dry bone mass is 6-7 % (Heymsfield *et al.*, 2005), which gives about 5 kg of bone for a 75 kg person, density is approximated to be 2 g/cm^3 leading to about 2.5 liters of absolute mineralized bone volume). For comparison, the number of neurons found in the human brain is 86 billion (Azevedo *et al.*, 2009). However, in this estimation we assumed that all lacunae actually contain an osteocyte and are not empty.

3.2.4 DISCUSSION

The present study aimed to determine the potential impacts of alterations of the osteocyte lacunar network, and mass density of the extracellular matrix, in the event of osteonecrosis after BP treatment. To address this question, we used synchrotron radiation phase micro-tomography with a 350 nm voxel size. We analyzed human cortical bone specimens extracted from the mandibular jaw of 10 patients suffering from BRONJ and of 9 healthy persons for control. In addition, we investigated samples from anatomical sites in which the BP treatment does not usually induce necrosis, such as the tibia and femur.

The imaging technique used allows the investigation of relatively large sample volumes in 3D, without the necessity for demineralization or any other tissue preparation steps (except for ethanol fixation and drying), and combines a large field of view, a very high spatial

resolution and a high signal-to-noise ratio with a good sensitivity to mass density fluctuations (Marinescu et al., 2013, Diemoz *et al.*, 2012). Although the absolute mass density could not be derived, the derived relative mass density distributions (MDD^r) enabled a quantitative comparison between the evaluated samples.

Our results suggest that the osteocyte lacunar number, volume and distribution, as well as the mass density in the extracellular matrix, are closely linked to the anatomical site. While there are several studies reporting the human lacunar density based on 2D imaging modalities (Qiu *et al.*, 2006, Mullender et al., 2005) there are only a few reporting lacunar density in 3D, and these are from attenuation contrast tomography (Dong et al., 2013b) at a lower resolution (1.47 μm voxel size) (Carter et al., 2013a, Carter et al., 2013b). The lacunar density values we found in the femoral samples are consistent with those we reported recently (Dong et al., 2013b) and with those reported by Carter et al. (Carter et al., 2013b) for the same anatomical region in women across their lifespan. In another study, significant variations were observed between anterior-posterior and medial-lateral regions with differences of up to 30 % between the regions in single individuals, but no significant impact of age on N.Lc/BV (Carter et al., 2013b). Moreover, they found a significant decrease in the lacunar volume with respect to donor age (R^2=0.46), whereas the younger group's lacunae were ~30 % larger (age: < 50 years) than those of the older group (age: >50 years). In contrast, there was no impact of age on lacunar size reported by others (McCreadie et al., 2004).

We observed pronounced differences between jaw bones compared to the two peripheral skeletal bone sites. This may be explained by the different origin of the cells and the different remodeling rates in those tissues, or the different mechanical environment. While osteocytes in the peripheral skeleton derive from the trunk lateral plate mesoderm, in the mandible they derive from the paraxial mesoderm (Russell *et al.*, 2008, Bonnet *et al.*, 2013). The remodeling rate in jaw bone is believed to be higher than in femur and tibia (Yu *et al.*, 2012, Bertoldo et al., 2007), which leads to a lower mineralization and mass density (Ruffoni et al., 2007) in the jaw. The latter has been only partly confirmed in our study by means of lower distribution values of MDD^r (mean, low and high) and a higher intra-specimen variability (in terms of FWHM) in the jaw bones compared to tibia (Fig. 3-15 F-J). However, we observe a trend towards smaller values for jaw compared to femur (mean, low and high), which is in line with the lower remodeling rate in the femur reported earlier (Huja et al., 2006).

The majority of the osteocyte lacunar volumes were in the range between 100 and 400 µm³, which is in agreement with values reported in other studies (Carter et al., 2013b, Carter et al., 2013a, Dong et al., 2013b). However, a small fraction of very large osteocyte lacunae with volumes between 400 and 1000 µm³ was found in the jaw bone samples (Fig. 6). Most strikingly, this characteristic asymmetric distribution of osteocyte lacunar volumes was almost identical in healthy and BP treated jaw bone samples (Fig. 7). The only significant effect of the BP treatment in jaw bones appeared to be the reduction of lacunar density, which was also evident in the increased average distance between the extracellular matrix and the closest osteocyte lacuna. On average, the samples treated with BP had a 14.8 % lower lacunar density than the healthy jaw bone controls, but still 15 % higher than the femur samples. Mass density (mean, low, and high values) was not significantly higher in the jaws treated with BP compared to the healthy controls, although these values were marginally higher and the heterogeneity (FWHM) was slightly lower than those in the control group. Therefore, it must be concluded that no remarkable changes of mass density occur in the extracellular matrix after BP treatment. For comparison, the mass density distribution values of the jaw bones treated with BP do not reach the values observed in tibia and femur samples. However, with the current analysis we cannot exclude potential local changes, for example directly at the pore tissue boundary. It is well accepted that osteocytes actively remodel their direct extracellular environment (Qing et al., 2012) and it has been shown by fluorescence-labeled risedronate injected intravenously in a murine model that BP is indeed deposited around the osteocyte lacunae (Roelofs *et al.*, 2010). Interestingly, the results of that study have suggested that the deposition rate was not uniform in all osteocytes, but decreased with the distance to the next vascular channel. Therefore, a dedicated regional analysis of the lacunar-matrix interface merits further investigation. Overall, except for the reduction in osteocyte lacunar number, the changes of the lacunar network and the mass density of the extracellular matrix appeared to be marginal. In particular, the BP-induced parameter alterations in the jaw stayed within the variations observed between different anatomical sites. Consequently, the observed parameter variations are not likely to be primary causes for the development of BRONJ in the jaw.

In this study, we have not investigated the lacunar occupation rate and viability of osteocytes, as the increased number of abandoned osteocyte lacunae is a well-documented sign of BP treatment in the jaw (Bonnet et al., 2013, Maurer *et al.*, 2011). Moreover, the filling of empty lacunae with mineral has been reported in several studies (Frost, 1960, Carpentier et al., 2012,

Busse et al., 2010), which is in line with the reduced lacunar density we observed in the jaw bones treated with BP. It is known that BPs have a high affinity to hydroxyapatite (Russell et al., 2008). Therefore, we hypothesize that higher perfusion and turnover rates initially lead to a higher deposition of BP in the human jaw compared to other human sites, which is in line with finding of previous animal studies (Bertoldo et al., 2007). At higher doses BP becomes cytotoxic (Allen & Burr, 2008), which presumably promotes the gradual depletion of osteocytes and allows the abandoned pores to be filled with more BP-loaded mineral. Finally, acidification of this tissue, caused for example by an inflammation, which is known to occur in BRONJ, can result in an excessive dissolution of BP-loaded mineral and a release of toxic doses of BP. Among the multifold biological factors promoting the development of a necrosis in the jaw, the fraction of large lacunae (> 400 μm^3) found in jaw bone tissue but not in the tissues from the other skeletal sites may be a structural factor, since it allows the deposition of larger amounts of highly concentrated BP-loaded mineral in such abandoned lacunae, which when washed out, results in higher and thus more toxic local BP doses.

We did not observe significant differences between the different groups for the vessel porosities, which supports the idea that the observed differences of lacunar properties and mass density distributions between the different groups are not linked to potential differences of vessel porosities in the investigated specimens. The reported pore volume ratios are within the range previously shown for femoral cortical bone (Dong et al., 2013b). However, the quantification of vessel porosities was limited in our study due to the size of the field of view, which was small compared to the average distance between individual vessels. Therefore, the field of view cannot be considered to be a representative volume with respect to the vessel network.

This study has several limitations. A drawback of the present study is that the comparison between sites and even within the jaw bone is hampered by our limited ability to control the exact anatomical location and orientation of the harvested samples and the underlying diagnosis. Moreover, the samples from femur, tibia, and jaw bones could not be collected from the same donors, and duration and type of BP treatment was not uniform within the BRONJ group. Potentially influencing factors, e.g. intra-specimen variability, age and gender, as well as the BP treatment conditions, could have biased our analysis. Also, in contrast to previous investigations, in which we have demonstrated the feasibility to extract absolute mass density values from the phase contrast images (Varga et al., 2013, Langer et al., 2012b),

we report relative values in this study. This is due to the fact that (i) the large distance between sample and detector in the current configuration violated the near-field condition, which is an essential prerequisite for the Paganin-phase retrieval used (Weitkamp et al., 2011) and (ii) we used a constant ratio of delta over beta for the Paganin retrieval even though it could have been different between samples with different degrees of mineralization (Langer et al., 2014).

Nevertheless, the subtle ultra-structural alterations observed in the BP treated jaws underline the need of further sophisticated investigations of large tissue volume with sub-micron resolution, high sensitivity to local changes in mineral density and chemical composition of the tissue. Such changes are not likely to be depicted by conventional X-ray methods. Phase contrast tomography with voxel sizes ranging down to about 50 nm is now available at SR sources and may provide new hints towards the ultra-structural mechanisms leading to the pathogenesis of BRONJ.

3.3 CANALICULAR NETWORK MORPHOLOGY IS THE MAJOR DETERMINANT OF THE SPATIAL DISTRIBUTION OF MASS DENSITY IN HUMAN BONE TISSUE - EVIDENCE BY PHASE-CONTRAST SYNCHROTRON RADIATION NANOCT.

3.3.1 ABSTRACT

Under healthy conditions bone undergoes continuous remodeling. Newly formed osteonal bone maturation is associated with a rapid primary and then slower secondary increase of mineralization. This increase requires the supply and precipitation of mineral into the bone matrix. The mineral delivery can only occur from the extracellular fluid via interfaces such as the Haversian system and the pore network of osteocytes. Osteocytes, the most abundant type of bone cells, are believed to actively participate in the calcium homeostasis by accessing a rapid exchangeable calcium pool of bone via osteolysis. We hypothesized that mineral exchange in both secondary mineralization and in the course of mineral homeostasis are achieved by the diffusion of mineral from the lacuno-canalicular network to the bone matrix and vice versa, resulting in a gradual change of tissue mineralization with respect to the distance from the pore-matrix interface. We expected to observe alterations in the mass density distribution with tissue age. We further hypothesized mineral exchange to occur not only at the lacunar, but also at the canalicular boundaries. The aim of this study was therefore to investigate the spatial distribution of mass density in the peri-lacunar and peri-canalicular bone tissue using phase-contrast synchrotron nanoCT with 50 nm voxel size and to evaluate if density gradients exist in human jaw bone specimens originating from four healthy donors and four treated with high-dosage bisphosphonate. Our results show the first experimental evidence that mass density in the direct vicinity of both lacunae ($p<0.001$) and canaliculi ($p=0.04$) are different from the mean matrix density, resulting in gradients with respect to the distance from both pore-matrix interfaces. The density gradient was more pronounced around the lacunae than around the canaliculi, which was explained by geometrical considerations in the morphology of the LCN. We conclude that the observed mass density gradients are unlikely to be impacted by processes caused by short term exchanges occurring in mineral homeostasis.

3.3.2 MATERIALS AND METHODS

3.3.2.1 Sample preparation

In the present study, data were taken from human jaw bone sections originating from four healthy subjects (aged 19, 40, 42, and 47 years, respectively) and four patients suffering from bisphosphonate related osteonecrosis of the jaw (BRONJ) (aged 40, 70, and 72 years, respectively, for one sample, the donor age is unknown). All specimens but one originated from female donors. The specimens (cubes of about 1 mm^3 in size) were extracted during the surgical interventions necessary for the treatment of the necrosis. Healthy control samples were obtained from debris during wisdom tooth removal. All sections originated from similar anatomical regions of the mandible. All patients signed an informed consent form. Ethical approval was granted by the Ärztekammer Bremen. After removal, the bone specimens were placed in tissueTec (Sakura Finetec, USA, Inc) and stored frozen at a temperature of -20 °C until further processing. Following thawing, the specimens were milled down to a diameter of about 0.5 mm using a high precision lathe. For the BRONJ samples, this sub-volume was selected from a region in which no apparent sign of necrosis was observed. The samples were then fixed in 70 % ethanol. At least 12 hours prior to imaging the samples were placed inside the measurement hutch in order to allow adjustment to humidity and temperature.

3.3.2.2 Image acquisition and reconstruction

Phase-nano computed tomography (PNCT) measurements were carried out on beamline ID 22 NI at the ESRF (France) following the protocol described elsewhere (Langer et al., 2012b). Briefly, each sample was first scanned at 350 nm voxel size to obtain an overview of the sample using just 1200 projections of 0.2 s each, to keep the dose as low as possible. This was used to assist the selection of a region of interest, which was then scanned with a higher resolution. Radiographs were collected at four different distances from the detector corresponding to 50 nm pixel size (focus-detector distance: 526,2 mm, distances focus-sample: 36.1, 37.1, 41.1, 51.1 mm), having four times 2999 projections for each 0.2 s of illumination. The field of view corresponding to the chosen settings was about 100 µm in diameter and length. The energy of the beam was set to 16.874 keV allowing for sufficient transmission and high contrast at the same time. Based on the tomographic scans, phase maps were retrieved for each angle (Langer et al., 2012b, Cloetens et al., 1999). From the phase maps δ was reconstructed and stored in units of $\frac{2\pi}{\lambda}$ (λ =0.735 Å) using the filtered back

projection algorithm. The complex refractive index is $n = 1 - \delta + i\beta$. For a given energy of the X-ray beam, the absorption index, β, is proportional to the linear attenuation coefficient, μ, while δ is proportional to the electron density. The conversion from δ to mass density can be approximated by: $\delta \approx 1.3 \cdot 10^{-6}\ \rho\ \lambda^2$, with λ being in units of Å and ρ in units of $\frac{g}{cm^3}$ (Langer et al., 2012b).

The spatial resolution was determined based on line profiles of the image grayscale values evaluated across several apparently sharp interfaces between mineralized and non-mineralized regions. These profiles were fitted with an error function, full width at half maxima (FWHM), which was used to define the physical spatial resolution. The FWHM of the error function fitted to sharp interfaces was found to be smaller than 6 voxels (300 nm)

3.3.2.3 Segmentation

Following image reconstruction, all data processing was performed using Matlab (MATLAB R2012a, The MathWorks Inc., Natick, MA). Within the reconstructed volumes, 3D rectangular regions of interest (VOI) were manually selected by avoiding microcracks. For the samples from healthy subjects, the tissue type of the VOI was determined using the overview scans and defined as either osteonal or interstitial tissues based on the osteonal patterns. In the case of specimens originating from patients suffering from BRONJ, only interstitial tissue regions were selected for further analysis.

The floating 2048 x 2048 x 2048 row data (32 bit) was converted into 8 bit (grey level) to reduce the size of each dataset from 32 to 8 GB. 3D Gaussian filtering with standard deviation of one pixel was applied to reduce noise. Due to noise and the very fine structures that had to be resolved, a single threshold method did not give sufficiently good results, therefore the segmentation of the LCN pore network within the VOI was performed by applying a hysteresis-based method based on two threshold levels identified on the grayscale histogram for each VOI individually. The two threshold values used in the hysteresis-based method were computed from the histograms, which showed two distinguishable peaks (one corresponding to the mineralized tissue, the other corresponding to the non-mineralized LCN). The initial threshold (th_1) was defined at the first inflection point of the mass density histogram in log-scale below the peak position (Mode). The second threshold (th_2) was defined as: $th_2=th_1-(Mode-th_1)$, see Fig. 3-18.

Small features, considered to be noise, were removed using a morphological opening with kernel radius of two voxel and by cleaning islands smaller than 0.2 μm^3. The osteocyte lacuna was separated from the canaliculi using a morphological opening with 10 voxels, followed by a dilatation with 3 voxels.

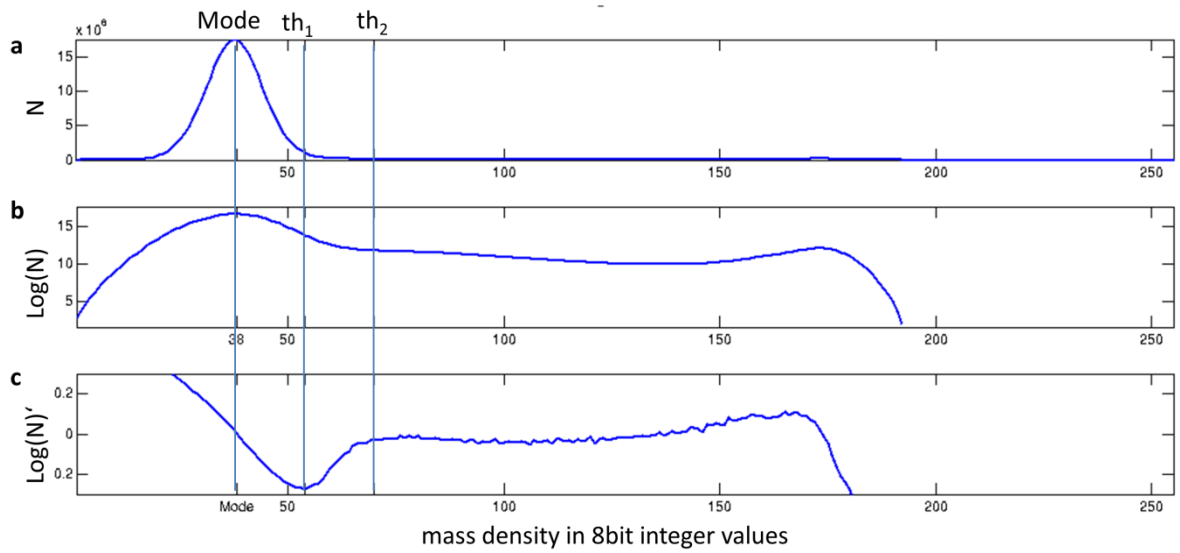

Fig. 3-18 The histogram of one VOI after conversion into 8bit integer values is shown in a. and b. c shows the first derivative of b. The mode and the two thresholds used in the hysteresis method are indicated.

3.3.2.4 Quantification of the LCN morphology, the peri-canalicular and peri-lacunar mass density

The volume of mineralized tissue (BV) within the VOI was calculated by counting the voxels identified as no pores. The lacunar volume (Lc.V), the lacunar surface (Lc.S), the aspect ratios of the lacunae ($Lc.Ar_{13}$, $Lc.Ar_{12}$, $Lc.Ar_{23}$), and canalicular volume (Cn.V) was quantified from the corresponding segmented images and the canalicular porosity (Cn.V/BV) was computed.

The lacunar aspect ratios were calculated from the three eigenvalues of the co-variance matrix of the lacunar mask. (Dong et al., 2013b).

The mean diameter of the canaliculi (Cn.Dm) was calculated based on the method introduced in (Hildebrand & Rüegsegger, 1997) after upsampling the image by a factor of 2 in order to archive higher precision for the voxel-based measure.

The distance of the mineralized tissue to the LCN was quantified using the distance transform with the Euclidean metric. The median of the distance transform corresponds to the distance within which 50 % of the matrix is located relative to the LCN. This was quantified independently for the canaliculi and the lacunae, denoted with $Cn.Dist_{50}$ and $Lc.Dist_{50}$, respectively.

Due to the local nature of the tomography, i.e. not the whole cross section of the sample was within the field of view, the image grayscales were shifted with a global offset value, which was corrected for each VOI individually based on the mean gray value within the pores. The mean and standard deviation of mass density *(ρ)* of the mineralized tissue was calculated within the volume of the segmented bone matrix, which was eroded with 5 voxels in order to minimize partial volume effects. Moreover, ρ was evaluated as a function of distance (*d*) from the lacuna (Fig. 3-21f) and the canaliculi (Fig. 3-21f) independently. The functions *ρ(d)* were characterized as being within the range of 0.35 – 2.3 µm (7 and 46 pixels) distance from the LCN. The lower limit was selected in order to avoid partial volume effects in the direct neighborhood of the pores (Fig. 3-21e-f). The higher limit was set so that at this distance a sufficient amount of bone matrix is still included in the peri-canalicular analysis (Fig. 3-21d).

The following exponential function was fitted to each *ρ(d)*:

$$\rho(d) = \Delta\, exp(-\tau d^{p}) + c, \qquad (3\text{-}1)$$

where Δ, p and c are the parameters to be fitted and p was restricted to be within [0, 3]. The value for the mass density adjacent to the pore boundary was defined as $\Delta + c$. The difference of density between the pore boundary and the tissue at a remote distance was defined to be Δ. Given the fixed range of distance used to evaluate these parameters, Δ characterizes the mass-density gradient and thus will be referred to from now on as mass density gradient. Examples of the fits to the data are shown in Fig. 3-24.

3.3.2.5 Impact of LCN morphology on peri-LCN mass density

We assumed that the increase of tissue mineralization occurs due to the diffusion of mineral from the fluid filling the pericellular volume (PCV) between the osteocyte and the mineralized wall (see Fig. 3-25). Both the peri-lacuanar and the peri-canalicular gradients may depend on the diffusion constant, D, of mineral diffusion from the pericellular fluid into

the peri-LCN mineralized tissue, as well as on the morphology of the LCN. In recent experimental (Price *et al.*, 2011) and numerical (Kamioka *et al.*, 2012, Verbruggen *et al.*, 2013) studies it has been reported that the pericellular fluid flows with velocities of tens to hundreds of μm per second. Therefore we assumed that the mineral concentration in the PCV is the same in the PCV of the lacuna and the PCV of the adjacent canaliculi.

We also assumed that the diffusion constant is the same at the canaliculi-ECM and lacunae-ECM interfaces and thus the diffusion of mineral from the pericellular fluid into the mineralized matrix only depends on the ratio of the fluid-matrix interface area to the peri-LCN tissue volume. The ratio of the interface area and a unit volume defined to be located within a distance r_e to the LCN is denoted as relative flux (f'). The derivation of f' is shown here:

The surface area of the canaliculi ($A.Cn$) is given by:

$$A.Cn = 2\pi rl, \qquad (3\text{-}2)$$

with r being the radius and l being the length of the canaliculi. The volume of peri-Cn tissue within r_e can be formulated by:

$$V_{peri-Cn} = l\pi(r + re)^2 - l\pi r^2. \qquad (3\text{-}3)$$

The surface area of the lacuna ($A.Lc$) is approximated by:

$$A.Lc \approx 4\pi \left(\frac{(ab)^{1.6}+(ac)^{1.6}+(bc)^{1.6}}{3}\right)^{0.625}, \qquad (3\text{-}4)$$

with the length of the half-axes defined by *a, b, c*. The volume of peri-Lc tissue within r_e is calculated as:

$$V_{peri-Lc} = (\frac{4\pi}{3}(a + re)(b + re)(b + re) - (\frac{4\pi}{3}abc)). \qquad (3\text{-}5)$$

The relative flux at the lacunar and canalicular boundary are defined as

$$\text{Relative flux at Cn: } = \frac{A.Cn}{V_{peri-Cn}} \qquad (3\text{-}6)$$

and

$$\text{Relative flux at Lc: } = \frac{A.Lc}{V_{peri-Lc}}, \qquad (3\text{-}7)$$

respectively.

3.3.2.6 Statistical analysis

Statistical analyses were performed using Matlab (MATLAB R2012a, The MathWorks Inc., Natick, MA). The correlation between properties is quantified by R and p (Pearson's correlation) based on the jaw bone sections originating from healthy subjects. Differences between mass density adjacent to the lacunae or canaliculi and the mean mass density of the respective VOI were assessed by analyses of variance (ANOVA). All statistical results were considered significant for $p < 0.05$.

3.3.3 RESULTS

Synchrotron radiation phase nanoCT allowed for quantitative imaging of the mass density of the mineralized bone matrix (Fig. 3-19) and the LCN (Fig. 3-20). The resolution enabled segmentation of both, lacunae and canaliculi (Fig. 3-21). However, due to the small size and number of the VOIs, the lacunar morphology parameter could not be included in the statistical analysis. In 14 out of 23 investigated VOIs, for which the lacunae were completely within the VOI, the means and standard deviations of the lacunar volume (Lc.V = 646 ± 147 µm³), surface area (Lc.S = 484 ± 90 µm²), surface to volume ratio (Lc.S/Lc.V = 0.75 ± 0.14), and aspect ratios ($Lc.Ar_{13}$ = 4.1 ± 0.4, $Lc.Ar_{12}$ = 2.1 ± 0.2, $Lc.Ar_{23}$ = 2.0 ± 0.3) were quantified.

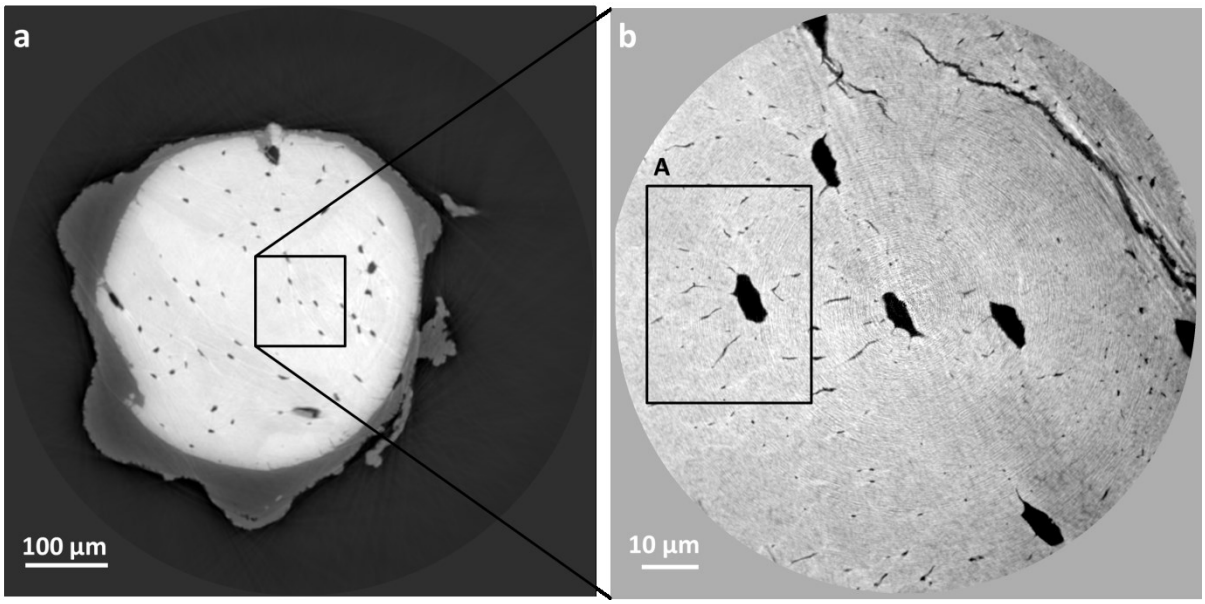

*Fig. 3-19 Reconstructed slice of the overview scan at 350 nm pixel-size **(a),** with the indicated region chosen for the actual phase nanoCT. A reconstructed slice of the phase nanoCT scan is shown in **b**. One volume of interest is indicated in **b** by A.*

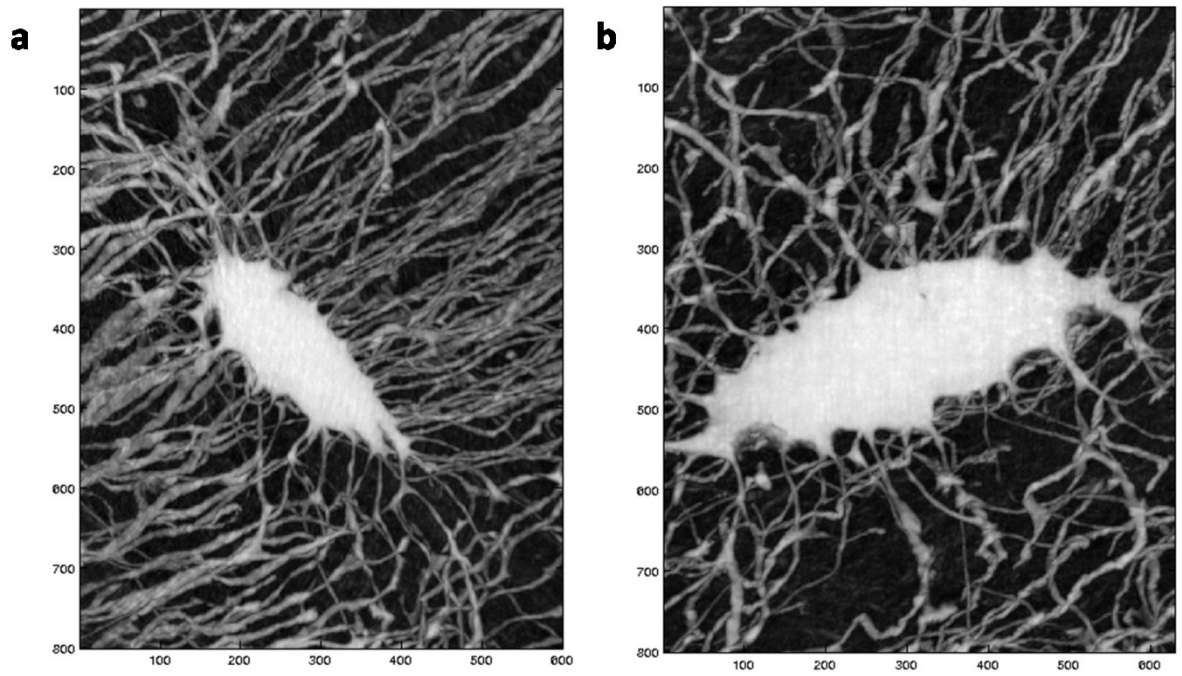

Fig. 3-20 Minimum intensity projections along z (a) and y (b) of the volume of interest indicated in Fig. 1b. The size of the shown volume of interest is z = 630 pixel, x = 800 pixel and y = 600 pixel (200 pixel = 10 µm).

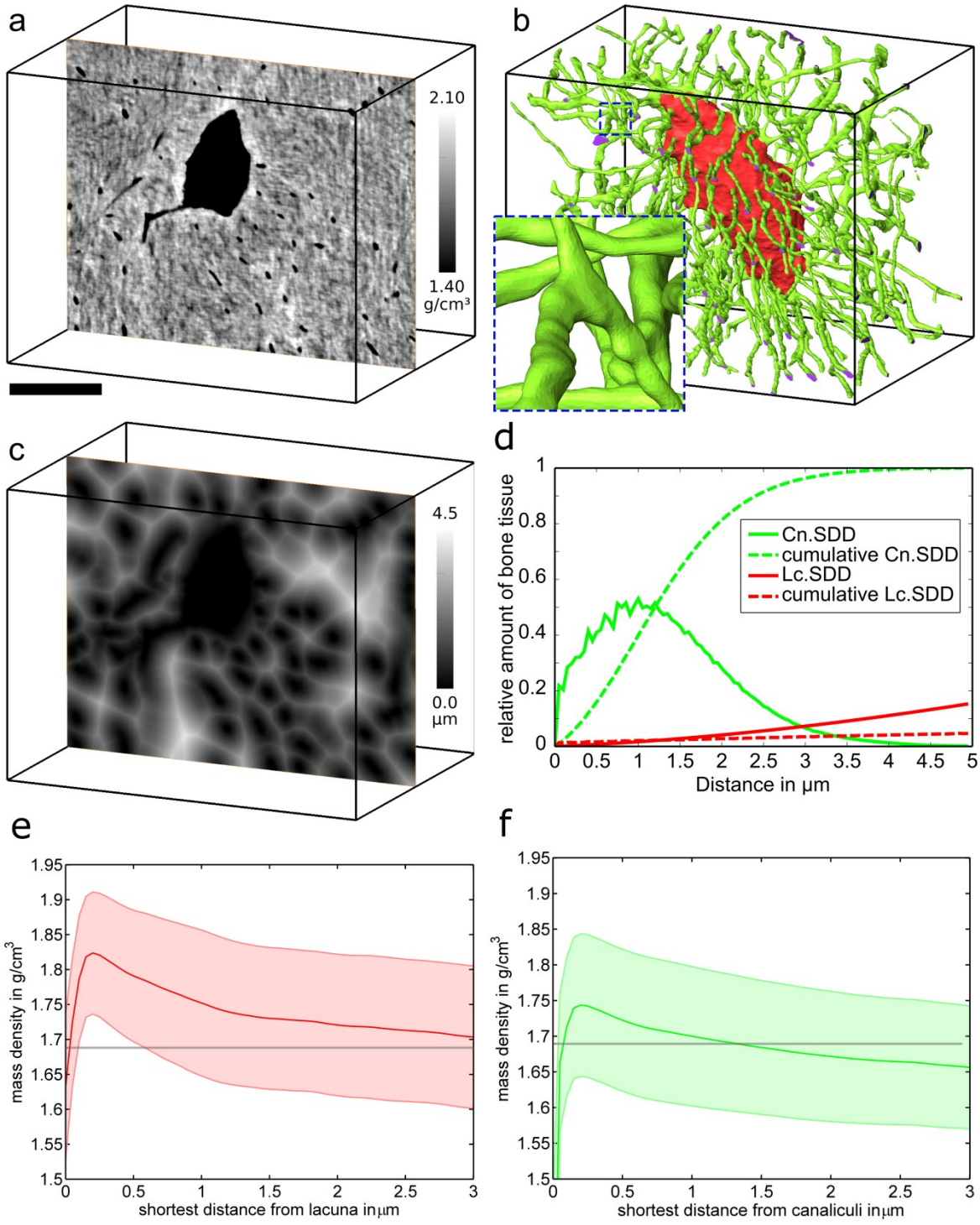

Fig. 3-21 Assessment of the peri-lacunar and peri-canalicular bone tissue mass densities. ***a****, One slice of a volume of interest containing one osteocyte lacuna, cropped from the 3D reconstructed SR-PNT image. The VOI dimensions are 800 by 600 by 630 pixels. The gray scale corresponds to mass density and the scale bar to 10 µm.* ***b****, Surface representations of the lacunar (red) and canaliculi (green) compartments segmented from the same image volume.* ***c****, Distance transform image showing the shortest distance from each point in the*

matrix to the LCN. ***d****, Histogram of the 3D distance transform considering only the canaliculi (green) and the lacuna (red) and their cumulative functions for one ROI. From the solid lines one can see that 50 % of the bone tissue is within about 1.2 µm distance to the canaliculi, while at this distance the cumulative function of the histogram of the distance transform considering the lacuna is only about 10 times smaller.* ***e*** *and* ***f****, Average mass density and standard error bands as a function of the shortest distance to the osteocyte lacuna (****e****) and canaliculi (****f****), shown for one VOI. The grey horizontal lines represent the mean mass density of the ROI.*

3.3.3.1 Canalicular morphology

The canalicular porosity was found to be around 2 % with large variability between the individual VOIs and non-significant variations of the means with respect to the tissue groups (Table 3-5). The average Cn.Dm and $Cn.Dist_{50}$ of all analyzed ROIs was found to be 0.38 ± 0.04 µm and 1.3 ± 0.4 µm, respectively.

After pooling all the morphological parameters from osteonal and interstitial VOIs of the control groups, significant correlations were found between canalicular porosity Ca.V/BV and diameter Ca.Dm, and between Ca.V/BV and $Cn.Dist_{50}$ (Table 3-6).

3.3.3.2 Peri-canalicular and peri-lacunar mass density properties

We found the smallest mean mass density in osteonal and the largest in BRONJ tissue, respectively (*Table* ***3-5***). Moreover, ANOVA revealed that mass densities in the tissue adjacent to both lacunae ($p<0.001$) and canaliculi ($p=0.04$) were significantly different from the average matrix mass density. This resulted in gradients with respect to the distance from both the peri-lacunar (*Fig. 3-21*e) and the peri-canalicular (*Fig. 3-21*f) regions. Both the magnitude and the gradient of density were higher around the lacunae compared to the canaliculi (*Table* ***3-5***). The adjacent pore density appeared to be independent of tissue age except for the peri-canalicular domains in the osteonal regions. The most pronounced peri-lacunar and the peri-canalicular mass density gradients were observed in osteonal tissue and interstitial tissue, respectively. The analysis of one representative VOI revealed that the peri-canalicular mass density gradient was independent of the distance to the lacuna (Fig. 3-22).

The peri-canalicular density was found to correlate with both peri-lacunar and peri-canalicular mass density gradients and the mean tissue mass density (Table 3-6). The latter also correlated to the peri-lacunar gradient.

Table 3-5 Mean and standard deviation of properties reported for osteonal tissue, interstitial tissue and bone originating from patients suffering from BRONJ. Ca: canaliculi, BV: bone volume, Dm: diameter, $Dist_{50}$: Distance to canaliculi boundary in which 50 % of the BV are located in, ρ: mean mass density of the BV, Δ: difference in mass density of the tissue adjacent to the pore boundary to tissue furthest away from the pore boundary, Lc: Lacuna.

	osteonal	interstitial	BRONJ
number of different donors	1	4	4
age of donor	47	19,40,42,47	44,70,72,n.k.
number of ROI	3	11	9
Ca.V/BV in %	2.0 ± 0.5	1.8 ± 0.8	2.3 ± 0.8
Ca.Dm in µm	0 .36± 0.01	0.37 ± 0.04	0.40 ± 0.04
Ca.Dist $_{50}$ in µm	1.2 ± 0.1	1.4 ± 0.5	1.3 ± 0.4
ρ in g/cm^3	1.61 ± 0.03	1.72 ± 0.04	1.78 ± 0.05
Δ peri-Lc ρ in g/cm^3	0.29 ± 0.09	0.13 ± 0.06	0.14 ± 0.10
ρ adjacent to Lc in g/cm3	1.86 ± 0.16	1.85 ± 0.03	1.86 ± 0.12
Δ peri-Ca ρ in g/cm^3	0.02 ± 0.03	0.12 ± 0.08	0.04 ± 0.17
ρ adjacent to Ca in g/cm3	1.62 ± 0.01	1.79 ± 0.04	1.79 ± 0.05

Table 3-6 Correlations between properties are quantified by p and R values. Only jaw bone tissue from healthy subjects is considered in this analysis.

Correlation	p - value	R - value
Ca.V/BV vs. Ca.Dm	0.002	0.75
Ca.V/BV vs. Ca.Dist $_{50}$	<0.001	-0.85
ρ vs. Δ peri-Lc ρ	<0.001	-0.88
ρ vs. ρ adjacent to Ca	<0.001	0.85
Δ peri-Lc ρ vs. ρ adjacent to Ca	<0.001	-0.83
Δ peri-Ca ρ vs. ρ adjacent to Ca	0.029	0.58

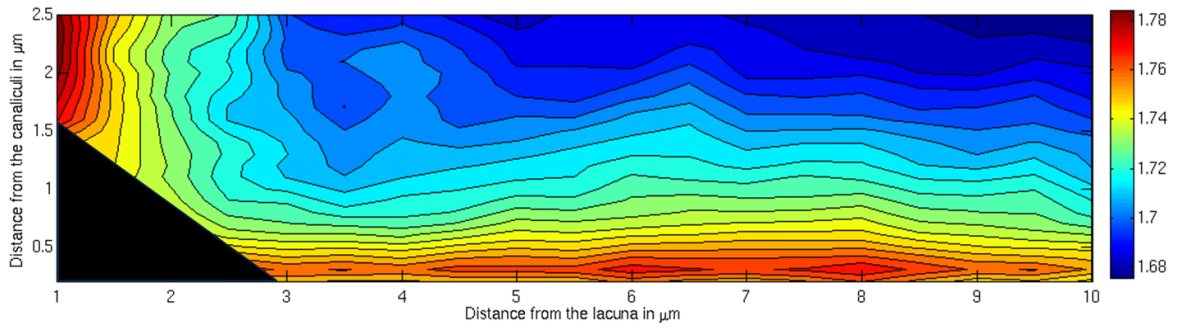

Fig. 3-22 Contour plot of mass density as a function of the distance from both the lacuna and the canaliculi, shown for one representative volume of interest. The region close to the intersection of the canaliculi with the lacuna was not considered, due to artefacts caused by the overlapping masks in this region.

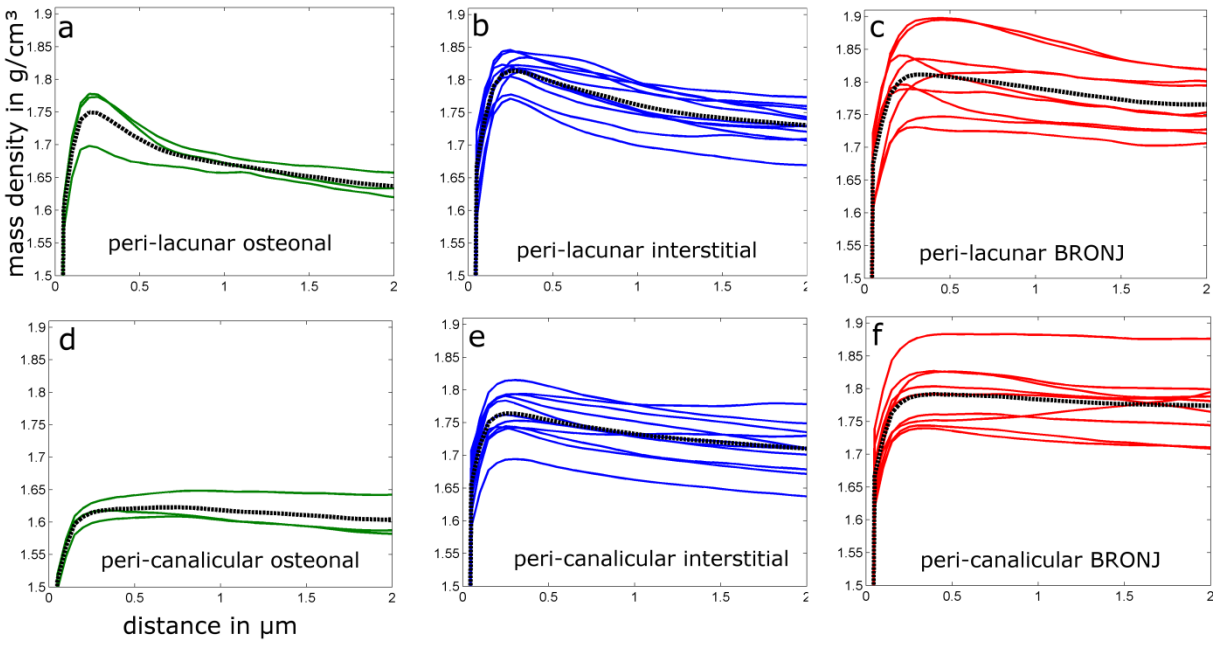

*Fig. 3-23 Average mass density as a function of the shortest distance to the osteocyte lacuna (**a, b, c**) and canaliculi (**d, e, f**), shown for regions of interest originating from osteonal (N = 3) (**a, d**) and interstitial (N = 11) tissue (**b, e**) regions as well as from BRONJ (N = 9) bone tissue (**c, f**). In each sub-figure the average of the measured relationships between mass density and distance is also shown with black dashed lines.*

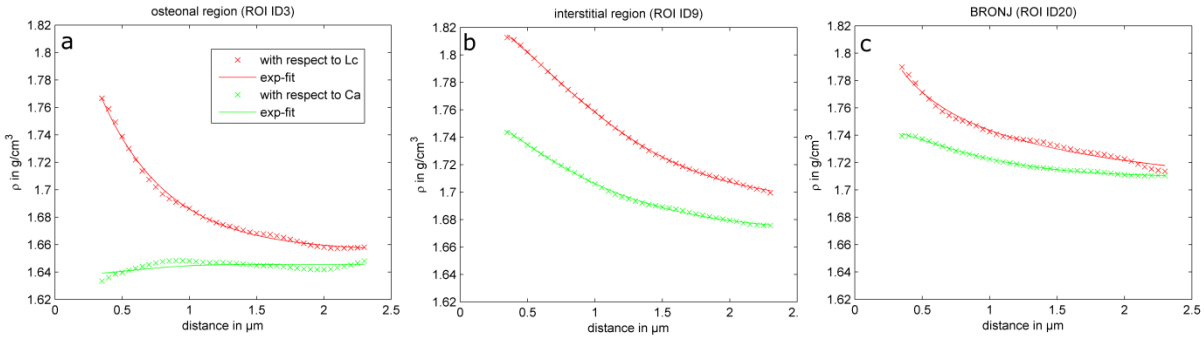

Fig. 3-24 Peri-lacunar (red) and peri-canalicular mass density distributions as a function of distance to the respective pore boundary are plotted for three different ROIs.

3.3.3.3 Impact of LCN morphology on peri-LCN mass density

We calculated higher values of relative flux (f^r) for lacunar compared to canalicular geometrical assumptions (*Fig. 3-25*d).

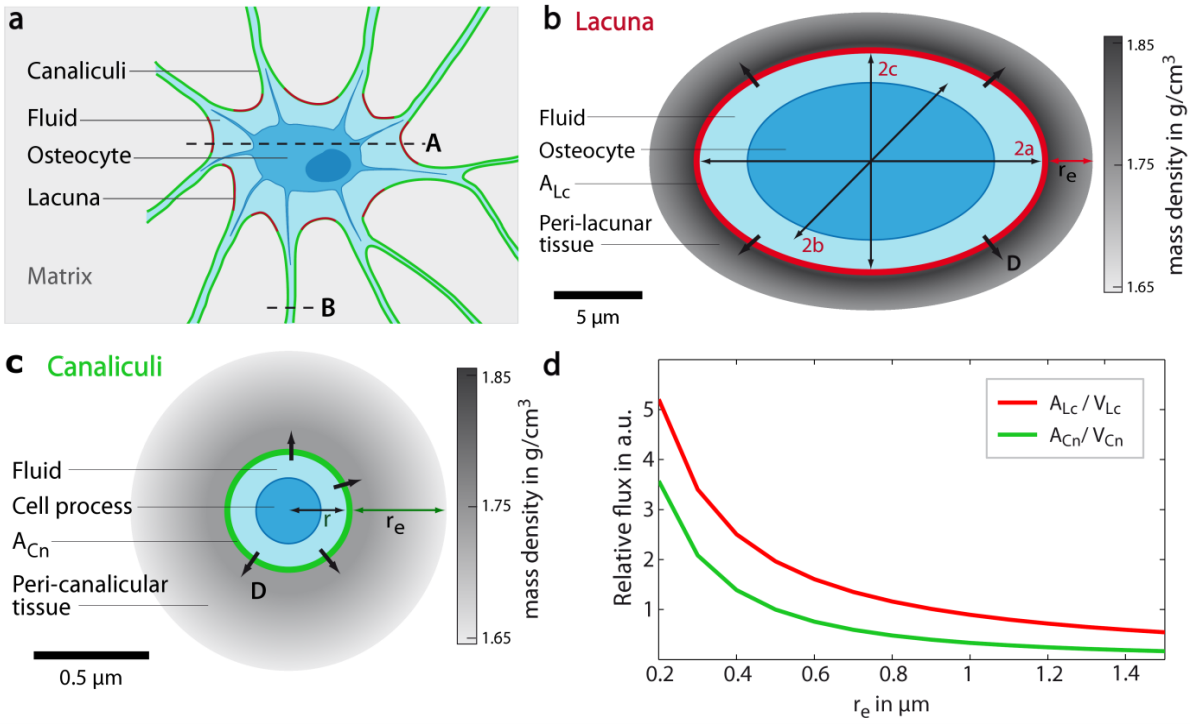

Fig. 3-25 Illustration of the model of the mineral flux from the extracellular fluid into the peri-lacunar ***(b)*** *and peri-canalicular* ***(c)*** *tissue. The extracellular fluid is indicated in light-blue. a: Schematic drawing of an osteocyte and its processes housed in the lacuna and canaliculi, respectively. The interface from the lacuna to the peri-lacunar space and from the canaliculi to the peri-canalicular space is indicated in red and green, respectively. The dashed lines at A and B indicate the cross-sections shown in* ***(b)*** *and* ***(c)****, respectively. b:*

Schematic drawing of a lacuna approximated as ellipsoid, characterized by the length of the half-axes (a> b> c). The density of the peri-lacunar tissue is represented by grey values. ***c****: Schematic drawing of* ***a*** *cross-section through a canaliculi.* ***d****: The relative flux, defined as surface by peri-pore volume ratio, is plotted considering the lacunar (red) and the canalicular boundary (green) as a function of the distance* r_e*. In* ***(d)*** *the lacunar sizes were set to a= 10 µm, b=5 µm, c=2.5 µm, the canaliculi were approximated to have a cylindrical shape with 0.5 µm diameter.*

3.3.4 DISCUSSION

Recent advancements in synchrotron-based X-ray tomography with phase contrast have provided a new insight into the fine structure of the extracellular matrix of bone. In the present study we utilized SR-PNT to investigate the 3D LCN morphology and the peri-LCN tissue mass density distribution in human jaw bone.

3.3.4.1 Lacunar and canalicular morphology

The values of the lacunar morphology of the osteocyte lacunae investigated in this study are in agreement with those reported by others (Dong et al., 2013b, Carter et al., 2013b). Therefore, the investigated VOIs can be considered to be representative.

As expected, the magnitude of the canalicular porosity in healthy tissue appears to be determined by both the diameter of canaliculi and the distance between them. The latter is reflected by 50% - distance of the mineralized matrix from these pores. The fact that the distance of the matrix from the canaliculi was not altered in the tissue treated with BP suggests that the observed trend of increased canalicular porosity may primarily be due to the larger canalicular diameter. However, the large variability of Cn.V/BV between the individual VOIs would require much more data to statistically support this hypothesis. $Cn.Dist_{50}$ was found to be slightly smaller in osteonal compared to interstitial tissue, suggesting a better accessibility to the ECM in young tissue. Moreover, some canaliculi may be filled with increasing tissue age.

Recent studies on human bone sections reported that 50 % of the mineralized bone tissue is located within about 65 µm and 14 µm of the nearest Haversian canal and lacuna, respectively (Dong et al., 2013b, Hesse *et al.*, 2014). By including the canaliculi in a similar consideration, we find that 50 % of the mineralized tissue is located within a distance of less than 1.4 µm

from these pores. This is in line with findings of other recent studies (Kerschnitzki et al., 2013) and underlines the important role of canaliculi not only for the cell-cell contact, and the transport of nutrition, signaling molecules and waste products from the Haversian system to the cells, but also for the potential interaction with the extracellular tissue matrix.

3.3.4.2 Peri-canalicular and peri-lacunar mass density distributions

As expected, the mean tissue mass density increased with tissue age as a consequence of the secondary mineralization process (Ruffoni et al., 2007, Parfitt, 2003). However, for the first time we report that this increase does not occur homogeneously across the mineralized matrix, but as a function of distance from the LCN boundaries. The mass density adjacent to the pores was found to be higher compared to the average density further away from the interfaces, resulting in characteristic mass density gradients. The tissue directly surrounding the osteocyte lacunae was reported earlier to be distinctly different from the matrix not in contact with the lacunae (Nicolella *et al.*, 2008). Here we showed that the mass densities of both, the peri-lacunar and the peri-canalicular tissues are different compared to those of more remote tissue regions.

3.3.4.3 Diffusive mineralization of bone tissue through all pore boundaries

We speculated that the observed density gradients are the consequences of a diffusive mineralization process, which incorporates the supply and precipitation of mineral. Moreover, we hypothesize that the supply of mineral required for the mineralization process is available in the ECF filling the LCN. Calcium ions and other molecules required for the precipitation to hydroxyapatite can diffuse into and from the the extra-cellular mineralized matrix through all pore-boundaries including the canalicular surfaces, which is supported by our observation of gradual decreases of mass density from the interface towards tissue regions further away from the pores. With increasing tissue age, this process results in less pronounced gradients, i.e. a more homogeneous spatial distribution of mass density. We further suggest that tissue mass density has an upper limit, representing the mineral-saturated state of the mineralized matrix. These trends were consistent between osteonal and interstitial tissues from healthy donors, as well as in BP treated interstitial tissue. Our data suggests that the overall increase of tissue mineralization is not only due to an increase in the ratio of interstitial to osteonal tissue volume, as suggested by others (Fuchs *et al.*, 2011), but also due to the increase in tissue mass density in ageing interstitial tissue.

The existence of mineral exchange between the ECF and the mineralized extracellular matrix may have special relevance in the homeostasis of mineral. Approximately 10 % fluctuations in the calcium level of blood, controlled mainly by PTH (Talmage & Mobley, 2008), have been reported to occur during a daily cycle (Jubiz *et al.*, 1972, Whalley, 2011). Rapidly exchangeable calcium resources are required to compensate for such daily fluctuations. Therefore, the direct access to the calcium reservoir of bone matrix through the LCN has an enormous potential. As the diffusion of molecules through the mineralized collagen matrix is slow, the canalicular network is an essential design feature to increase the contact surface and to reduce the diffusion length.

In the evaluated tissue samples we have observed that 50 % of the mineralized tissue matrix was within a distance of less than 1.4 µm relative to the canalicular pore boundaries. The cumulative distribution function (Fig. 3-21 d) can be used to approximate the thickness of the pericanalicular mineralized tissue matrix layer, which is required to provide sufficient calcium for the compensation of the daily fluctuations in the serum calcium level. The absolute amount of calcium stored in human skeleton has been estimated to be about 1 kg, while approximately 1 g calcium is solved in the in the ECF (Parfitt, 2003). The daily fluctuation of calcium in the ECF is around 10 % (corresponding to 100 mg) (Jubiz et al., 1972). However, the total calcium flux between bone and the ECF has been reported to be > 6 g/day (i.e. 0.6 % of the total amount of calcium stored in the bone), of which only around 400 mg/day is provided by osteoclastic/osteoblastic remodeling (Pirklbauer & Mayer, 2011). According to the cumulative distribution function of ECM (see Appendix A at the end of this Chapter 3.3) around the canalicular network, the required amount of calcium (6 g) is deposited within a distance of about 60 nm from the canalicular wall. Within a distance of 500 nm, ~ 100 g calcium, i.e. ~1700 % of the required rapidly exchangeable calcium is deposited an unknown portion of which is quickly soluble.

The measured mass density distributions around the LCN (Fig. 3-23) exhibit a pronounced peak, was most pronounced in young osteonal tissue in the peri-lacunar region and decreased with relative tissue age (i.e. interstitial tissues from normal and BP treated subjects). This increased mass density in the close proximity to the LCN boundary can be explained by an increased mineral particle thickness in tissue regions, in which the distance to the LCN network is less than ~2 µm, as observed by Kerschnitzki et al. in ovine plexiform tissue (Kerschnitzki et al., 2013). Although we could not determine whether the peak density

occurred directly at the fluid matrix interface or at a certain distance away from the interface (due to potential partial volume effects), we can conclude that it always occurred at distances much smaller than 500 nm (Fig. 3-23). This dimension is comparable to the thickness of a few mineral collagen fibrils (single fibril average diameter: 50-100 nm, (Fratzl & Weinkamer, 2007)). We hypothesize that a thin (<< 500 nm) ECM layer around the LCN is sufficient to provide the rapidly exchangeable calcium depot at short diffusion distances. Moreover, the higher mass density in this layer compared to more distant ECM regions provides a barrier against the free diffusion of calcium from the supersaturated ECF to distant ECM regions, which may decelerate the tissue-age related mineralization process.

3.3.4.4 Impact of LCN morphology on peri-LCN mass density

We observe differences between the peri-lacunar and peri-canalicular mass density densities, with the latter being in general lower. Further, the density gradient around the canaliculi was not yet present in the osteonal tissue. In line with the findings of different mineral particle thicknesses (Kerschnitzki et al., 2013) our data suggest that the diffusive mineralization process and mineral particle growth is either slower or is influenced by the morphology of the LCN. In fact, the ratio between pore surface to peri-pore tissue volume, defined as relative flux, was found to be smaller for canaliculi than for lacunae. Our calculations on the canalicular and lacunar surfaces and the peri-LCN tissue volumes suggest a higher flux of mineral into a unit volume adjacent to lacunae compared to a unit volume adjacent to the canaliculi, which could explain the observed differences in the peri-canalicular and peri-lacunar mass densities of these two tissue regions. Another potential explanation for this phenomenon is that the peri-lacunar tissue also receives supply from the adjacent canaliculi.

3.3.4.5 Limitations

The present study has several limitations, most notably the inhomogeneity of the groups in terms of variations in anatomical origin of the jaw specimens. Additionally, the different impact of different BP was not considered in the present study. A further limitation is the differing ages of the donors. Another issue is the size of the VOI's, which was (if possible) selected so that the lacuna is in the center of the VOI. Parameters such as canalicular porosity or the median of the distance transform might be affected by the VOI size. Additionally, since the tomography was performed locally (not the whole cross-section is inside the field of view) the reconstructed densities face a local offset that was taken into account by setting the offset to the mean mass density determined for the pores.

3.3.4.6 Conclusions

Here we show, by means of SR-PNT, that mass density in the direct vicinity of the LCN is different from the mean mass density of the bone tissue, resulting in mass density gradients with respect to the interface. This supports our hypothesis that ECM mineralization is achieved through diffusion of calcium from the ECF in the LCN to the bone matrix. We find that mass density of the tissue adjacent to the canaliculi and the magnitude of the mass gradients are smaller than those of the corresponding lacunae, which can be explained by the morphology of the LCN. We conclude that a thin ECM layer of much less than 500 nm provides i) the rapidly exchangeable calcium pool required for the compensation of daily fluctuations in serum calcium level and ii) a diffusion barrier against rapid mineralization of the entire ECM. With tissue age, the average mass density increases and the gradients disappear. Future studies using SR-PNT may help to investigate the diffusion and mineralization processes and their coordination by osteocytes or other factors. The role of the increased mass density adjacent to the LCN with respect to tissue age and LCN morphology should be taken into account in drug deposition studies and in mechanical models studying the mechanosensation of osteocytes (Verbruggen et al., 2012, Verbruggen et al., 2013, Wang *et al.*, 2007, Nicolella et al., 2008).

3.3.4.7 Appendix A: Mathematical modelling on the tissue distribution around the canaliculi

The amount of tissue in the vicinity (smaller than half of the distance between two canaliculi) can be computed from the histogram of the distance transform assuming the canaliculi to be cylindrical shaped with diameter (*Dm*). The amount of tissue (*h*) at a certain distance (x) from the canal boundary can be described by:

$$h(x) = (2\pi\, x\, + n)l, \qquad (3\text{-}8)$$

with *n l* corresponding to the surface area of the canaliculi and depend on *d* and the length (*l*) of the canal. For symmetry reasons *l* can be set to 1. The surface, *n*, becomes equal to $Dm\,\pi$.

The integral of the *h* (called cumulative function, *C*) can be written as:

$$C(x) = \int h(x)dx = \int 2\pi x + Dm\,\pi\, dx = \pi x^2 + Dm\,\pi x \qquad (3\text{-}9)$$

Reorganizing *C(x)* to *x(C)* gives:

$$x(C) = -\frac{Dm}{2} + \sqrt{\frac{Dm^2}{4} + \frac{C}{\pi}} \qquad (3\text{-}10)$$

We know from our data (Table 3-5) that we have 50% BV within x=1.3 µm, thus in combination with x(C) it can be calculated how much of the relative amount of BV is in a given distance.

E.g. if absolute amount (100 %) of Ca stored in the skeleton is 1000g, 500 g are located within 1.3 µm (Table 3-5) distance to the canalicular boundaries, diameter (*Dm*) may set to 0.4 µm (Table 3-5),the distance x within which 6 g of Calcium would be located in is equal to:

$$x = -\frac{Dm}{2} + \sqrt{\frac{Dm^2}{4} + \frac{\frac{\pi(1.3\mu m)^2 + \pi\, Dm\, 1.3\mu m}{\frac{500g}{6g}}}{\pi}} = 0.058\ \mu m \qquad (3\text{-}11)$$

4 CONCLUSION

Bone is a biological material structured in a hierarchical way over several length scales, from the molecular level of collagen to the organ level (Fratzl & Weinkamer, 2007, Weiner & Traub, 1992, Rho et al., 1998). Apparent bone quality depends on bone properties at all scale lengths. Human bone undergoes permanent remodeling in order to adjust to mechanical demands, to repair microcracks and to maintain mineral homeostasis. Details on the morphology of the micro/nano porosity as well as properties of the surrounding mineralized tissue at this scale are of high interest in understanding bone function at all length scales.

Aiming to investigate the morphology of the lacuno-canalicular network (LCN) and the mass density distribution of human cortical jaw bone and to establish a comparison between healthy subjects and patients treated with bisphosphonates, the present thesis shows that synchrotron radiation CT is a well-suited tool for the analysis of bone at the micron and sub-micron length scales. In combination with a phase retrieval, we were able to demonstrate that nano-CT enables not only the assessment of the morphology of the LCN but also the alterations in terms of mass density of the extracellular matrix in the direct vicinity of the LCN.

In an explorative study described in Chapter 3.1., we were able to quantify osteocyte lacunar geometrical properties in human jaw bone on the sub-micron length scale using µCT with attenuation contrast. Based on five jaw bone samples, originating from two healthy subjects and three patients suffering from BRONJ, we detailed the properties of lacunae (N=19208) such as average volume (296 - 502 μm^3) and the distribution of the volumes for each specimen, quantified by the standard deviation (153 – 234 μm^3). We observed that the mean and standard deviation of lacunar size are smaller in osteonal tissue in comparison to the entire sample. The average shape of all lacunae could be described using an ellipse characterized by its axes $a>b>c$, such that $a=2.2b$ and $a=4c$. The lacunar density was found to variy between 15800 and 50200 per mm^3. Additionally, we quantified the spatial distribution of the lacunae using a measure of the distance from the lacunae to the mineralized matrix and found that on average 50% of the mineralized matrix volume is located within 11.9 µm, with respect to the closest lacunar boundary. Furthermore, we described the frequency of lacunae containing mineralized objects and found this to be elevated in BRONJ samples. In this pilot study, we have not related our findings to the course or cause of

BRONJ, due to the small number of specimens. However, we found that the differences in morphological properties are statistically significant for all five investigated specimens.

In the second part of this thesis, described in Chapter 3.2., we included a larger set of human bone sections, originating from the femoral site (N=7), the tibial site (N=3), BRONJ (N=10) and healthy jaw bone (N=9). Using μCT in combination with a phase retrieval, we observed a lower degree of mineralization for the jaw bone compared to tibia. Comparing the volume distribution of osteocyte lacunae in the jaw bone to those of the tibial or femoral sites, we discovered larger lacunae in the jaw. We did not observe statistically significant differences in terms of the degree of mineralization in jaw bone when comparing patients treated with BP and healthy controls. Interestingly, we could not confirm that the patients treated with BP reveal larger osteocyte lacunae. The question whether the potentially occurring osteocytic osteolysis results in decreased peri-lacunar mineralization instead of enlarged osteocyte lacunae could not yet be explored.

Based on these results we hypothesized that BPs are more easily deposited into jaw bone due to the high bone turnover, and if deposited into lacunae during the mineralization of osteocyte lacunae (micropetrosis), a toxic concentration of bisphosphonates can be reached following the de-solution of mineral caused by a decreased pH level in the course of infections, for example. This process potentially explains the occurrence of BRONJ. However, it requires more in-depth study, in particular with samples originating from more homogeneous groups than those being used in the present thesis.

In a third approach, shown in Chapter 3.3, we applied synchrotron radiation nano-CT at 50 nm isotropic voxel size in combination with a phase retrieval to investigate and compare the morphology of the canalicular network and the bone tissue properties in the vicinity of the lacuna-canalicular network of human jaw bone originating from healthy subjects and bisphosphonate treated patients.

Regarding the morphology of the canalicular network, we found the canalicular porosity to be around 2 % with minor differences between the different tissue types (osteonal tissue, interstitial tissue, tissue originating from patients suffering from BRONJ). We observed a non-significant trend that canalicular diameter is higher in BRONJ tissue (Cn.Dm = 0.40 ± 0.04 μm) compared to osteonal (Cn.Dm = 0.36 ± 0.01 μm) and interstitial (Cn.Dm = 0.37 ± 0.04 μm) tissues. The average $Cn.Dist_{50}$ of all ROIs analyzed was found to be 1.3 ± 0.4 μm.

We noticed that the hypothesized mass density gradients in the pore adjacent extracellular matrix indeed exist at both the lacunar and canalicular interfaces. Our finding that these gradients exist both at the lacunar as well as at the canalicular surface, suggests that the process of mineral exchange between the extracellular fluid and the mineralized matrix occurs at all bone surfaces, including the canalicular network. Our data further suggests that the capacity of the matrix to exchange mineral with the extracellular mineralized bone matrix is increased by one order of magnitude if the canalicular surface is taken into account. Based on the morphology of the lacuna-canalicular network, we could show that the mass density gradients are most likely to be unaffected by short-term fluctuations of mineral in the extracellular fluid, and are instead solely affected by secondary mineralization processes. To conclude, the findings concerning the effective diffusion processes during secondary mineralization and the fact that the canalicular surfaces are likely to be involved in the diffusion process provide an important contribution with respect to understanding and optimizing of drug delivery. However, more sophisticated studies should be performed, targeting not only the changes in tissue properties during secondary mineralization but also during fluctuations in mineral concentration in periods of high mineral demand.

In future studies, the spatial deposition of BP within the bone tissue should be investigated at the micron-length scale. Suitable methods for this could be X-ray absorption techniques such as μXANES. Using this method, our formulated hypothesis from Chapter 3.2. could be tested, i.e. whether BP accumulate differently in the jaw bone compared to other anatomical sites and especially in osteocyte lacunae during the process of micropetrosis. The mineralized objects (pearls) found inside many lacunae should be further investigated in terms of elemental composition. In addition, the role of these pearls in the course of mineral homeostasis would also be interesting to investigate.

The impact on the stress/strain experienced by the osteocytes due to reported alterations of mass density in the direct vicinity of the LCN could be assessed using finite element modeling. Determining the diffusion constant of mineral through the mineralized matrix for different matrix mineralization levels would allow new insights into the capacity and dynamics of the bone matrix to store mineral, rather than only considering the remodeling of the boundaries of the LCN.

5 REFERENCES

(2009) CHMP ASSESSMENT REPORT ON BISPHOSPHONATES AND OSTEONECROSIS OF THE JAW. European Medicines Agency.

Allen, M. R. & Burr, D. B. (2008) Mandible matrix necrosis in beagle dogs after 3 years of daily oral bisphosphonate treatment. *Journal of oral and maxillofacial surgery : official journal of the American Association of Oral and Maxillofacial Surgeons,* **66,** 987-994.

Allen, M. R. & Ruggiero, S. L. (2009) Higher bone matrix density exists in only a subset of patients with bisphosphonate-related osteonecrosis of the jaw. *Journal of oral and maxillofacial surgery : official journal of the American Association of Oral and Maxillofacial Surgeons,* **67,** 1373-1377.

Als-Nielsen, J. & McMorrow, D. (2011) X-rays and their interaction with matter. In: *Elements of Modern X-ray Physics.* John Wiley & Sons, Inc.

Anderson, E. J. & Knothe Tate, M. L. (2008) Idealization of pericellular fluid space geometry and dimension results in a profound underprediction of nano-microscale stresses imparted by fluid drag on osteocytes. *Journal of biomechanics,* **41,** 1736-1746.

Atkins, G. J. & Findlay, D. M. (2012) Osteocyte regulation of bone mineral: a little give and take. *Osteoporosis international : a journal established as result of cooperation between the European Foundation for Osteoporosis and the National Osteoporosis Foundation of the USA,* **23,** 2067-2079.

Azevedo, F. A. C., Carvalho, L. R. B., Grinberg, L. T., Farfel, J. M., Ferretti, R. E. L., Leite, R. E. P., Jacob, W., Lent, R. & Herculano-Houzel, S. (2009) Equal Numbers of Neuronal and Nonneuronal Cells Make the Human Brain an Isometrically Scaled-Up Primate Brain. *J Comp Neurol,* **513,** 532-541.

Bach-Gansmo, F. L., Irvine, S. C., Bruel, A., Thomsen, J. S. & Birkedal, H. (2013) Calcified cartilage islands in rat cortical bone. *Calcified tissue international,* **92,** 330-338.

Bauss, F., Pfister, T. & Papapoulos, S. (2008) Ibandronate uptake in the jaw is similar to long bones and vertebrae in the rat. *Journal of bone and mineral metabolism,* **26,** 406-408.

Belanger, L. F., Belanger, C. & Semba, T. (1967) Technical approaches leading to the concept of osteocytic osteolysis. *Clinical orthopaedics and related research,* **54,** 187-196.

Bertoldo, F., Santini, D. & Lo Cascio, V. (2007) Bisphosphonates and osteomyelitis of the jaw: a pathogenic puzzle. *Nature clinical practice. Oncology,* **4,** 711-721.

Blaber, E. A., Dvorochkin, N., Lee, C., Alwood, J. S., Yousuf, R., Pianetta, P., Globus, R. K., Burns, B. P. & Almeida, E. A. (2013) Microgravity induces pelvic bone loss through osteoclastic activity, osteocytic osteolysis, and osteoblastic cell cycle inhibition by CDKN1a/p21. *PloS one,* **8,** e61372.

Bonewald, L. F. (2011) The amazing osteocyte. *Journal of bone and mineral research : the official journal of the American Society for Bone and Mineral Research,* **26,** 229-238.

Bonnet, N., Lesclous, P., Saffar, J. L. & Ferrari, S. (2013) Zoledronate effects on systemic and jaw osteopenias in ovariectomized periostin-deficient mice. *PloS one,* **8,** e58726.

Boskey, A. & Pleshko Camacho, N. (2007) FT-IR imaging of native and tissue-engineered bone and cartilage. *Biomaterials,* **28,** 2465-2478.

Burger, E. H. & Klein-Nulend, J. (1999) Mechanotransduction in bone--role of the lacuno-canalicular network. *FASEB journal : official publication of the Federation of American Societies for Experimental Biology,* **13 Suppl,** S101-112.

Busse, B., Djonic, D., Milovanovic, P., Hahn, M., Puschel, K., Ritchie, R. O., Djuric, M. & Amling, M. (2010) Decrease in the osteocyte lacunar density accompanied by hypermineralized lacunar occlusion reveals failure and delay of remodeling in aged human bone. *Aging cell,* **9,** 1065-1075.

Carpentier, V. T., Wong, J., Yeap, Y., Gan, C., Sutton-Smith, P., Badiei, A., Fazzalari, N. L. & Kuliwaba, J. S. (2012) Increased proportion of hypermineralized osteocyte lacunae in osteoporotic and osteoarthritic human trabecular bone: implications for bone remodeling. *Bone,* **50,** 688-694.

Carter, Y., Thomas, C. D., Clement, J. G. & Cooper, D. M. (2013a) Femoral osteocyte lacunar density, volume and morphology in women across the lifespan. *Journal of structural biology,* **183,** 519-526.

Carter, Y., Thomas, C. D., Clement, J. G., Peele, A. G., Hannah, K. & Cooper, D. M. (2013b) Variation in osteocyte lacunar morphology and density in the human femur--a synchrotron radiation micro-CT study. *Bone,* **52,** 126-132.

Cloetens, P., Ludwig, W., Baruchel, J., Dyck, D. V., Landuyt, J. V., Guigay, J. P. & Schlenker, M. (1999) Holotomography: Quantitative phase tomography with micrometer resolution using hard synchrotron radiation x rays. *Applied Physics Letters,* **75,** 2912-2914.

Cloetens, P., Pateyron-Salome, M., Buffiere, J. Y., Peix, G., Baruchel, J., Peyrin, F. & Schlenker, M. (1997) Observation of microstructure and damage in materials by phase sensitive radiography and tomography. *Journal of Applied Physics,* **81,** 5878-5886.

Cremers, S. C., Pillai, G. & Papapoulos, S. E. (2005) Pharmacokinetics/pharmacodynamics of bisphosphonates: use for optimisation of intermittent therapy for osteoporosis. *Clinical pharmacokinetics,* **44,** 551-570.

Currey, J. D. (1984a) Effects of differences in mineralization on the mechanical properties of bone. *Philosophical transactions of the Royal Society of London. Series B, Biological sciences,* **304,** 509-518.

Currey, J. D. (1984b) The Mechanical Adaption of Bone. *Princeton University Press*.

Currey, J. D. (2003) The many adaptations of bone. *Journal of biomechanics,* **36,** 1487-1495.

Dall'Ara, E., Luisier, B., Schmidt, R., Kainberger, F., Zysset, P. & Pahr, D. (2013) A nonlinear QCT-based finite element model validation study for the human femur tested in two configurations in vitro. *Bone,* **52,** 27-38.

del Río, M. S. & Dejus, R. J. (2004) XOP 2.1 — A New Version of the X-ray Optics Software Toolkit. *AIP Conference Proceedings,* **705,** 784-787.

Dhillon, S. & Lyseng-Williamson, K. A. (2008) Zoledronic acid - A review of its use in the management of bone metastases of malignancy. *Drugs,* **68,** 507-534.

Diemoz, P. C., Bravin, A., Langer, M. & Coan, P. (2012) Analytical and experimental determination of signal-to-noise ratio and figure of merit in three phase-contrast imaging techniques. *Optics express,* **20,** 27670–27690.

Dierolf, M., Menzel, A., Thibault, P., Schneider, P., Kewish, C. M., Wepf, R., Bunk, O. & Pfeiffer, F. (2010) Ptychographic X-ray computed tomography at the nanoscale. *Nature,* **467,** 436-439.

Dong, P., Haupert, S., Gouttenoire, P.-J. & Peyrin, F. (2013a) Efficient extraction of 3D bone cells descriptors from micro-CT images. In: *Biomedical Imaging (ISBI), 2013 IEEE 10th International Symposium on.*

Dong, P., Haupert, S., Hesse, B., Langer, M., Gouttenoire, P.-J., Bousson, V. & Peyrin, F. (2013b) 3D osteocyte lacunar morphometric properties and distributions in human femoral cortical bone using synchrotron radiation micro-CT images. *Bone,* **60,** 172-185.

Feng, J. Q., Clinkenbeard, E. L., Yuan, B., White, K. E. & Drezner, M. K. (2013) Osteocyte regulation of phosphate homeostasis and bone mineralization underlies the pathophysiology of the heritable disorders of rickets and osteomalacia. *Bone,* **54,** 213-221.

Fernandez, V., Abdala, F., Carlson, K. J., Cook, D. C., Rubidge, B. S., Yates, A. & Tafforeau, P. (2013) Synchrotron Reveals Early Triassic Odd Couple: Injured Amphibian and Aestivating Therapsid Share Burrow. *PloS one,* **8,** e64978.

Fratzl, P. & Weinkamer, R. (2007) Nature's hierarchical materials. *Prog Mater Sci,* **52,** 1263-1334.

Frost, H. M. (1960) Micropetrosis. *The Journal of bone and joint surgery. American volume,* **42-A,** 144-150.

Fuchs, R. K., Faillace, M. E., Allen, M. R., Phipps, R. J., Miller, L. M. & Burr, D. B. (2011) Bisphosphonates do not alter the rate of secondary mineralization. *Bone,* **49,** 701-705.

Hannah, K. M., Thomas, C. D., Clement, J. G., De Carlo, F. & Peele, A. G. (2010) Bimodal distribution of osteocyte lacunar size in the human femoral cortex as revealed by micro-CT. *Bone,* **47,** 866-871.

Hesse, B., Langer, M., Varga, P., Pacureanu, A., Dong, P., Schrof, S., Männicke, N., Suhonen, H., Olivier, C., Kazakia, G. J., Raum, K. & Peyrin, F. (2014) Alterations of mass density and 3D osteocyte lacunar properties in bisphosphonate related osteonecrotic human jaw bone, a synchrotron µCT study. *PloS one*.

Hesse, B., Männicke, N., Pacureanu, A., Varga, P., Langer, M., Maurer, P., Peyrin, F. & Raum, K. (2013 UNDER REVIEW) Accessing osteocyte lacunar geometrical properties in human jaw bone on the sub-micron length scale using SR µCT. *Journal of microscopy*.

Heymsfield, S., Lohman, T., Wang, Z. & Going, S. (2005) *Human body composition*.

Hildebrand, T. & Rüegsegger, P. (1997) A new method for the model-independent assessment of thickness in three-dimensional images. *Journal of microscopy,* **185,** 67-75.

Hofmann, T., Heyroth, F., Meinhard, H., Franzel, W. & Raum, K. (2006) Assessment of composition and anisotropic elastic properties of secondary osteon lamellae. *Journal of biomechanics,* **39,** 2282-2294.

Huja, S. S., Fernandez, S. A., Hill, K. J. & Li, Y. (2006) Remodeling dynamics in the alveolar process in skeletally mature dogs. *The anatomical record. Part A, Discoveries in molecular, cellular, and evolutionary biology,* **288,** 1243-1249.

Hunter, G. K., Hauschka, P. V., Poole, A. R., Rosenberg, L. C. & Goldberg, H. A. (1996) Nucleation and inhibition of hydroxyapatite formation by mineralized tissue proteins. *Biochem J,* **317 (Pt 1),** 59-64.

ICRU (1989) Tissue Substitutes in Radiation Dosimetry and Measurement, Report 44 of the International Commission on Radiation Units and Measurements (Bethesda, MD).

Isaksson, H., Harjula, T., Koistinen, A., Iivarinen, J., Seppanen, K., Arokoski, J. P., Brama, P. A., Jurvelin, J. S. & Helminen, H. J. (2010) Collagen and mineral deposition in rabbit cortical bone during maturation and growth: effects on tissue properties. *Journal of orthopaedic research : official publication of the Orthopaedic Research Society,* **28,** 1626-1633.

Jarque, C. M., Bera, A.K. (1987) A test for normality of observations and regression residuals. *International Statistical Review,* **Vol. 55,** 163–172.

Jensen, T. H., Bech, M., Binderup, T., Bottiger, A., David, C., Weitkamp, T., Zanette, I., Reznikova, E., Mohr, J., Rank, F., Feidenhans'l, R., Kjaer, A., Hojgaard, L. & Pfeiffer, F. (2013) Imaging of metastatic lymph nodes by X-ray phase-contrast micro-tomography. *PloS one,* **8,** e54047.

Jilka, R. L., Noble, B. & Weinstein, R. S. (2013) Osteocyte apoptosis. *Bone,* **54,** 264-271.

Jubiz, W., Canterbury, J. M., Reiss, E. & Tyler, F. H. (1972) Circadian rhythm in serum parathyroid hormone concentration in human subjects: correlation with serum calcium, phosphate, albumin, and growth hormone levels. *The Journal of clinical investigation,* **51,** 2040-2046.

Kak, A. C. & Slaney, M. (1988) Principles of Computerized Tomographical Imaging. *IEEE Press*.

Kamioka, H., Kameo, Y., Imai, Y., Bakker, A. D., Bacabac, R. G., Yamada, N., Takaoka, A., Yamashiro, T., Adachi, T. & Klein-Nulend, J. (2012) Microscale fluid flow analysis in a human osteocyte canaliculus using a realistic high-resolution image-based three-dimensional model. *Integrative biology : quantitative biosciences from nano to macro,* **4,** 1198-1206.

Kazakia, G. J., Burghardt, A. J., Cheung, S. & Majumdar, S. (2008) Assessment of bone tissue mineralization by conventional x-ray microcomputed tomography: comparison with synchrotron radiation microcomputed tomography and ash measurements. *Medical physics,* **35,** 3170-3179.

Kerschnitzki, M., Kollmannsberger, P., Burghammer, M., Duda, G. N., Weinkamer, R., Wagermaier, W. & Fratzl, P. (2013) Architecture of the osteocyte network correlates with bone material quality. *Journal of bone and mineral research : the official journal of the American Society for Bone and Mineral Research,* **28,** 1837-1845.

Kerschnitzki, M., Wagermaier, W., Roschger, P., Seto, J., Shahar, R., Duda, G. N., Mundlos, S. & Fratzl, P. (2011) The organization of the osteocyte network mirrors the extracellular matrix orientation in bone. *Journal of structural biology,* **173,** 303-311.

Klein-Nulend, J., Bakker, A. D., Bacabac, R. G., Vatsa, A. & Weinbaum, S. (2013) Mechanosensation and transduction in osteocytes. *Bone,* **54,** 182-190.

Knothe Tate, M. L. (2003) "Whither flows the fluid in bone?" An osteocyte's perspective. *Journal of biomechanics,* **36,** 1409-1424.

Knothe Tate, M. L. (2011) Top down and bottom up engineering of bone. *Journal of biomechanics,* **44,** 304-312.

Kuhl, S., Walter, C., Acham, S., Pfeffer, R. & Lambrecht, J. T. (2012) Bisphosphonate-related osteonecrosis of the jaws--a review. *Oral oncology,* **48,** 938-947.

Lakshmanan, S., Bodi, A. & Raum, K. (2007) Assessment of Anisotropic Tissue Elasticity of Cortical Bone from High-Resolution, Angular Acoustic Measurements. *Ultrasonics, Ferroelectrics and Frequency Control, IEEE Transactions on,* **54,** 1560-1570.

Lane, N. E., Yao, W., Balooch, M., Nalla, R. K., Balooch, G., Habelitz, S., Kinney, J. H. & Bonewald, L. F. (2006) Glucocorticoid-treated mice have localized changes in trabecular bone material properties and osteocyte lacunar size that are not observed in placebo-treated or estrogen-deficient mice. *Journal of bone and mineral research : the official journal of the American Society for Bone and Mineral Research,* **21,** 466-476.

Langer, M., Cloetens, P., Guigay, J. P. & Peyrin, F. (2008) Quantitative comparison of direct phase retrieval algorithms in in-line phase tomography. *Medical physics,* **35,** 4556-4566.

Langer, M., Cloetens, P., Hesse, B., Suhonen, H., Pacureanu, A., Raum, K. & Peyrin, F. (2014) Priors for X-ray in-line phase tomography of heterogeneous objects. *Phil. Trans. R. Soc. A***,** In press.

Langer, M., Cloetens, P., Pacureanu, A. & Peyrin, F. (2012a) X-ray in-line phase tomography of multimaterial objects. *Optics letters,* **37,** 2151-2153.

Langer, M., Pacureanu, A., Suhonen, H., Grimal, Q., Cloetens, P. & Peyrin, F. (2012b) X-ray phase nanotomography resolves the 3D human bone ultrastructure. *PloS one,* **7,** e35691.

Langer, M., Prisby, R., Peter, Z., Guignandon, A., Lafage-Proust, M. H. & Peyrin, F. (2011) Simultaneous 3D Imaging of Bone and Vessel Microstructure in a Rat Model. *Nuclear Science, IEEE Transactions on,* **58,** 139-145.

Lanyon, L. E. (1993) Osteocytes, strain detection, bone modeling and remodeling. *Calcified tissue international,* **53 Suppl 1,** S102-106; discussion S106-107.

Laurencin, D., Wong, A., Chrzanowski, W., Knowles, J. C., Qiu, D., Pickup, D. M., Newport, R. J., Gan, Z., Duer, M. J. & Smith, M. E. (2010) Probing the calcium and sodium local environment in bones and teeth using multinuclear solid state NMR and X-ray absorption spectroscopy. *Physical chemistry chemical physics : PCCP,* **12,** 1081-1091.

LeBlanc, A. D., Spector, E. R., Evans, H. J. & Sibonga, J. D. (2007) Skeletal responses to space flight and the bed rest analog: a review. *Journal of musculoskeletal & neuronal interactions,* **7,** 33-47.

Lesclous, P., Abi Najm, S., Carrel, J. P., Baroukh, B., Lombardi, T., Willi, J. P., Rizzoli, R., Saffar, J. L. & Samson, J. (2009) Bisphosphonate-associated osteonecrosis of the jaw: a key role of inflammation? *Bone,* **45,** 843-852.

Li, C., Paris, O., Siegel, S., Roschger, P., Paschalis, E. P., Klaushofer, K. & Fratzl, P. (2010) Strontium is incorporated into mineral crystals only in newly formed bone during strontium ranelate treatment. *Journal of bone and mineral research : the official journal of the American Society for Bone and Mineral Research,* **25,** 968-975.

Liberman, U. A., Weiss, S. R., Broll, J., Minne, H. W., Quan, H., Bell, N. H., Rodriguezportales, J., Downs, R. W., Dequeker, J., Favus, M., Seeman, E., Recker, R. R., Capizzi, T., Santora, A. C., Lombardi, A., Shah, R. V., Hirsch, L. J. & Karpf, D. B. (1995) Effect of Oral Alendronate on Bone-Mineral Density and the Incidence of Fractures in Postmenopausal Osteoporosis. *New Engl J Med,* **333,** 1437-1443.

Mahamid, J., Addadi, L. & Weiner, S. (2011a) Crystallization pathways in bone. *Cells, tissues, organs,* **194,** 92-97.

Mahamid, J., Sharir, A., Gur, D., Zelzer, E., Addadi, L. & Weiner, S. (2011b) Bone mineralization proceeds through intracellular calcium phosphate loaded vesicles: a cryo-electron microscopy study. *Journal of structural biology,* **174,** 527-535.

Marenzana, M., Shipley, A. M., Squitiero, P., Kunkel, J. G. & Rubinacci, A. (2005) Bone as an ion exchange organ: Evidence for instantaneous cell-dependent calcium efflux from bone not due to resorption. *Bone,* **37,** 545-554.

Marinescu, M., Langer, M., Durand, A., Olivier, C., Chabrol, A., Rositi, H., Chauveau, F., Cho, T. H., Nighoghossian, N., Berthezene, Y., Peyrin, F. & Wiart, M. (2013) Synchrotron Radiation X-Ray Phase Micro-computed Tomography as a New Method to Detect Iron Oxide Nanoparticles in the Brain. *Molecular imaging and biology : MIB : the official publication of the Academy of Molecular Imaging*.

Marotti, G., Ferretti, M., Remaggi, F. & Palumbo, C. (1995) Quantitative evaluation on osteocyte canalicular density in human secondary osteons. *Bone,* **16,** 125-128.

Martinez-Criado, G., Tucoulou, R., Cloetens, P., Bleuet, P., Bohic, S., Cauzid, J., Kieffer, I., Kosior, E., Laboure, S., Petitgirard, S., Rack, A., Sans, J. A., Segura-Ruiz, J., Suhonen, H., Susini, J. & Villanova, J. (2012) Status of the hard X-ray microprobe beamline ID22 of the European Synchrotron Radiation Facility. *Journal of synchrotron radiation,* **19,** 10-18.

Maurer, P., Sandulescu, T., Kriwalsky, M. S., Rashad, A., Hollstein, S., Stricker, I., Holzle, F. & Kunkel, M. (2011) Bisphosphonate-related osteonecrosis of the maxilla and sinusitis maxillaris. *International journal of oral and maxillofacial surgery,* **40,** 285-291.

McCreadie, B. R., Hollister, S. J., Schaffler, M. B. & Goldstein, S. A. (2004) Osteocyte lacuna size and shape in women with and without osteoporotic fracture. *Journal of biomechanics,* **37,** 563-572.

Meiller, T., Almubarak, H., Weikel, D., Brahim, J. & Scheper, M. (2012) Bisphosphonate-associated osteonecrosis of the jaw: are we dealing with a localized non-traditional calciphylaxis? *The open dentistry journal,* **6,** 5-7.

Mercer, E., Norton, T., Woo, S., Treister, N., Dodson, T. B. & Solomon, D. H. (2013) Ninety-One Osteoporosis Patients Affected with Bisphosphonate-Related Osteonecrosis of the Jaw: A Case Series. *Calcified tissue international*.

Metz, L. N., Martin, R. B. & Turner, A. S. (2003) Histomorphometric analysis of the effects of osteocyte density on osteonal morphology and remodeling. *Bone,* **33,** 753-759.

Milovanovic, P., Potocnik, J., Djonic, D., Nikolic, S., Zivkovic, V., Djuric, M. & Rakocevic, Z. (2012) Age-related deterioration in trabecular bone mechanical properties at material level: nanoindentation study of the femoral neck in women by using AFM. *Experimental gerontology,* **47,** 154-159.

Milovanovic, P., Zimmermann, E. A., Hahn, M., Djonic, D., Puschel, K., Djuric, M., Amling, M. & Busse, B. (2013) Osteocytic Canalicular Networks: Morphological Implications for Altered Mechanosensitivity. *ACS nano*.

Mishra, S. & Knothe Tate, M. L. (2003) Effect of lacunocanalicular architecture on hydraulic conductance in bone tissue: implications for bone health and evolution. *The anatomical record. Part A, Discoveries in molecular, cellular, and evolutionary biology,* **273,** 752-762.

Morgeneyer, T. F., Starink, M. J. & Sinclair, I. (2008) Evolution of voids during ductile crack propagation in an aluminium alloy sheet toughness test studied by synchrotron radiation computed tomography. *Acta Materialia,* **56,** 1671-1679.

Mullender, M. G., Tan, S. D., Vico, L., Alexandre, C. & Klein-Nulend, J. (2005) Differences in osteocyte density and bone histomorphometry between men and women and between healthy and osteoporotic subjects. *Calcified tissue international,* **77,** 291-296.

Mullender, M. G., van der Meer, D. D., Huiskes, R. & Lips, P. (1996) Osteocyte density changes in aging and osteoporosis. *Bone,* **18,** 109-113.

Mullins, L. P., McGarry, J. P., Bruzzi, M. S. & McHugh, P. E. (2007) Micromechanical modelling of cortical bone. *Computer methods in biomechanics and biomedical engineering,* **10,** 159-169.

Nakashima, T., Hayashi, M., Fukunaga, T., Kurata, K., Oh-Hora, M., Feng, J. Q., Bonewald, L. F., Kodama, T., Wutz, A., Wagner, E. F., Penninger, J. M. & Takayanagi, H. (2011) Evidence for osteocyte regulation of bone homeostasis through RANKL expression. *Nature medicine,* **17,** 1231-1234.

Nango, N., Kubota, S., Takeuchi, A., Suzuki, Y., Yashiro, W., Momose, A. & Matsuo, K. (2013) Talbot-defocus multiscan tomography using the synchrotron X-ray microscope to study the lacuno-canalicular network in mouse bone. *Biomedical optics express,* **4,** 917-923.

Nicolella, D. P., Feng, J. Q., Moravits, D. E., Bonivitch, A. R., Wang, Y., Dusecich, V., Yao, W., Lane, N. & Bonewald, L. F. (2008) Effects of nanomechanical bone tissue properties on bone tissue strain: implications for osteocyte mechanotransduction. *Journal of musculoskeletal & neuronal interactions,* **8,** 330-331.

Otto, S., Hafner, S., Mast, G., Tischer, T., Volkmer, E., Schieker, M., Sturzenbaum, S. R., von Tresckow, E., Kolk, A., Ehrenfeld, M. & Pautke, C. (2010) Bisphosphonate-related osteonecrosis of the jaw: is pH the missing part in the pathogenesis puzzle? *Journal of oral and maxillofacial surgery : official journal of the American Association of Oral and Maxillofacial Surgeons,* **68,** 1158-1161.

Pacureanu, A., Langer, M., Boller, E., Tafforeau, P. & Peyrin, F. (2012) Nanoscale imaging of the bone cell network with synchrotron X-ray tomography: optimization of acquisition setup. *Medical physics,* **39,** 2229-2238.

Pacureanu, A., Revol-Muller, C., Rose, J., Ruiz, M. S. & Peyrin, F. (2010) Vesselness-guided variational segmentation of cellular networks from 3D micro-CT. In: *Biomedical Imaging: From Nano to Macro, 2010 IEEE International Symposium on.*

Paganin, D., Mayo, S. C., Gureyev, T. E., Miller, P. R. & Wilkins, S. W. (2002) Simultaneous phase and amplitude extraction from a single defocused image of a homogeneous object. *Journal of microscopy,* **206,** 33-40.

Parfitt, A. M. (2003) Misconceptions (3): calcium leaves bone only by resorption and enters only by formation. *Bone,* **33,** 259-263.

Paschalis, E. P., DiCarlo, E., Betts, F., Sherman, P., Mendelsohn, R. & Boskey, A. L. (1996) FTIR microspectroscopic analysis of human osteonal bone. *Calcified tissue international,* **59,** 480-487.

Paschalis, E. P., Verdelis, K., Doty, S. B., Boskey, A. L., Mendelsohn, R. & Yamauchi, M. (2001) Spectroscopic characterization of collagen cross-links in bone. *Journal of bone and mineral research : the official journal of the American Society for Bone and Mineral Research,* **16,** 1821-1828.

Pemmer, B., Roschger, A., Wastl, A., Hofstaetter, J. G., Wobrauschek, P., Simon, R., Thaler, H. W., Roschger, P., Klaushofer, K. & Streli, C. (2013) Spatial distribution of the trace elements zinc, strontium and lead in human bone tissue. *Bone,* **57,** 184-193.

Pirklbauer, M. & Mayer, G. (2011) The exchangeable calcium pool: physiology and pathophysiology in chronic kidney disease. *Nephrology, dialysis, transplantation : official publication of the European Dialysis and Transplant Association - European Renal Association,* **26,** 2438-2444.

Pradel, A., Langer, M., Maisey, J. G., Geffard-Kuriyama, D., Cloetens, P., Janvier, P. & Tafforeau, P. (2009) Skull and brain of a 300-million-year-old chimaeroid fish revealed by synchrotron holotomography. *Proceedings of the National Academy of Sciences of the United States of America,* **106,** 5224-5228.

Preininger, B., Hesse, B., Rohrbach, D., Varga, P., Gerigk, H., Langer, M., Peyrin, F., Perka, C. & Raum, K. (2012) Histogram feature-based classification improves differentiability of early bone healing stages from micro-computed tomographic data. *Journal of computer assisted tomography,* **36,** 469-476.

Price, C., Zhou, X., Li, W. & Wang, L. (2011) Real-time measurement of solute transport within the lacunar-canalicular system of mechanically loaded bone: direct evidence for load-induced fluid flow. *Journal of bone and mineral research : the official journal of the American Society for Bone and Mineral Research,* **26,** 277-285.

Qing, H., Ardeshirpour, L., Pajevic, P. D., Dusevich, V., Jahn, K., Kato, S., Wysolmerski, J. & Bonewald, L. F. (2012) Demonstration of osteocytic perilacunar/canalicular remodeling in mice during lactation. *Journal of bone and mineral research : the official journal of the American Society for Bone and Mineral Research,* **27,** 1018-1029.

Qing, H. & Bonewald, L. F. (2009) Osteocyte remodeling of the perilacunar and pericanalicular matrix. *International journal of oral science,* **1,** 59-65.

Qiu, S., Rao, D. S., Palnitkar, S. & Parfitt, A. M. (2003) Reduced iliac cancellous osteocyte density in patients with osteoporotic vertebral fracture. *Journal of bone and mineral research : the official journal of the American Society for Bone and Mineral Research,* **18,** 1657-1663.

Qiu, S., Rao, D. S., Palnitkar, S. & Parfitt, A. M. (2006) Differences in osteocyte and lacunar density between Black and White American women. *Bone,* **38,** 130-135.

Raum, K. (2008) Microelastic imaging of bone. *IEEE transactions on ultrasonics, ferroelectrics, and frequency control,* **55,** 1417-1431.

Raum, K., Cleveland, R. O., Peyrin, F. & Laugier, P. (2006) Derivation of elastic stiffness from site-matched mineral density and acoustic impedance maps. *Physics in medicine and biology,* **51,** 747-758.

Reid, I. R., Bolland, M. J. & Grey, A. B. (2007) Is bisphosphonate-associated osteonecrosis of the jaw caused by soft tissue toxicity? *Bone,* **41,** 318-320.

Reznikov, N., Almany-Magal, R., Shahar, R. & Weiner, S. (2013) Three-dimensional imaging of collagen fibril organization in rat circumferential lamellar bone using a dual beam electron microscope reveals ordered and disordered sub-lamellar structures. *Bone,* **52,** 676-683.

Rho, J. Y., Kuhn-Spearing, L. & Zioupos, P. (1998) Mechanical properties and the hierarchical structure of bone. *Medical engineering & physics,* **20,** 92-102.

Roelofs, A. J., Coxon, F. P., Ebetino, F. H., Lundy, M. W., Henneman, Z. J., Nancollas, G. H., Sun, S., Blazewska, K. M., Bala, J. L., Kashemirov, B. A., Khalid, A. B., McKenna, C. E. & Rogers, M. J. (2010) Fluorescent risedronate analogues reveal bisphosphonate uptake by bone marrow monocytes and localization around osteocytes in vivo. *Journal of bone and mineral research : the official journal of the American Society for Bone and Mineral Research,* **25,** 606-616.

Roschger, P., Paschalis, E. P., Fratzl, P. & Klaushofer, K. (2008) Bone mineralization density distribution in health and disease. *Bone,* **42,** 456-466.

Ruffoni, D., Fratzl, P., Roschger, P., Klaushofer, K. & Weinkamer, R. (2007) The bone mineralization density distribution as a fingerprint of the mineralization process. *Bone,* **40,** 1308-1319.

Ruggiero, S. L., Dodson, T. B., Assael, L. A., Landesberg, R., Marx, R. E. & Mehrotra, B. (2009) American Association of Oral and Maxillofacial Surgeons Position Paper on Bisphosphonate-Related Osteonecrosis of the Jaws—2009 Update. *Journal of Oral and Maxillofacial Surgery,* **67,** 2-12.

Russell, R. G. G., Watts, N. B., Ebetino, F. H. & Rogers, M. J. (2008) Mechanisms of action of bisphosphonates: similarities and differences and their potential influence on clinical efficacy. *Osteoporosis International,* **19,** 733-759.

Schneider, P., Meier, M., Wepf, R. & Muller, R. (2010) Towards quantitative 3D imaging of the osteocyte lacuno-canalicular network. *Bone,* **47,** 848-858.

Stalling D, W. M., Hege H-C (2005) Amira: a highly interactive system for visual data analysis.r. In: *The Visualization Handbook.* (ed. H. C. Charles D). Elsevier, Oxford.

Talmage, R. V. & Mobley, H. T. (2008) Calcium homeostasis: reassessment of the actions of parathyroid hormone. *General and comparative endocrinology,* **156,** 1-8.

Teti, A. & Zallone, A. (2009) Do osteocytes contribute to bone mineral homeostasis? Osteocytic osteolysis revisited. *Bone,* **44,** 11-16.

Tolnai, D., Requena, G., Cloetens, P., Lendvai, J. & Degischer, H. P. (2012) Sub-micrometre holotomographic characterisation of the effects of solution heat treatment on an AlMg7.3Si3.5 alloy. *Materials science & engineering. A, Structural materials : properties, microstructure and processing,* **550,** 214-221.

Tommasini, S. M., Trinward, A., Acerbo, A. S., De Carlo, F., Miller, L. M. & Judex, S. (2012) Changes in intracortical microporosities induced by pharmaceutical treatment of osteoporosis as detected by high resolution micro-CT. *Bone,* **50,** 596-604.

Vaananen, H. K., Zhao, H., Mulari, M. & Halleen, J. M. (2000) The cell biology of osteoclast function. *Journal of cell science,* **113 (Pt 3),** 377-381.

van Hove, R. P., Nolte, P. A., Vatsa, A., Semeins, C. M., Salmon, P. L., Smit, T. H. & Klein-Nulend, J. (2009) Osteocyte morphology in human tibiae of different bone pathologies with different bone mineral density--is there a role for mechanosensing? *Bone,* **45,** 321-329.

Varga, P., Pacureanu, A., Langer, M., Suhonen, H., Hesse, B., Grimal, Q., Cloetens, P., Raum, K. & Peyrin, F. (2013) Investigation of the 3D orientation of mineralized collagen fibrils in human lamellar bone using synchrotron X-ray phase nano-tomography. *Acta biomaterialia,* **9,** 8118-8127.

Vatsa, A., Breuls, R. G., Semeins, C. M., Salmon, P. L., Smit, T. H. & Klein-Nulend, J. (2008) Osteocyte morphology in fibula and calvaria --- is there a role for mechanosensing? *Bone,* **43,** 452-458.

Verbruggen, S. W., Vaughan, T. J. & McNamara, L. M. (2012) Strain amplification in bone mechanobiology: a computational investigation of the in vivo mechanics of osteocytes. *Journal of the Royal Society, Interface / the Royal Society,* **9,** 2735-2744.

Verbruggen, S. W., Vaughan, T. J. & McNamara, L. M. (2013) Fluid flow in the osteocyte mechanical environment: a fluid-structure interaction approach. *Biomechanics and modeling in mechanobiology*.

Vignery, A. & Baron, R. (1980) Dynamic histomorphometry of alveolar bone remodeling in the adult rat. *The Anatomical record,* **196,** 191-200.

Wang, N., Butler, J. P. & Ingber, D. E. (1993a) Mechanotransduction across the Cell-Surface and through the Cytoskeleton. *Science,* **260,** 1124-1127.

Wang, N., Butler, J. P. & Ingber, D. E. (1993b) Mechanotransduction across the cell surface and through the cytoskeleton. *Science,* **260,** 1124-1127.

Wang, Y. (2007) Intuitive dimensional analyses of the energy and atomic number dependences of the cross sections for radiation interaction with matter. *JOURNAL OF X-RAY SCIENCE AND TECHNOLOGY,* **15,** 169-175.

Wang, Y., McNamara, L. M., Schaffler, M. B. & Weinbaum, S. (2007) A model for the role of integrins in flow induced mechanotransduction in osteocytes. *Proceedings of the National Academy of Sciences of the United States of America,* **104,** 15941-15946.

Webster, D. J., Schneider, P., Dallas, S. L. & Muller, R. (2013) Studying osteocytes within their environment. *Bone,* **54,** 285-295.

Weinbaum, S., Cowin, S. C. & Zeng, Y. (1994) A model for the excitation of osteocytes by mechanical loading-induced bone fluid shear stresses. *Journal of biomechanics,* **27,** 339-360.

Weiner, S. & Traub, W. (1992) Bone structure: from angstroms to microns. *FASEB journal : official publication of the Federation of American Societies for Experimental Biology,* **6,** 879-885.

Weitkamp, T., Haas, D., Wegrzynek, D. & Rack, A. (2011) ANKAphase: software for single-distance phase retrieval from inline X-ray phase-contrast radiographs. *Journal of synchrotron radiation,* **18,** 617-629.

Westbroek, I., De Rooij, K. E. & Nijweide, P. J. (2002) Osteocyte-specific monoclonal antibody MAb OB7.3 is directed against Phex protein. *Journal of bone and mineral research : the official journal of the American Society for Bone and Mineral Research,* **17,** 845-853.

Whalley, K. (2011) Circadian rhythms: Calcium sets the tempo. *Nature reviews. Neuroscience,* **12,** 434-435.

Yoo, T. S., Ackerman, M. J., Lorensen, W. E., Schroeder, W., Chalana, V., Aylward, S., Metaxas, D. & Whitaker, R. (2002) Engineering and algorithm design for an image processing Api: a technical report on ITK--the Insight Toolkit. *Studies in health technology and informatics,* **85,** 586-592.

Yu, Y. Y., Lieu, S., Hu, D., Miclau, T. & Colnot, C. (2012) Site Specific Effects of Zoledronic Acid during Tibial and Mandibular Fracture Repair. *PloS one,* **7,** e31771.

Zhao, Y., Brun, E., Coan, P., Huang, Z., Sztrokay, A., Diemoz, P. C., Liebhardt, S., Mittone, A., Gasilov, S., Miao, J. & Bravin, A. (2012) High-resolution, low-dose phase contrast X-ray tomography for 3D diagnosis of human breast cancers. *Proceedings of the National Academy of Sciences of the United States of America,* **109,** 18290-18294.

Zhou, X., Novotny, J. E. & Wang, L. (2009) Anatomic variations of the lacunar-canalicular system influence solute transport in bone. *Bone,* **45,** 704-710.

6 APPENDIX

i. **Selbständigkeitserklärung**

ii. **List of publication**

iii. **Cover page for INSA**

iv. **Folio Administratif**

v. **Acknowledgement**

Selbständigkeitserklärung

Ich erkläre hiermit, dass ich die vorliegende Arbeit selbstständig und nur unter Verwendung der angegebenen Hilfen und Hilfsmittel angefertigt habe. Alle Stellen die wörtlich oder sinngemäß aus Quellen entnommen wurden oder diesen entlehnt wurden, sind mit der Quellenangabe versehen.

Ich versichere, dass ich mich nicht anderweitig um einen Doktorgrad beworben habe oder einen entsprechenden Doktortitel besitze. Die Promotionsordnung der Mathematisch-Naturwissenschaftlichen Fakultät I der Humboldt-Universität zu Berlin habe ich gelesen und akzeptiert.

_____

Bernhard Hesse

Berlin, 20.01.2014

N° d'ordre : 2014 ISAL 0031 Année 2014

THÈSE

présenté devant

L'Institut National des Sciences Appliquée de Lyon

pour obtenir

LE GRADE DE DOCTEUR

École doctorale: ELECTRONIQUE, ELECTROTECHNIQUE, AUTOMATIQUE

par

Bernhard HESSE

Characterization of tissue properties on the sub-micron scale in human bone by means of Synchrotron Radiation CT

Soutenue le 24/ 03/ 2014 devant la commission d'examen

Jury:

Klaus RADEMANN	Professeur	Rapporteur
Pascal LAUGIER	DR CNRS	Rapporteur
Birgit KANNGIESSER	Professeur	Rapporteur
Nils BLÜTHGEN	Professeur	Examinateur
Max LANGER	CR CNRS	Invité
Kay RAUM	Professeur	Co-Directeur de thèse
Françoise PEYRIN	DR INSERM	Directeur de thèse

FOLIO ADMINISTRATIF

THESE SOUTENUE DEVANT L'INSTITUT NATIONAL DES SCIENCES APPLIQUEES DE LYON

NOM : Hesse **DATE de SOUTENANCE** : 24.03.2014

Prénoms : Bernhard

TITRE : Characterization of tissue properties on the sub-micron scale in human bone by means of Synchrotron Radiation CT

NATURE : Doctorat **Numéro d'ordre** : 2014 ISAL 0031

Ecole doctorale : Electronique, Electrotechnique, Automatique

Spécialité :

RESUME : En conditions saines, le tissu osseux est constamment remodelé pour s'adapter aux différentes contraintes mécaniques, réparer les microfissures et maintenir l'homéostasie minérale. Ce remodelage est effectué par les ostéoblastes et les ostéoclastes, responsables de la formation et de la résorption du tissu osseux. Leurs activités sont orchestrées par les ostéocytes, cellules osseuses les plus abondantes, via la mechanotransduction.

Dans cette thèse, nous avons utilisé la microtomographie par rayonnement synchrotron afin d'étudier la morphologie du réseau lacuno-canaliculaire (LCN), ainsi que la distribution 3D de la densité massique des tissus osseux minéralisés, sur des sujets sains ou atteints d'ostéonécrose de la mâchoire suite à un traitement par bisphosphonates (BP). Les BP sont utilisés pour le traitement de l'ostéoporose et des métastases osseuses, limitant la résorption osseuse par les ostéoclastes. Nous avons supposé que les patients ainsi traités présentaient un volume de lacunes ostéocytaires plus grand, dû à la résorption du tissu péri-lacunaire par ostéolyse ostéocytaire. Le sujet affecté par un manque de minéraux induit par la réduction du remodelage ostéoclastique, maintiendrait ainsi son homéostasie minérale. Cette hypothèse n'a pas été confirmée, mais nous avons toutefois remarqué que les lacunes larges étaient plus abondantes dans la mâchoire que dans le tibia et le fémur. Cela s'expliquerait par l'accumulation préférentielle des BP dans la mâchoire, au taux de remodelage élevé. De plus, si ces BP sont déposés dans les lacunes ostéocytaires pendant le processus de minéralisation, des concentrations toxiques pourraient être atteintes en cas d'infection, conduisant alors à une diminution du pH, et à la dissolution des minéraux.

Nous avons également utilisé la nanotomographie par rayonnement synchrotron avec reconstruction de phase pour analyser la morphologie du LCN et les propriétés du tissu avoisinant, sur mâchoires de sujets sains et traités par BP. Nous supposons qu'une minéralisation secondaire a lieu via la diffusion des minéraux à travers l'interface fluide-matrice, à la surface des lacunaire et des canalicules. Cela devrait conduire à une variation de la densité massique en fonction de la distance par rapport au bord des porosités, que nous avons effectivement observé.

Ainsi, l'échange minéral entre le fluide extracellulaire et la matrice minéralisée s'effectue à la frontière des lacunes et des canalicules. Nos données suggèrent que la capacité d'échange de minéraux entre le réseau poreux et la matrice osseuse augmenterait d'un ordre de grandeur si la surface canaliculaire était prise en compte. Le modèle de diffusion résultant de nos études devrait contribuer à une meilleure compréhension puis optimisation du traitement. Toutefois, des études complémentaires sur les modifications des propriétés du tissu pendant la minéralisation secondaire et les fluctuations des concentrations du minéral dans le sang sont nécessaires.

MOTS-CLES : Synchrotron Radiation ; micro and nano CT ; bone ; Lacuno-canalicular network ; mineralization

Laboratoire (s) de recherche : CREATIS

Directeur de thèse: Françoise PEYRIN

Président de jury : Nils Blüthgen

Composition du jury : Françoise PEYRIN (Directeur de thèse), Kay RAUM (Co-Directeur de thèse), Pascal LAUGIER (Rapporteur), Klaus RADEMANN (Rapporteur), Birgit KANNGIESSER (Rapporteur), Max Langer (Invité), Nils Blüthgen (Examinateur)

List of publications

Under review:

Hesse B, Männicke N, Pacureanu A, Varga P, Langer M, Maurer P, Peyrin P, Raum K; 2013 Accessing osteocyte lacunar geometrical properties in human jaw bone on the sub-micron length scale using Synchrotron Radiation μCT, under review in Journal of Microscopy

Ongoing submissions:

Hesse B*, Varga P*, Langer M, Suhonen H, Pacureanu A, Männicke N, Schrof S, Cloetens P, Peyrin F, Raum K; 2013 Peri-lacunar and peri-canalicular tissue mass densities and gradients are determined by morphology of the osteocyte-network and remodeling rate - revealed by phase-contrast Synchrotron Radiation nanoCT. Ongoing submission to JBMR; (* equal contribution)

Varga P, Hesse B, Langer M, Pacureanu A, Schrof. S, Männicke N, Suhonen H, Pahr D, Peyrin F, Raum K, Case specific finite element analysis of the in situ strains that osteocytes experience, manuscript in preparation

Frachon T, Hesse B, Rit S, Dong P, Olivier C, Peyrin F, Langer M; Optimization of acquisition conditions in synchrotron X-ray phase micro-tomography, manuscript in preparation for MedPhys

Checa S, Hesse B, Roschger P, Aido M, Duda GN, Raum K, Willie BW; 2013 In vivo mechanical loading of mice tibia results in alterations in bone tissue elastic properties of pre-existing bone. manuscript in preparation for JBMR;

Accepted:

Hesse B, Langer M, Varga P, Pacureanu A, Dong P, Schrof S, Männicke N, Suhonen H, Olivier C, Kazakia GJ, Raum K, Peyrin F; 2014 Alterations of mass density and 3D osteocyte lacunar properties in bisphosphonate related osteonecrotic human jaw bone, a synchrotron μCT study, Plos One

Dong P, Haupert S, Hesse B, Langer M, Gouttenoire PJ, Bousson V, Peyrin F;2013 3D osteocyte lacunar morphometric properties and distribution in human femoral cortical bone using synchrotron radiation micro-CT images, BONE

Langer M,Cloetens P, Hesse B, Suhonen H, Pacureanu A, Raum K, Peyrin F; 2014 Priors for X-ray in-line phase tomography of heterogeneous objects, Philosophical Transactions A

Varga P, Pacureanu A, Langer M, Suhonen H, Hesse B, Grimal Q, Cloetens P, Raum K, Peyrin F; 2013 Investigation of the 3D orientation of mineralized collagen fibrils in human lamellar bone using synchrotron X-ray phase nano-tomography. Acta biomaterialia.

Langer M, Cloetens P, Hesse B, Pacureanu A, Raum K, Lafage-Proust M, Peyrin F; 2012 Propagation based X-ray phase microtomography of multi-material objects for simultaneous bone and soft tissue visualisation Biomedical Imaging (ISBI), 2012 9th IEEE International Symposium on, pp 210-213.

Rohrbach D, Preininger B, Hesse B, Gerigk H, Perka C, Raum K; 2013 The Early Phases of Bone Healing Can Be Differentiated in a Rat Osteotomy Model by Focused Transverse-Transmission Ultrasound. Ultrasound in medicine & biology.

Preininger B*, Hesse B*, Rohrbach D, Varga P, Gerigk H, Langer M, Peyrin F, Perka C, Raum K; 2012 Histogram feature-based classification improves differentiability of early bone healing stages from micro-computed tomographic data. Journal of computer assisted tomography 36(4):469-476. (* equal contribution)

Acknowledgement ♥

Foremost, I would like to express my gratitude to my supervisors Kay Raum and Francoise Peyrin for the support of my thesis project.

Without you Peter Varga I would have gotten lost and the present thesis would not have happened. Your smartness and your patience are impressive. I hope you will once become a Professor such that more people can enjoy working with you and under your supervision.

Max Langer, it was with you when I learned the one truth “it is all wrong”, guess the challenge is to hide this as long as possible. You were insisting that as a Swede, you wouldn’t be the man of many words. I will keep things short then: Tack.

I am thankful for having great office mates. It was you guys cheering me up when “an unexpected error has occurred and the program must close”.☼♪ ♫ Nils, ♫♪♫ Martin, ♫♪♫ Susanne ♪☼!

And there are many more people contributing to the success of this work in one or the other way. In random order: Pei Dong, Cecile Olivier, Pierre-Jean, Alexandra Pacureanu, Daniel Rohrbach, Ferenc Molnar, Sabine Bartosch, Janet Klonower, …

Thank you so much Ellie Stephenson and Florent Birrien and Loriane Weber for proof reading!

♥ Alfred, Mama, Papa, Oma Doris, Opa Peter

anaJ :11